Super-elastic scattering from laser-excited calcium and silver atoms

A thesis
submitted to The University of Manchester
for the degree of
doctor of philosophy (PhD)
in the Faculty of Engineering and Physical Sciences

Sarah Jhumka

School of Physics and Astronomy
2013

Contents

List of Figures

List of Tables

Abstract

This thesis presents the results of the experimental study of super-elastic scattering from laser-excited calcium and silver atoms. The studies performed with calcium were carried out at energies of 10 eV and 12 eV in a scattering chamber evacuated to a pressure of $\sim$3 x 10^{-7} mbar. A well-collimated beam of calcium atoms, produced by a resistively heated oven at $\sim$800^{o}C, was excited from the 4^1S_0 to 4^1P_1 state, by a resonant continuous wave laser beam at $\sim$423 nm. Electrons of well-defined energy were directed onto the optically pumped target atoms which relaxed to ground state while the electrons were scattered. The electrons that gained energy equivalent to the transition in the atom were detected by an electron analyser.

The rate of super-elastically scattered electrons was measured as a function of laser polarisation and scattering angle, from which a set of atomic collision parameters, P_{lin}, γ and $L_{\perp}$ and their associated uncertainties were determined. The data obtained over the angular range of 25^{o} to 140^{o}, were compared to predictions from theoretical models. The agreement thus obtained was not satisfactory. After a 2 eV discrepancy in the energy of the electrons was identified, the experimental results at 12 eV were compared to theoretical predictions at 10 eV and the 10 eV data with available 8 eV theory. Overall, better agreement was noted between experiment and theory, and the CCC model was found to show excellent agreement.

To conduct similar experiments using silver as a target, a new high temperature oven was constructed. With the oven operating at $\sim$1200^{o}C, a well-collimated beam of silver atoms was produced which was excited from the $5^2S_{1/2}$ ground state to the $5^2P_{3/2}$ excited state using circularly polarised light at $\sim$328 nm. The excited atoms were collisionally de-excited by incident electrons of well-defined momentum and energy. The super-elastic count rates were measured as a function of laser polarisation and scattering angle over a range of 20^{o} to 130^{o}, at outgoing energies of 20-100 eV. The data obtained was compared to CCC calculations. Generally, good agreement was observed between experiment and theory especially at higher energies.

Declaration

University of Manchester

Candidate Name: Sarah Jhumka

Faculty: Faculty of Engineering and Physical Sciences

Thesis Title: Super-elastic scattering from laser-excited calcium and silver atoms

Declaration to be completed by the candidate:

I declare that no portion of this work referred to in this thesis has been submitted in support of an application for another degree or qualification of this or any other university or other institute of learning.

Signed: Date: March 12, 2014

Copyright

Acknowledgements

A PhD is a journey not achievable without the involvement of many people, some of whom I would like to take the opportunity to mention.

First and foremost, I would like to thank my supervisor, Professor Andrew Murray, for giving me the opportunity to work on this project, for his guidance, clever ideas and often desperately needed help during the research and writing of this thesis. He is an inspiration to any aspiring physicist. Many thanks go to my adviser, Dr Mark Dickinson, for his words of encouragement.

I would like to thank all those who provided assistance and distraction in the lab, in particular Martyn Hussey who patiently taught me the operation of the spectrometer and put up with my constant questioning and confusion. He also helped a great deal in tightening screws and bolts. Alex Knight-Percival assisted in my initial acclimatisation to the lab environment. Thanks must go to Kate Nixon who patiently repeated things I had previously been told. Other members of the group are also acknowledged including Matthew Harvey and John Agomuo who I also bothered for information. Special thanks are due to Professor George King who always showed a keen interest in the progress of this work. Likewise, Dr Steven Magennis often shared encouraging comments.

The technical staff from the School workshop is gratefully acknowledged especially Paul Richardson for his efforts in urgent constructions and subsequent repairs of various parts.

I would like to express my gratitude to my family: to my parents for giving me the best education they could and their unfailing support in so doing, my brothers and their partners for lending their ears to my grumbling and to Zahrah, for her love. Last but not least, I would like to thank Vincenzo for his patience and understanding, and for reminding me of the light at the end of the tunnel in my moments of despair.

Dedication

To my parents,
who taught me to walk,
and watched my every step thereafter.

List of Publications

1. S. Jhumka, K. L. Nixon, M. Hussey and A. J. Murray, "Superelastic electron collisions with silver: Measuring the angular momentum transferred to the target during the collision," *Phys. Rev. A*, vol. 87, p. 052714, 2013.

2. A. J. Murray, M. Hussey, A. Knight-Percival, S Jhumka, K. L. Nixon, M. Harvey and J. Agomuo, "Electron impact ionization and excitation studies of laser prepared targets," *J. Phys., Conf. Ser.*, vol. 388, p. 012009, 2012.

3. M. Hussey, S. Jhumka and A. J. Murray, "Electron-atom interactions in a resonant optical enhancement cavity," *Phys. Rev. A*, vol. 86, 042705, 2012.

4. A. Knight-Percival, S. Jhumka, M. Hussey and A. J. Murray, "Superelastic electron scattering from the laser-excited 4^1P_1 state of calcium at low incident energy," *Journal of Physics B: Atomic, Molecular and Optical Physics*, vol. 44, no. 10, 2011

Chapter 1

Introduction

Collisions between electrons and atoms are at the basis of numerous natural as well as man-made phenomena. Complete understanding of these processes can only be achieved by studying the interactions between the atomic systems and electrons. Detailed investigation of such collisions is needed in order to enhance our understanding of various processes in other areas of physics such as astrophysics, astronomy and plasma physics [1]. For example, laser heating of a plasma occurs as a result of collisional effects. The Sun and stars are made of plasma hence the importance of recreating plasmas in attempting to further decipher our Universe.

Collision studies are valuable tools that also help us gain insight into the internal structure of atomic systems. To date, many technological advances have been possible as a result of our deepened and ever increasing understanding in collision physics. The gas laser is one device that has emerged as a result and so is the more commonplace fluorescent lamp. In turn, the fundamental electron-atomic collision process has been more deeply probed over the last few decades owing to the newer, improved experimental techniques which come from progress in technology.

Experimental investigations of particle-atomic interactions have aided our fundamental understanding of the underlying physics and provided a means of testing theoretical predictions since the early experiments. As far back as 1911, James Franck and Gustav Ludwig Hertz carried out one of the first experi-

ments to investigate collisions between electrons and atoms, using vapourised mercury [2]. This demonstrated the existence of discrete energy levels which, at the time, provided support for Bohr's model of the atom. The practical techniques and apparatus used have since greatly improved, for instance with the notable invention of the laser in the 1960s and new atomic sources and detectors, and so the link between theory and experiment is ever more important. Extensive experimental studies of electron-impact excitation of atoms have been performed over the last three decades using increasingly sophisticated techniques. The experimental data collected from these studies provide a useful tool to test and compare different theoretical models [3].

1.1 Electron-atom collision experiments

In general, a scattering experiment constitutes of a projectile directed into a target. By observing the effect of the incident projectile after the collision, information can be gathered about the structure of the target.

In electron impact interactions with atoms, a number of processes may occur as a result of the interaction of the electron with the atom, depending on the energy of the incoming electron. These are:

i. Ionisation
   If the energy of the electron exceeds the ionisation energy of the target atom, sufficient energy may be imparted to the atom to cause it to ionise by ejecting a bound electron.

ii. Elastic scattering
   This is the most common process. The electron is elastically scattered when no net transfer of energy occurs between the colliding particles. In this case, the energy of the electron after the interaction is the same as that of the incident electron beam, but the momentum of the particles may change.

iii. Inelastic scattering
   The electron may be inelastically scattered if it imparts its energy to an

atom such that the latter is promoted to a higher internal energy state. The electron therefore leaves the interaction with lower energy.

The third outcome lays the foundation for one of the principal experimental techniques in atomic physics known as the electron-photon coincidence experiment. This requires the detection of the inelastically scattered electron in delayed time coincidence with the fluorescence emitted from the excited atom as it subsequently relaxes to a bound state of lower electronic energy [4]. The first experiment of this type was conducted by Imhof and Read in Manchester [5] where they measured helium atomic lifetimes.

In principle, such an electron impact experiment may be carried out to determine a set of atomic collision parameters (ACPs) that fully describe the quantum state of the system. For an atom excited to a P-state, these are:
γ-the alignment angle of the excited state charge cloud relative to the incident electron beam axis;
P_{lin}- the linear polarisation of the charge cloud in the scattering plane;
$L_{\perp}$- the orbital angular momentum perpendicular to the scattering plane that is transferred to the atom during the collision;
ρ_{00}- the relative height of the atomic charge cloud perpendicular to the scattering plane. These are further discussed in Chapter 2.

These parameters can be compared to predictions from theoretical models once they have been measured experimentally. These parameters were formalised in a review by Andersen *et al.* [4]. The first group that determined parameters which are related to the above mentioned ones was Kleinpoppen and co-workers who investigated the 2^1P_1 and 3^1P_1 states in helium [6, 7]. They compared their experimental findings to theoretical predictions available at the time and reported good agreement with a distorted wave calculation.

In practice, coincidence experiments are conducted inside an evacuated chamber. Generally, in such electron-atom scattering experiments, an electron gun is used to produce a beam of mono-energetic electrons. The target is usually provided by vapourising the sample in a purpose built oven fitted

with a collimator in the case of metals, or by a gas jet for gases. The electron beam with energy E_e intersects the atomic beam at the interaction region. The incident electron collides with the atom, imparting energy ΔE, equivalent to a transition in the target such that the atom is excited to a higher internal energy state. The electron is scattered with energy (E_e-ΔE). The photon emitted by the excited atom as it relaxes to a lower energy state is detected by a photon detector, *in coincidence* with the detection of the inelastically scattered outgoing electron.

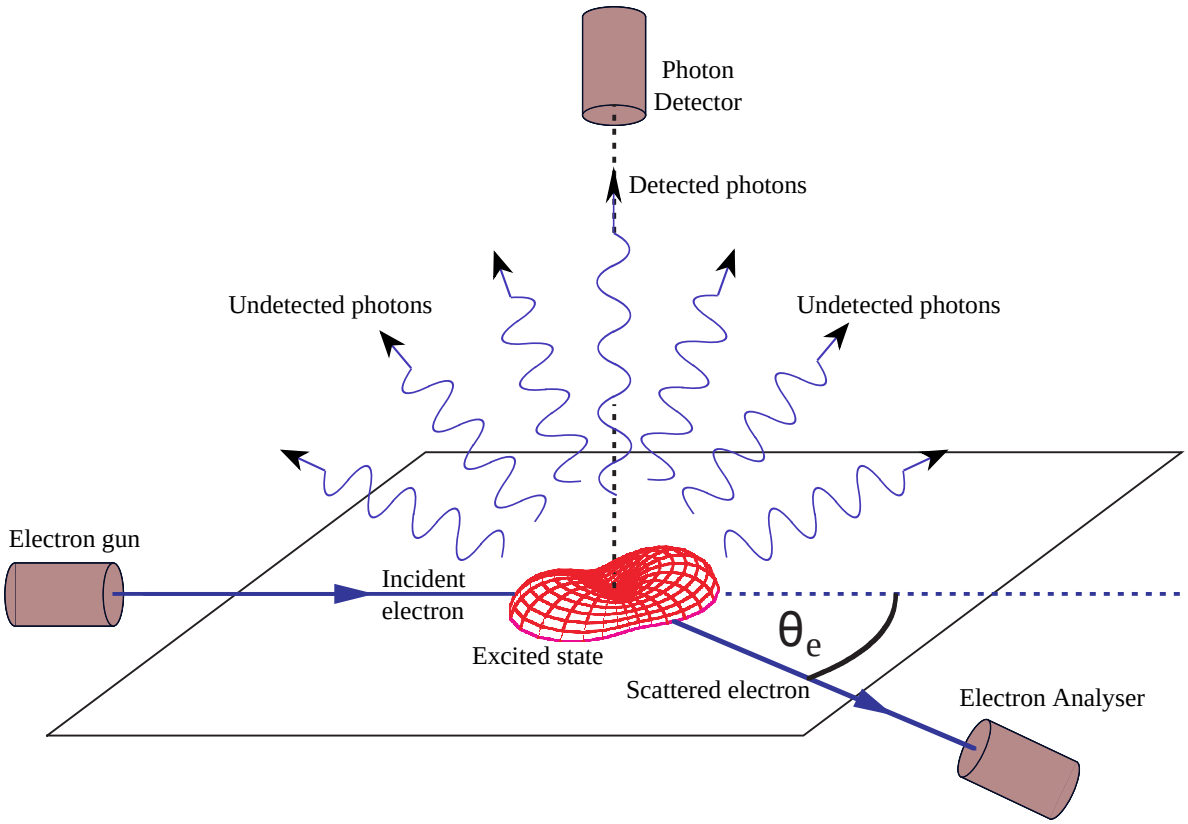

Figure 1.1: *Geometry adopted for a typical electron-photon coincidence experiment illustrating the randomness of photon emission direction as a result of the de-excitation of the atom through spontaneous emission. The probability of a photon being emitted in the direction of the detector is low.*

The analyser and photon detector are aligned to point to the interaction region so as to be efficient in the detection of the electron and photon respectively.

The interaction region is defined as the point of intersection of the atomic beam and the beam of electrons. A schematic diagram of a general electron-photon coincidence apparatus is shown in figure 1.1. By measuring the polarisation state of the emitted photons, the electronic structure of the excited state can be inferred.

The electron-photon coincidence experiment has since been extensively used and tested against various theories. Since the first experiments with helium, interest has shifted to more complicated atomic structures including but not limited to H, Hg, Na and the rare gases [8–15]. The data thus obtained have stimulated the development and improvement of various theoretical models that seek to predict the outcomes of the scattering process. The groundwork for the theoretical modelling of these experiments includes that which was carried out by Macek and Jaecks [16]. Fano and Macek defined the alignment parameters [17]. The theoretical models can be broadly classified into two categories: a distorted wave approximation method (DWA) [18] and a close-coupling approach (CC) [19]. The DWA is a higher order improvement on the Born approximation which assumes that the interaction between the electron and the atom is weak. The First-Born approximation (FBA) was the first model to use this assumption and it models the collision between the electron and the atom as a binary encounter between the incident electron and the target atom. The incident and outgoing electrons are modelled as undisturbed plane waves. On the other hand, the DW method improves from the FBA by considering as a perturbation the distortion of the electron wave function by the atomic potential. The CC treats the interaction problem in a different way to the Born Approximation and the DWA. It obtains a number of coupled equations by expanding the wave function of the scattering process. In order to find solutions using these coupled equations, it is assumed that the scattering process is dominated by a particular set of strongly interacting states only. These states usually lie close to the initial and final states.

Despite being a well tested technique, electron-photon coincidence experiments suffer from a major drawback: slow data acquisition time. This is a result of the intrinsic method utilised for the data collection. In order for a

coincidence event to be registered, the outgoing electron must be scattered in the direction of the analyser but also the resulting photon must be emitted into the photon detector. In actual fact, the excited atom emits photons randomly in all directions as it relaxes to a lower state, which implies that the photon may not necessarily hit the detector, as is illustrated in figure 1.1. For this reason, the probability of an electron being detected in coincidence with a photon is low and this results in long running times. For this reason, data from electron-photon coincidence studies only cover a limited range of mostly forward scattering angles where the cross sections are high.

One way to overcome this problem is to employ the super-elastic scattering technique which can be regarded as the time-inverse of the electron-photon coincidence process, based on the principles of quantum micro-reversibility [20]. Hertel and Stoll were the first to postulate that the coincidence process is reversible [21].

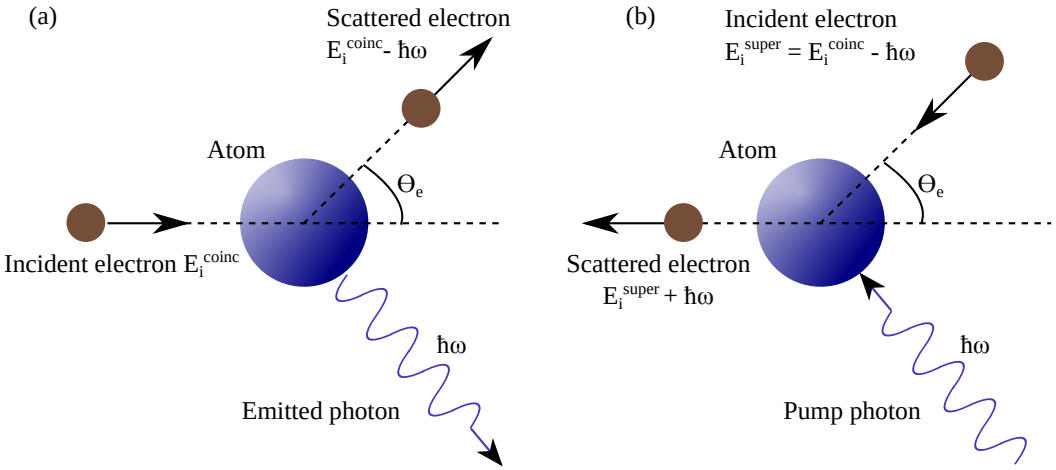

Figure 1.2: *Equivalence of the electron-photon coincidence process and the super-elastic scattering process.*

In simple terms this can be explained as follows. Consider an electron impact with an atom. Let the atom be in an initial state $|\Psi\rangle$ as shown in figure 1.2.

Upon collision with an incoming electron of energy E_i^{coinc}, the atom is excited to a state with higher internal energy $|\Psi'\rangle$. As the excited atom relaxes to a lower state which is not necessarily the ground state, it emits a photon while

the electron is inelastically scattered with energy $E_i - \hbar\omega$.

Figure 1.2(b) shows the process reversed in time. In this case, the atom has been radiatively excited to the $|\Psi'\rangle$ prior to collision with an incident electron of energy $\mathrm{E_i}^{\mathrm{super}}$. The energy released by the atom as it relaxes to a lower lying state is imparted to the outgoing electron which leaves with energy $\mathrm{E_i}^{\mathrm{super}} + \hbar\omega$.

In this way it is possible to define a so-called *equivalent energy* which relates to both the coincidence experiment as well as the super-elastic process. This represents the energy of the incident electron in the electron-photon coincidence experiment and on the other hand, the energy of the outgoing scattered electron in the super-elastic scattering process. Considering the examples in figure 1.2, this implies $\mathrm{E_{equivalent}} = \mathrm{E_i}^{\mathrm{super}} + \hbar\omega = \mathrm{E_i}^{\mathrm{coinc}}$.

Generally, super-elastic experiments proceed in the following sequence. Light from a laser of well-defined polarisation and frequency, is used to prepare atoms in an initial excited state. The atoms are usually provided by an atomic beam oven or a gas jet. The frequency of the laser matches a transition of interest in the target. For example, in the case of calcium, the laser system provided blue light at $\sim$ 423 nm corresponding to the $4^1\mathrm{S_o}$ to $4^1\mathrm{P_1}$ transition. In this case, the laser provides the "pump photon" shown in figure 1.2(b), which is effectively taking the place of the photon detector in the traditional electron-photon coincidence experiment. Upon impact with incident electrons of well-defined energy, generated by an electron gun, the atom may relax to a lower lying state. The electron then collisionally gains energy and is hence *super-elastically* scattered. The two incident particles are the photon and electron which correspond to the scattered particles in the conventional coincidence experiment.

The pioneering work in super-elastic scattering was conducted by Hertel and Stoll who reported spectra showing the inelastic as well as the first super-elastic peak from laser-excited sodium atoms [22]. The authors used circularly polarised radiation from a continuous wave dye laser to excite the sodium atoms. Collisions of the excited target atoms with incident electrons of energy 6 eV were then carried out. The spectra presented from their measurements

showed the detection of electrons that have gained energy of 2.1 eV, corresponding to the 3^2P to 3^2S transition in sodium. This was the first experiment to detect super-elastically scattered electrons from a laser-excited target. Since these initial experiments, further studies involving various processes in sodium were studied using the super-elastic technique. The work of Hermann and colleagues [23] followed, where super-elastic scattering results within a range of 3 to 20 eV were taken over the angular range of 0° and 20°. The results were compared to Born Approximation calculations available at the time and fairly good agreement was reported for small angles. Further work by the same group in 1980 over a slightly extended range of angles from 0° to 22.5°, measured the orientation in sodium for the 3^2S to 3^2P transition from 3 eV to 20 eV [24]. The results were compared to close-coupling calculations which showed good agreement especially for the data at 3 eV. When a comparison between the data was made with a distorted-wave theoretical model, poor agreement was obtained particularly at lower energies. Sodium has since been extensively studied by several groups including McClelland *et al.* [25, 26], Farrell *et al.* [27], Teubner *et al.* [28], Scholten *et al.* [29, 30], Sang *et al.* [31], Jiang *et al.* [32] and Masters *et al.* [33].

Beyond sodium, other alkali metals were also the chosen targets for additional super-elastic scattering studies. For instance, lithium was investigated by Karaganov and co-workers in 1996 at 22 eV [34], in 1998 at 7 and 14 eV [35] and subsequently in 1999 at lower energies [36]. Their results showed excellent agreement with the convergent close-coupling (CCC) theoretical model of Bray [37–39]. Super-elastic scattering investigation from potassium has been reported by Stockman *et al.* in 1998 [40]. Scattering from laser-excited barium atoms was carried out by Register *et al.* in 1978 [41], also by Li and Zetner in 1994 [42] and Johnson and co-workers in 1999 [43], and 2005 [44]. A complete set of ACPs was also determined for rubidium by Hall *et al.* in 2004 [45]. Alkali metals are relatively easy targets in that they can be vapourised and delivered using beam ovens at relatively low temperatures. Sodium requires the highest temperature to reach a vapour pressure of 10^{-2} mm Hg at 290° [46]. In addition, the interest in alkali metals also stems from the fact that their theoretical treatment is simplified by treating them as hydrogen-like targets, since they

consist of a single valence electron orbiting an inert core.

An important finding obtained through the extensive study of sodium was the fact that the so-called optical pumping parameters play an important role in the scattering process when using laser-excited atomic targets. This realisation resulted from a comparison of scattering data obtained using the coincidence method and the super-elastic technique. The optical pumping parameters are multiplicative constants required to take into account laser-induced optical pumping processes and enable accurate determination of ACPs in super-elastic experiments [36, 47]. The importance of quoting the so-called optical pumping parameters was emphasised by Farrell *et al.* [27] which prompted the experimental investigation of the behaviour of the pumping parameters by Farrell *et al.* [47] and Meng *et al.* [48].

Several groups have extended the super-elastic scattering research beyond the alkali metals. Other targets such as ytterbium [49, 50] have also been investigated. Super-elastic scattering from laser-excited caesium has also been reported [51]. The targets have mostly been restricted to alkali and alkali-earth metals. This has been imposed by the availability of commercial laser systems whose primary wavelengths range from ∼400 nm to ∼ 1000 nm. It is possible to extend this range into the UV by frequency doubling the laser radiation however the power is considerably reduced, making super-elastic experiments challenging. The focus has hence been on atomic targets which are relatively easily accessed by commercially available lasers.

Of particular interest to this project is the work undertaken to investigate super-elastic scattering from laser-excited calcium atoms. This was carried out for the first time by Law and Teubner who determined the ACP $L_\perp$ at 25.7 eV and 45 eV over an angular range of 3° to 100° [52]. Their experimental findings were compared to the theoretical predictions of Srivastava *et al.* who accounted for relativistic effects in their Relativistic Distorted Wave calculation (RDWA) [53]. Furthermore, two more sets of theoretical calculations were compared, also based on the distorted wave model, by Clark and Csanak [54]. The conclusion they drew from the comparisons was that the distorted wave model

was only partially successful in predicting the results at small angles wherein good agreement was seen at both energies investigated. In general, poor agreement was observed at higher scattering angles and lower energy. Teubner and co-workers also presented results conducted with calcium where they measured the atomic alignment parameter γ [55] and compared their results to theoretical calculations [53].

Further super-elastic scattering work with calcium was conducted by Murray and Cvejanovic at Manchester [56]. They presented a set of ACPs at 20, 25 and 35 eV, which they compared to RDW calculations provided by Stauffer and co-workers [53]. The theoretical calculations were seen to be in agreement with the data at higher energies but there were increasing discrepancies as the energy decreased. At lower energies, there was poor agreement between theory and experiment.

These experimental works in the study of calcium prompted further focus on the theoretical modelling of the scattering process by other groups. An additional model called the R-matrix was put forward by Kawazoe *et al.* who applied their model at 10, 20 and 25 eV [57]. An enhanced model based on the R-matrix, called the R-matrix B-Splines was developed by Zatsarinny and colleagues [58]. Additionally Chauhan *et al.* considered the relativistic effects in their distorted wave model calculations [59]. A convergent close-coupling (CCC) model was also proposed by Fursa and Bray [60].

Meanwhile, the group in Manchester undertook the construction of a new super-elastic spectrometer [61]. The work that then followed determined the ACPs for calcium at 45 eV and 55 eV [61]. This was achieved for the first time over the full angular range by using a magnetic angle changing (MAC) device also developed in Manchester by Read *et al.* [61–63]. Super-elastic scattering from calcium at 65 eV has also been investigated by the group at Manchester [64].

It has been seen that the DW calculations fail to accurately predict results over the full energy range in the case of calcium. Although the agreement

between theory and experimental data was promising at higher energies, the discrepancies observed at lower energies justified the need for further research in the low energy regime. Indeed, the first part of this project focused on determining the ACPs at 8 eV and 10 eV equivalent incident energy.

The principal advantage of the super-elastic scattering technique is its much higher data collection rate compared to the electron-photon coincidence process. This stems from the fact that the atomic state is coherently excited by the continuous wave (CW) laser beam which always propagates in the same direction with respect to the scattering plane. This is in direct contrast to the equivalent photon detection process in the conventional coincidence experiment, as already discussed. A measurement process in the coincidence experiment is only registered if the photon is emitted in the direction of the photon detector and the electron emitted towards the analyser.

Additionally, the laser radiation used is of the order of hundreds of milliwatts and is therefore sufficiently powerful to ensure a high density of atoms in the excited state of interest in the interaction region. The signal rate, given by the detection of scattered electrons, is high as a result of the high probability of laser excitation of the target. Signal counting rates are many thousands of times greater than the equivalent coincidence rates.

A further advantage of the super-elastic technique is the higher resolution achievable owing to the use of CW lasers [65]. The linewidth of these laser systems can be as small as 10 kHz, as was the case with the lasers used in this project for the super-elastic scattering experiment with silver. The corresponding energy resolution is $\sim$0.1 neV. Even though the actual resolution of the scattering experiment also depends on the Doppler profile of the target atoms, resolutions better than 0.1 μeV are possible in a super-elastic scattering experiment. Consequently, detailed electron impact measurements are feasible using super-elastic scattering geometry whereby close-lying states can be probed that would otherwise appear as one unresolved feature in a coincidence measurement [65].

The principle of the super-elastic experiment imposes the need for the laser frequency to be resonant with a transition in the target atom, that couples with its ground state. In order to successfully conduct these experiments, the laser has to be tuneable, stable over long periods of time and must be able to deliver sufficiently high power to enable super-elastic studies. Only a selected range of commercially available continuous wave lasers are able to meet these requirements. As a result of the above demands, the wavelength range is limited to ∼220 nm to ∼1000 nm and therefore the number of targets that can be accessed is also restricted. For targets that cannot be excited using laser radiation, the coincidence method is still necessary to carry out electron impact excitation studies.

1.1.1 Motivation

This project investigates super-elastic scattering of electrons from two different atomic targets, namely calcium [66] and silver [67]. Calcium is a group II element otherwise known as alkaline-earth metals and can be compared to helium in having two valence electrons orbiting a charged core. Calcium is composed of 97% ^{40}Ca [68]. On the other hand, silver is a transition metal with an incomplete d-electron sub-shell. It exists naturally as two stable isotopes, 51.83% ^{107}Ag and 48.16% ^{109}Ag [68]. Both isotopes have nuclear spin I=1/2 and therefore possess hyperfine structure.

Despite the obvious dissimilarities in the two atomic systems, there is one common reason that justifies the need for the experimental study of both elements. These experiments are able to provide accurate data to test theoretical calculations. There are numerous models that seek to predict the outcomes of the interactions of electrons with atomic systems. However, quantum mechanically every different atom displays different behaviour as a result of its distinct atomic structure. Generally, numerical methods are employed but these become more complicated as the atomic structure evolves into more complex systems. The calculations relating to these systems then become increasingly lengthy, often requiring large quantities of computing power. In the process, approximations are usually made to simplify the interaction model. Different models

use diverse approximations, and the only way to effectively test the validity of these assumptions is to put the theories to test by comparing their predictions with actual experimental data.

To date, super-elastic scattering from calcium has been investigated by various groups over a series of energies as discussed above, and existing theoretical predictions have been compared to the data. One conclusion that could be drawn from these previous studies is that the agreement between experiment and different theories is best at intermediate to high energies. It has been shown that the agreement with theory breaks down at incident equivalent energy of 20 eV [56]. This has warranted the need for low energy super-elastic scattering from calcium so as to further test emerging models.

During this project, super-elastic scattering data from silver has been obtained for the first time. At the time of writing, only one model has predicted these data. It is expected that this new experimental data will encourage further modelling of the scattering process in silver using additional theoretical models. By comparing their predictions to the data, it is hoped that the development of a general theory may be achieved which will be applicable to all elements from low to high energy regimes. The ultimate goal would be that this unified theory can be used to make predictions for targets that cannot be easily studied experimentally.

1.1.2 Structure of the thesis

This thesis is divided into two parts namely the experimental investigation of super-elastic scattering of electrons from laser-excited calcium and silver atoms. The thesis consists of eight chapters including this introduction to the project as well as a concluding summary. The above introduction has briefly reviewed the experimental and theoretical works in this field that have paved the way for the current project and has stated the reasons that justify these investigations.

Chapter 2 covers the theoretical framework that underlies the experimental

work of this thesis. It describes the theory relevant to the scattering experiment using calcium as an example. Quantum Electrodynamics (QED) calculations that treat the interaction of the laser system with calcium are provided. By contrast, the excitation process from silver is more complicated, given the addition of hyperfine structure. For the purpose of this thesis, which concerns the measurement of only one of the ACPs, the theory pertinent to silver has been referred to existing literature.

In Chapter 3, the equipment employed for the scattering experiments with calcium is presented. The experiments were performed inside an evacuated chamber within which most of the necessary components such as the atomic beam oven and the electron source and detector, were contained. These are individually described in separate sections. The laser system that provides the suitable radiation for the super-elastic experiments is also detailed.

Chapter 4 details the methods and procedures of the experiments conducted with calcium. These were performed for the first time in the low energy regime at 8 eV and 10 eV equivalent incident energy of the electron. The results obtained are presented and are compared to available theoretical calculations.

Chapter 5 describes the custom-built, high-temperature atomic beam source developed during the course of this project, for use with either silver, copper or gold. The design and construction of this resistively heated oven are therein illustrated. In addition, the preliminary tests conducted to establish the behaviour of the oven are also detailed. It was concluded that the oven is able to operate successfully at a temperature of $\sim$1200^{o}C and a pressure of 3x10^{-7} mbar which are satisfactory conditions for the work on silver.

Chapter 6 describes the apparatus used for the experiments with silver as the atomic target. The spectrometer employed had previously been used for coincidence studies at Manchester and was modified for the purpose of this project. The atomic beam source described in Chapter 4, was fitted into this apparatus. The remaining components for super-elastic studies in the spectrometer are also described. A dye laser operating at 328.1 nm was used to

excite the silver atoms prior to super-elastic collisions with electrons, and this is also presented here.

Chapter 7 then reviews the measurement processes involved in acquiring super-elastic scattering data using silver as a target. These were carried out at six different outgoing energies namely 20, 25, 30, 40, 50 and 100 eV. The results from these investigations are presented in this chapter. Theoretical calculations kindly provided by I.Bray [69] are also shown and a comparison is made to the experimental results obtained.

The final chapter of the thesis concludes with a summary of the work conducted in the two distinct parts of this study. Directions for possible future works, specially pertinent to the use of silver as atomic target, are also suggested.

Chapter 2

Theory

2.1 Introduction

This chapter provides an analysis of the theoretical treatment of the interaction of laser radiation and electrons with atoms during the electron super-elastic scattering process. In particular, it presents the scattering theory that describes the inelastic process, whose analysis can also be applied to the super-elastic event, as the two processes can be regarded as the time inverse of each other. The S-P transition is considered here which is relevant to both calcium and silver. The density matrix formalism is introduced to describe the resulting excited P-state. The elements of the density matrix are then related to alignment and orientation parameters that are used to describe the super-elastic scattering process.

The second part of the chapter briefly reviews the quantum electrodynamics (QED) model of the interaction of the laser field with calcium as the atomic target whereby both the laser field and the atom are treated quantum mechanically. The general equations of motion are employed in order to determine the density matrix elements that describe the evolution of the system with time. The relationship between the density matrix elements and the experimental measurements is then established.

Different approaches have been used to model the interaction between the atomic system and the laser field. The first model was proposed by Hertel and

Stoll [21] who solved a simple set of rate equations under steady state conditions. However, this approach is only valid for low laser powers, and is thus inadequate for modelling most laser assisted collision processes. The rate model was superseded by a semi-classical density matrix approach by McClelland and Kelly [25], who used optical Bloch equations to describe the interaction of atomic sodium with coherent laser light. In this case the laser was treated classically while the atomic system was given a quantum mechanical treatment. This method does not include relaxation terms which had to be added in an *ad hoc* manner. The most rigorous and complete theoretical interpretation of the collision process is the QED model which was proposed by Farrell *et al.* [47] where a fully quantum mechanical approach was employed for the atom (sodium) as well as the laser. Since then, the QED model has been extensively used for the interaction of the laser radiation with the atom in the super-elastic studies of various targets, among which are the publications of Teubner *et al.* [55] and Hall *et al.* [70]. In the work presented in this thesis, the experimental measurements are complemented with a theoretical treatment using the QED model.

The case of laser interaction with calcium from the ground state to the 4^1P_1 excited state is relatively straightforward since it can be accurately represented as a two-level system. On the other hand, the full derivation of the general equations of motion for silver is far less straightforward due to the presence of hyperfine structure. Calculations in this case would follow closely those performed by Shurgalin [71] and Hall [72] for sodium and rubidium respectively, and these works can be referred to for details. For the purpose of this thesis which investigates the super-elastic process using only circularly polarised light in the case of silver, the silver atomic system can again be considered as a two-level system under steady state conditions, and therefore the analysis conducted for calcium can be extended to silver. The introduction of optical pumping parameters is critical in accurately describing the interaction of laser radiation with different atoms as a consequence of any hyperfine structure in the atom. This is discussed in the final part of the chapter.

2.2 Scattering Theory

Following Blum [73], an atomic ensemble which is excited to a pure state by electron collision, can be represented by a wavefunction which is a linear superposition of orthonormal basis states, ϕ_i.

$$\mid \Psi\rangle = \sum_i a_i \mid \phi_i\rangle \tag{2.1}$$

where the sum over i refers to a set of quantum numbers that describe the system. For such a pure state, the density operator may be defined as [73]

$$\rho = \mid \Psi\rangle\langle\Psi \mid \tag{2.2}$$

By choosing appropriate basis states, the corresponding density matrix elements for an atomic ensemble in a pure state, may be defined as

$$\begin{aligned} \rho_{ij} &= \langle i \mid \rho \mid j\rangle \\ \Rightarrow \rho_{ij} &= \langle i \mid \Psi\rangle\langle\Psi \mid j\rangle \end{aligned} \tag{2.3}$$

For atoms that do not possess hyperfine structure, the relevant quantum numbers describing the atomic system are the angular momentum J and the magnetic quantum numbers m_j of the electrons. In the super-elastic experiments with calcium as considered in this thesis, the excited state is a ^{1}P-state, hence the excited state wavefunction can be written as:

$$\begin{aligned} \mid \Psi\rangle^{1P} = \sum_{J,m_j} a_{J,m_j} \mid J, m_j\rangle &= \sum_{m_j} a_{m_j} \mid 1, m_j\rangle \\ &= a_{+1} \mid 1,1\rangle + a_0 \mid 1,0\rangle + a_{-1} \mid 1,-1\rangle \end{aligned} \tag{2.4}$$

The a_i coefficients in the above equation may be complex and they are directly related to the scattering amplitudes f [74]. These scattering amplitudes are the terms that are calculated from collision theory to describe the collision process. The scattering amplitude at a scattering angle θ_e is given by

$$f(\theta_e) = \left\langle J, m_j \mid T \mid J', m_j'\right\rangle \tag{2.5}$$

where T is the transition operator which describes the transition from the initial state $\mid J', m'_j\rangle$ to the final state $\mid J, m_j\rangle$ following an electron collision. In order to determine the scattering amplitudes, a quantisation axis must be chosen. The *natural frame*, (x^n, y^n, z^n) is the chosen coordinate frame used in the super-elastic experiments in this thesis, and this is now generally adopted by experimental groups. This reference frame is represented in figure 2.1, where the x^n axis is along the direction of incoming electron and the x^n and y^n orthogonal axes lie within the scattering plane. The z^n axis is perpendicular to the scattering plane as shown in figure 2.1.

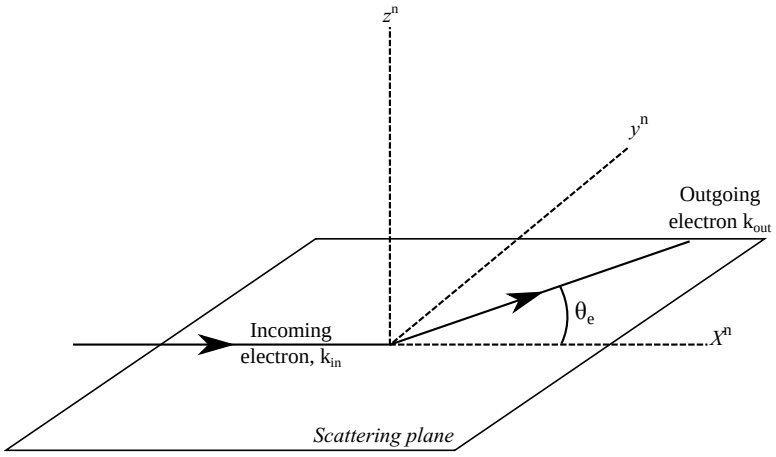

Figure 2.1: *Figure showing the natural coordinate frame defined where the x^n axis is collinear with the direction of the incident electron. The scattering plane is defined by the momenta of the incoming and outgoing electrons, k_{in} and k_{out} respectively.*

In this frame of reference, an excited pure P state can be described as a superposition of only two magnetic substates, after appropriate reduction of the states as proposed by Andersen *et al.* [4]. Hence

$$\begin{aligned} \mid \Psi\rangle^P = \sum_{J,m_j} a_{J,m_j} \mid J, m_j\rangle &= \sum_{m_j} a_{m_j} \mid 1, m_j\rangle \\ &= a_{+1} \mid 1, 1\rangle + a_{-1} \mid 1, -1\rangle \end{aligned} \tag{2.6}$$

The density matrix for the excited P-state can then be written as

$$\rho_{ij} = \begin{pmatrix} \mid a_1 \mid^2 & 0 & a_1 a_{-1}^* \\ 0 & 0 & 0 \\ a_{-1} a_1^* & 0 & \mid a_{-1} \mid^2 \end{pmatrix} = \begin{pmatrix} \rho_{11} & 0 & \rho_{1-1} \\ 0 & 0 & 0 \\ \rho_{1-1}^* & 0 & \rho_{-1-1} \end{pmatrix} \tag{2.7}$$

The number of independent elements of ρ is also the number of independent measurements that are required to make a complete determination of the density matrix. The diagonal elements of the density matrix are real quantities which measure the relative population of the atomic sub-states. The off-diagonal elements are complex numbers which relate to real parameters representing the coherences formed between the magnetic sub-states. In the natural frame, the elements of the density matrix relate to alignment and orientation of the state as suggested by Fano and Macek [17]. Andersen *et al.* [4] proposed the following parametrisation

$$\rho_{ij} = \frac{1}{2} \begin{pmatrix} 1 + L_\perp & 0 & -P_{lin} e^{-2i\gamma} \\ 0 & 0 & 0 \\ -P_{lin} e^{+2i\gamma} & 0 & 1 - L_\perp \end{pmatrix} \tag{2.8}$$

thus introducing the atomic collision parameters P_{lin}, γ and $L_\perp$. By measuring the ACPs, the density matrix elements can be determined and hence can be directly related to the theoretically calculated scattering amplitudes. In practice, theoretical calculations usually determine the scattering amplitudes and then derive the ACPs for comparison to experimental data.

2.2.1 Relating the matrix elements to experiment

The ACPs as described in Chapter 1 allow a direct visualisation of the atomic charge cloud. In order to determine these collision parameters, the differential cross section for super-elastically scattered electrons is measured as a function of the laser polarisation. The alignment and orientation parameters employed to describe the charge cloud are as follows. $L_\perp$ is the angular momentum transferred perpendicular to the scattering plane, γ is the alignment angle of the charge cloud and P_{lin} is the linear polarisation, given by the following

expression:

$$P_{lin} = \frac{l - w}{l + w} \tag{2.9}$$

These parameters are shown in figure 2.2.

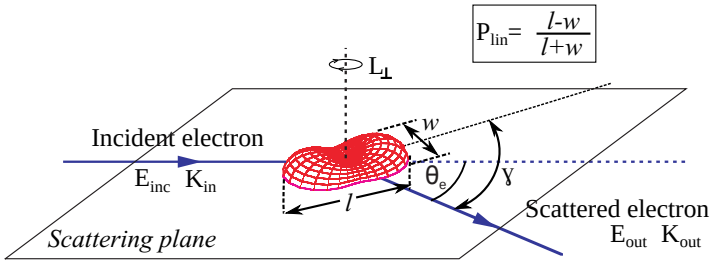

Figure 2.2: *Diagram showing a collisionally induced P state charge cloud pertaining to both the electron-photon coincidence and the super-elastic scattering experiments. The alignment and orientation parameters P_{lin}, γ and $L_\perp$ are shown.*

To establish the relationship between the experimental measurements performed in this project and the density matrix, it is useful to consider an electron-photon coincidence measurement as introduced in Chapter 1 since this can be considered as the time-inverse of the super-elastic measurements. The geometry of the experimental set-up is illustrated in figure 2.3. A source of target atoms

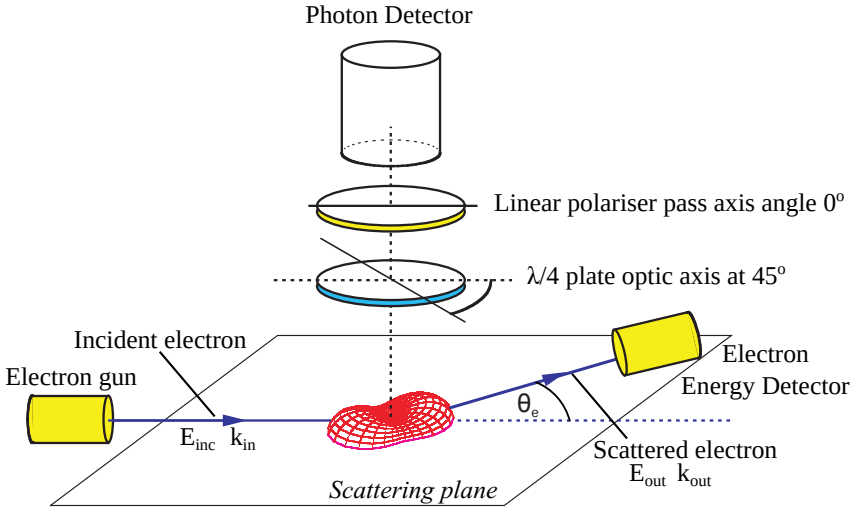

Figure 2.3: *Illustration of the geometry of the electron-photon coincidence experiment. The four main components which are the atomic beam source, electron gun, electron energy analyser and photon detector, are shown. The set-up shown with the quarter-wave plate is used to detect the P3 Stokes parameter.*

is provided either by a heated oven or a gas jet. An electron gun generates a beam of electrons of well-defined energy and momentum. Scattered electrons are detected in coincidence with photons emitted by the excited atoms using an analyser and a photon detector respectively. The atomic beam and the incoming electrons intersect at the interaction region in the scattering plane which is defined by the momenta of the incoming and scattered electrons. The photons are detected perpendicular to this plane as shown in figure 2.3.

Scattering theory generally describes the interaction in terms of the inelastic collision process. Owing to the equivalence of the two physical processes under time-reversal as pointed out in Chapter 1, the analysis derived for the coincidence process can be applied to the super-elastic event from time-reversal arguments. In the super-elastic experiment, the photon detector is replaced by a resonant laser beam which excites the target atoms, as discussed in Chapter 1. The scattered electron in the coincidence experiment is then replaced by an electron beam, while the electron gun in the coincidence experiment is replaced by an electron detector. In both coincidence and super-elastic experiments, the atomic charge cloud can be described in terms of the common set of alignment and orientation parameters P_{lin}, γ and $L_{\perp}$. In the electron photon coincidence experiment, data is measured in terms of the Stokes components P_1, P_2 and P_3 which are analogous to the components used for polarised light [75]. The components relate directly to the measurements of the rate of inelastically scattered electrons, taken in time correlated coincidence with the ejected photon. The components are

$$P_1 = \frac{I(0^o) - I(90^o)}{I(0^o) + I(90^o)} \tag{2.10a}$$

$$P_2 = \frac{I(45^o) - I(135^o)}{I(45^o) + I(135^o)} \tag{2.10b}$$

$$P_3 = \frac{I(RHC) - I(LHC)}{I(RHC) + I(LHC)} \tag{2.10c}$$

where $I(\theta^o)$ is the number of detected coincidence events with the fluorescence polarised at an angle of θ^o to the incident electron beam ; and I(RHC) and I(LHC) are the number of events when the fluorescence is right-hand and left-hand circularly polarised respectively. The alignment and orientation param-

eters previously mentioned are then related to the Stokes parameters by the following set of equations [4].

$$P_{lin} = \sqrt{P_1^2 + P_2^2} \tag{2.11a}$$

$$L_\perp = -P_3 \tag{2.11b}$$

$$\gamma = \frac{1}{2}\arg(P_1 + iP_2) \tag{2.11c}$$

The parameters P_{lin}, γ and $L_\perp$ are illustrated in figure 2.2.

In the case of a super-elastic scattering experiment, a measurement of the scattering intensity as a function of scattering angle (the super-elastic scattering differential cross section) is made. A set of pseudo-Stokes parameters can then be derived [47] given by:

$$P_1^S = \frac{S(0^o) - S(90^o)}{S(0^o) + I(90^o)} \tag{2.12}$$

$$P_2^S = \frac{S(45^o) - S(135^o)}{S(45^o) + I(135^o)} \tag{2.13}$$

$$P_3^S = \frac{S(RHC) - S(LHC)}{S(RHC) + S(LHC)} \tag{2.14}$$

The same set of formerly mentioned ACPs for the electron-photon coincidence experiment are then derived which describe the excited P-state in super-elastic scattering.

The above set of pseudo-Stokes parameters and expressions for the ACPs can be used to describe laser-induced excitation in atoms with no fine or hyperfine structure. In the general case, the above expressions cannot be directly used because the depolarisation that may occur in certain atomic targets due to hyperfine structure has not been considered. A set of optical pumping parameters need to be introduced for a valid generalisation [76]. In the case of calcium which exhibits no hyperfine structure, these optical parameters equate to unity [56]. By contrast, for atoms with hyperfine structure such as silver, so called *reduced* Stokes parameters are required which are then related to the

Stokes parameters as given below.

$$P_1{}^S = \frac{1}{K} P_1 \tag{2.15a}$$

$$P_2{}^S = \frac{1}{K} P_2 \tag{2.15b}$$

$$P_3{}^S = \frac{1}{K'} P_3 \tag{2.15c}$$

Hence, in general,

$$\bar{P_{lin}} = \sqrt{\left(P_1{}^S\right)^2 + \left(P_2{}^S\right)^2} \tag{2.16a}$$

$$L_\perp = -P_3^S \tag{2.16b}$$

$$\gamma = \frac{1}{2} \arg(P_1{}^S + iP_2{}^S) \tag{2.16c}$$

2.3 Laser-atom interaction for calcium

The following section will describe the system Hamiltonian followed by an overview of the laser field interaction with calcium atoms. This will be performed using the general equations which can be derived using the QED model for a two-level system. Calcium can be represented as such a system as shown in figure 2.4.

2.3.1 The System Hamiltonian

The Hamiltonian which fully describes the interaction of an atom with a laser field is given as

$$H = H_A + H_F + H_I \tag{2.17}$$

where H_A is the freely evolving atomic beam, H_F represents the electromagnetic field due to the laser at the interaction region and H_I is the interaction between the atom and the field term.

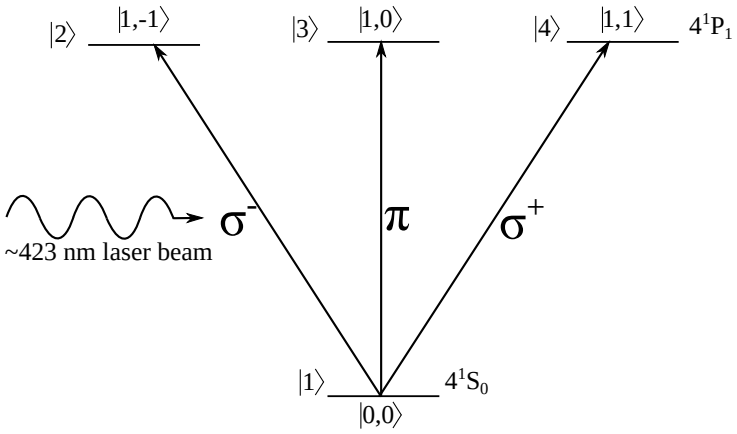

Figure 2.4: *Energy level diagram of calcium showing the 4^1S_0 ground state and the 4^1P_1 state, excited by radiation at ∼423 nm. The ground state is labelled $|1\rangle$ and the excited states are $|2\rangle, |3\rangle$ and $|4\rangle$. The allowed transitions for linearly polarised light(π), right-hand circularly polarised(σ^-) and left-hand circularly polarised (σ^+) radiation are also shown.*

The Atomic Hamiltonian, $\mathbf{H_A}$

The freely evolving atomic term is given by [77]

$$H_A = \sum_i E_i \sigma_{ii} = \sum_i \hbar\omega_i |i\rangle\langle i| \tag{2.18}$$

where the summation over i represents the orthogonal basis states of the atom. $|i\rangle$ is an eigenstate of the atomic system with energy E_i, and so $|i\rangle\langle i|$ is the operator that represents the states of the atom.

The Free Field Hamiltonian, $\mathbf{H_F}$

The free field Hamiltonian is described in terms of photon annihilation and creation operators, a_λ and $a_\lambda^\dagger$ [78]

$$H_F = \sum_\lambda \hbar\omega_\lambda a_\lambda^\dagger a_\lambda \tag{2.19}$$

where λ are the field modes that define the wavelength, polarisation and propagation of the laser beam. The field operators $a_\lambda^\dagger$ and a_λ represent the addition and removal of one photon to and from the system respectively.

The Interaction Hamiltonian, $\mathbf{H_I}$

The interaction Hamiltonian is given by

$$H_I = \hbar \sum_{\lambda'} \sum_{e'} \sum_{g'} (g^{\lambda'}_{e'g'} \sigma_{e'g'} a_{\lambda'} e^{ik_{\lambda'} z} + g^{\lambda'*}_{e'g'} a^{\dagger}_{\lambda'} e^{-ik_{\lambda'} z} \sigma_{g'e'}) \tag{2.20}$$

where $g^{\lambda'}_{e'g'}$ terms represent the coupling coefficient between the field mode λ' and the excited and ground states $\mid g\rangle$ to $\mid e\rangle$.
Equation 2.20 involves two processes as follows:

1. $\sigma_{e'g'} a_{\lambda'}$ represents the annihilation of a photon and the transition of an electron from a ground state $|g'\rangle$ to an excited state $|e'\rangle$.

2. $\sigma_{g'e'} a^{\dagger}_{\lambda'}$ represents the creation of a photon and the decay of an electron from excited state $|e'\rangle$ to a ground state $|g'\rangle$.

2.3.2 Evolution of the System

Considering the evolution of the atomic operators, a set of general equations can be derived in order to describe the time dependence of the system. In the Heisenberg representation, the following commutation relation gives the equation of motion for an operator A [79]:

$$\frac{dA}{dt} = -\frac{i}{\hbar}[A, H] \tag{2.21}$$

where H is the Hamiltonian that fully describes the atom-light interaction.

The equation of motion for the atomic operators are then given by

$$\begin{aligned}
\frac{d\hat{\sigma}_{eg}}{dt} &= -\frac{i}{\hbar}[\hat{\sigma}_{eg}, H_A + H_F + H_I] \\
&= -\frac{i}{\hbar}\Big(\big(\hat{\sigma}_{eg}(H_A + H_F + H_I)\big) - \big((H_A + H_F + H_I)\hat{\sigma}_{eg}\big)\Big) \\
&= -\frac{i}{\hbar}\big(\hat{\sigma}_{eg}H_A - H_A\hat{\sigma}_{eg} + \hat{\sigma}_{eg}H_F - H_F\hat{\sigma}_{eg} + \hat{\sigma}_{eg}H_I - H_I\hat{\sigma}_{eg}\big) \\
&= -\frac{i}{\hbar}\Big([\hat{\sigma}_{eg}, H_A] + [\hat{\sigma}_{eg}, H_F] + [\hat{\sigma}_{eg}, H_I]\Big) \\
&= -\frac{i}{\hbar}\big(\underbrace{[\hat{\sigma}_{eg}, H_A]}_{Term1} + \underbrace{[\hat{\sigma}_{eg}, H_I]}_{Term2}\big)
\end{aligned} \tag{2.22}$$

The term $[\hat{\sigma}_{eg}, H_F]$ is zero because H_F commutes with the atomic operator. Terms 1 and 2 from equation 2.22 need to be evaluated in order to find the equations of motion of the system.

The full derivation of the equations of motion has already been performed for various atomic systems [71,76,80–82] including in publications for the study of calcium [83,84]. The literature can be consulted for a full derivation, which will be not be repeated in this thesis.

From Murray *et al.* [83], the general equations of motion,derived from equation 2.22 for the density matrix elements, are given as follows:

$$\begin{aligned}
\dot{\rho}_{ge} = &-i\Delta_{L,eg}\rho_{ge} - i\sum_{L}\sum_{e'}\Omega^{L}_{e'g}\rho_{e'e} + i\sum_{L}\sum_{g'}\Omega^{L}_{eg'}\rho_{gg'} \\
&- \sum_{\lambda}\sum_{g'}\sum_{e'} g^{\lambda^*}_{eg'}g^{\lambda}_{e'g'}\rho_{ge'}\pi\delta(\omega_\lambda - \omega_{e'} + \omega_{g'})
\end{aligned} \tag{2.23}$$

$$\begin{aligned}
\dot{\rho}_{ee''} = &-i(\omega_e - \omega_{e''})\rho_{ee''} + i\sum_{L}\sum_{g}\omega^{L}_{e''g}\rho_{eg} - i\sum_{L}\sum_{g}\omega^{L}_{eg}\rho_{ge''} \\
&- \sum_{\lambda'}\sum_{g'}\sum_{e'} g_{eg'}\lambda g^{\lambda^*}_{e'g}\pi\delta(\Delta_{e'g'} - \omega_\lambda)\rho_{e'e''} \\
&- \sum_{\lambda}\sum_{g'}\sum_{e'} g^{\lambda^*}_{e''g'}g^{\lambda}_{e'g'}\pi\delta(\omega_\lambda - \Delta_{e'g'})\rho_{ee'}
\end{aligned} \tag{2.24}$$

$$\dot{\rho_{gg''}} = -i(\omega_g - \omega_{g''})\rho_{gg''} + i\sum_L\sum_e \Omega^L_{eg''}\rho_{ge} - i\sum_L\sum_e \Omega^L_{eg}\rho_{eg''}$$
$$+ i\sum_\lambda\sum_{e'}\sum_{e''} g^\lambda_{e'g''}g^{\lambda^*}_{e''g}\pi\delta(\Delta_{e''g} - \omega_\lambda)\rho_{e''e'}$$
$$+ \sum_\lambda\sum_{e'}\sum_{e''} g^{\lambda^*}_{e'g}g^\lambda_{e''g''}\pi\delta(\omega_\lambda - \Delta_{e''g''})\rho_{e'e''} \quad (2.25)$$

where

Δ terms are Doppler detuning between the driving field and the transition frequencies;

Ω^L represent on resonance Rabi frequency between two relevant states e.g $\Omega^L_{e'g'}$ is the Rabi frequency between states e' and g' when the laser is on resonance with the transition;

ω_λ is the frequency of the mode λ;

$\omega_{e'}$ is the frequency of state e' and;

δ are Kronecker delta functions.

The first terms in equations 2.24 to 2.25 represent oscillations between substates of the same state. Terms including the Rabi frequency are coherent driving terms which cause absorption and stimulated of radiation to and from the laser field. The triple sums correspond to the spontaneous emission of photons. For a full review, see Murray *et al.* [83].

2.4 The Two-Level System in calcium

The excitation process where calcium atoms in the 4^1S_0 ground state are promoted to the 4^1P_1 state is shown in figure 2.4. The excited P-state consists of 3 degenerate magnetic substates with magnetic quantum number, m_j=-1,0,+1.

The 4 level system can hence be represented by a 4x4 density matrix:

$$\rho = \left(\begin{array}{c:ccc} \rho_{11} & \rho_{12} & \rho_{13} & \rho_{14} \\ \hdashline \rho_{21} & \rho_{22} & \rho_{23} & \rho_{24} \\ \rho_{31} & \rho_{32} & \rho_{33} & \rho_{34} \\ \rho_{41} & \rho_{42} & \rho_{43} & \rho_{44} \end{array}\right) \tag{2.26}$$

where ρ_{11} describes the ground state. All diagonal elements represent populations in the respective state e.g. ρ_{11} relates to the population of the ground state. As previously mentioned, the off-diagonal elements relate to the coherences between the S and P states e.g. ρ_{12} describes the coherence between level $\mid 1\rangle$ and level $\mid 2\rangle$ i.e. ρ_{12} describes both the amplitude and phase of the wavefunctions representing the states $\mid 1\rangle$ and $\mid 2\rangle$.

The calculations that follow will consider excitation by σ^- polarised radiation. Optical selection rules dictate the state that can be excited depending on the polarisation of the incident light [85]. σ^- polarised radiation results in a change of $\Delta m_j = -1$ and therefore only substate $\mid 2\rangle$ can be excited. σ^+ would cause a change of $\Delta m_j = +1$, exciting the substate labelled $\mid 4\rangle$. Linearly polarised light would result in $\Delta m_j = 0$ causing excitation of level $\mid 3\rangle$.

In the case of σ^- polarised radiation, a 2-level system is set up between the ground state and substate $\mid 2\rangle$ whereby absorption of a σ^- polarised photon causes excitation to the $\mid 2\rangle$ level and the atom may relax back to the $\mid 1\rangle$ state after emission of a photon. The populations of the $\mid 3\rangle$ and $\mid 4\rangle$ levels are assumed to be zero as they can be populated only by π and σ^+ polarised light respectively. Therefore the two-level system can be represented by the following reduced density matrix.

$$\rho = \rho = \left(\begin{array}{c:ccc} \rho_{11} & \rho_{12} & 0 & 0 \\ \hdashline \rho_{21} & \rho_{22} & 0 & 0 \\ 0 & 0 & 0 & 0 \\ 0 & 0 & 0 & 0 \end{array}\right) = \begin{pmatrix} \rho_{11} & \rho_{12} \\ \rho_{21} & \rho_{22} \end{pmatrix} \tag{2.27}$$

as ρ_{33} and ρ_{44} are zero and hence the coherences between these states and any other are also zero.

The general equations of motion 2.23-2.25 will now be solved for the two-level system in calcium. In the case of σ^- radiation, the mode number of the laser, L=-1, the half-Rabi frequency is denoted by Ω_{21}^{-1} and the allowed coupling coefficient is g_{21}^{-1}. Since there is only one ground and one excited state, in the set of equations we may therefore set

$$g = g' = g'' \qquad \text{and} \qquad e = e' = e'' \tag{2.28}$$

Hence for the ground state,

$$\begin{aligned}\dot{\rho}_{gg''} = &-i(\omega_g - \omega_{g''})\rho_{gg''} + i\sum_L\sum_e \Omega^L_{eg''}\rho_{ge} - i\sum_L\sum_e \Omega^L_{eg}\rho_{eg''} \\ &+ \sum_\lambda\sum_{e'}\sum_{e''} g^\lambda_{e'g''}\pi\delta(\Delta_{e''g} - \omega_\lambda)\rho_{e''e} \\ &+ \sum_\lambda\sum_{e'}\sum_{e''} g^{\lambda^*}_{e'g} g^\lambda_{e''g''}\pi\delta(\omega_\lambda - \Delta_{e''g''})\rho_{e'e''}\end{aligned} \tag{2.29}$$

Therefore,

$$\begin{aligned}\dot{\rho}_{gg''} &= -i(\omega_1 - \omega_1)\rho_{11} + i\Omega_{21}^{-1}\rho_{12} - i\Omega_{21}^{-1}\rho_{21} \\ &\quad + g_{21}^{-1}g_{21}^{-1*}\pi\delta(\Delta_{21} - \omega_\lambda)\rho_{22} + g_{21}^{-1*}g_{21}^{-1}\pi\delta(\omega_{-1} - \Delta_{21})\rho_{22} \\ &= -\Omega_{12}^{-1}(\rho_{21} - \rho_{21}) + \underbrace{2|g_{21}^{-1}|^2\pi\delta(\Delta_{21} - \omega_\lambda)}_{=\Gamma_{21}}\rho_{22}\end{aligned} \tag{2.30}$$

where $\delta(\Delta_{21} - \omega_\lambda)$ has been introduced as the decay constant from state $\mid 2\rangle$ to $\mid 1\rangle$. The generalised decay constants are given by [86].

$$\Gamma_{ege'g'} = \sum_\lambda \left[g^\lambda_{e'g'}g^{\lambda^*}_{eg}\pi\delta(\omega_\lambda - \Delta_{e'g'}) + g^\lambda_{e'g'}g^{\lambda^*}_{eg}\pi\delta(\omega_\lambda - \Delta_{eg})\right] \tag{2.31}$$

$$\Rightarrow \Gamma_{eg} = \Gamma_{ege} = 2\sum_\lambda |g^\lambda_{eg}|^2\pi\delta(\omega_\lambda - \Delta_{eg}) \tag{2.32}$$

Hence the final equation for the ground state with σ^- radiation reduces to

$$\dot{\rho}_{11} = i\Omega_{21}^{-1}(\rho_{12} - \rho_{21}) + \Gamma_{21}\rho_{22} \tag{2.33}$$

Similar mathematical manipulation give expressions for ρ_{22}, ρ_{12} and ρ_{21} as

shown below.

$$\begin{aligned}
\dot{\rho}_{22} &= i\Omega_{21}^{-1}(\rho_{21} - \rho_{12}) - \Gamma_{21}\rho_{22} \\
\dot{\rho_{12}} &= i\Omega_{21}^{-1}(\rho_{11} - \rho_{22}) - \left[\frac{\Gamma_{21}}{2} + i(\Delta_{L,21})\right]\rho_{12} \\
\dot{\rho_{21}} &= i\Omega_{21}^{-1}(\rho_{22} - \rho_{11}) - \left[\frac{\Gamma_{21}}{2} + i(\Delta_{L,21})\right]\rho_{21}
\end{aligned} \tag{2.34}$$

Equations 2.33 and 2.34 can be written as a single matrix equation of the form

$$\underline{\dot{\rho}}(t) = \underline{\underline{A}}\underline{\rho}(t) \tag{2.35}$$

where ρ is a column vector with elements ρ_{ij} and A is a complex matrix containing all the coefficients from the general equations above. Equation 2.35 can be integrated to give solutions of the form

$$\underline{\rho}(t) = e^{\underline{\underline{A}}(t)}\,\underline{\rho}(0) \tag{2.36}$$

To solve the equations, a MatLab program was written to calculate the time evolution of $\rho(t)$. As an example, figure 2.5 shows the time evolution of the populations of the states.

The values for the parameters used for the calculations of the evolution of the two level system in calcium are as follows. The intensity of the laser is taken to be 25 mW/mm^2, which is typically used in super-elastic experiments. The decay constant, Γ_{21} for the 4^1P_1 state of calcium is 2.2x10^8 rad s^{-1} [87]. Murray and Cvejanovic [56] have previously determined the Rabi frequency to be (9.95x10$^7\sqrt{I}$) rad s^{-1}. The laser is on resonance with the transition, hence the detuning term is set to zero. The population is normalised such that the sum of ρ_{11} and ρ_{22} is always 1. This shows that under the given conditions, almost 50% of the calcium atoms will be excited from the ground to the excited 4^1P$_1$ state.

As can be seen from figure 2.5, the system eventually reaches a steady state where the populations of the ground and excited states are constant. It is possible to derive expressions for the populations and optical coherences for

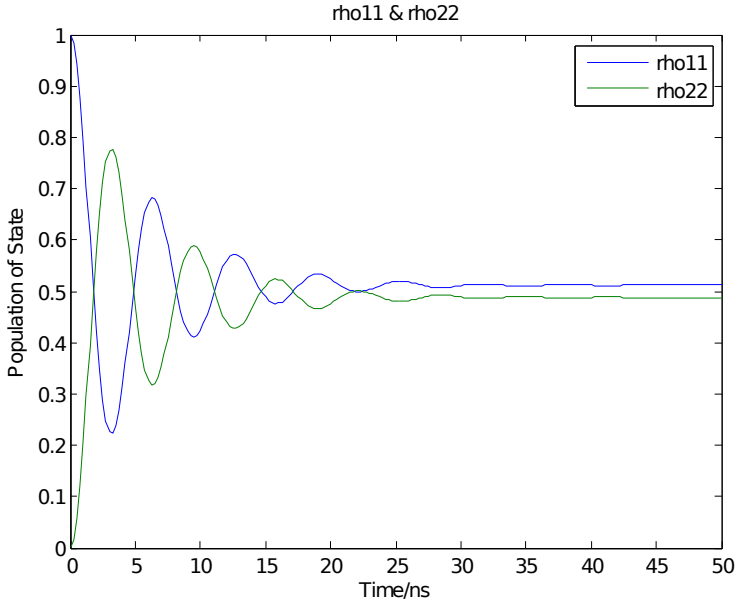

Figure 2.5: *Evolutions of the ground and excited state with time. The vertical axis shows the populations of* ρ_{11} *and* ρ_{22}*.*

the steady state by setting equations 2.33 and 2.34 to zero. This follows from the fact that the rates of evolution of the states, which are derivatives of the populations with respect to time, are zero when the populations are constant. Thus,

$$\begin{aligned}
\dot{\rho}_{11} &= i\rho_{21}^{-1}(\rho_{12} - \rho_{21}) + \Gamma_{21}\rho_{22} = 0 \\
\dot{\rho}_{22} &= i\Omega_{21}^{-1}(\rho_{21} - \rho_{12} - \Gamma_{21}\rho_{22} = 0 \\
\dot{\rho_{12}} &= i\Omega_{21}^{-1}(\rho_{11} - \rho_{22}) - \left[\frac{\Gamma_{21}}{2} + i(\Delta_{L,21})\right]\rho_{12} = 0 \\
\dot{\rho_{21}} &= i\Omega_{21}^{-1}(\rho_{22} - \rho_{11}) - \left[\frac{\Gamma_{21}}{2} + i(\Delta_{L,21})\right]\rho_{21} = 0
\end{aligned} \tag{2.37}$$

By re-writing the equations for the optical coherences in terms of the populations only, an expression for $\rho_{12} - \rho_{21}$ can be obtained which is then substituted in the equations for the populations. This is shown below.

$$\begin{aligned}
\rho_{12} &= \frac{i\Omega_{21}(\rho_{11} - \rho_{22})}{\frac{\Gamma_{21}}{2} + i\Delta_{L,21}} \\
\rho_{21} &= \frac{i\Omega_{21}(\rho_{22} - \rho_{11})}{\frac{\Gamma_{21}}{2} - i\Delta_{L,21}}
\end{aligned}$$

Therefore,

$$\begin{aligned}\rho_{12}-\rho_{21} &= \frac{i\Omega_{21}(\rho_{11}-\rho_{22})}{\frac{\Gamma_{21}}{2}+i\Delta_{L,21}} - \frac{i\Omega_{21}(\rho_{22}-\rho_{11})}{\frac{\Gamma_{21}}{2}-i\Delta_{L,21}} \\ &= i\Omega_{21}(\rho_{11}-\rho_{22})\left(\frac{\Gamma_{21}}{\frac{\Gamma_{21}^2}{4}+\Delta_{L,21}^2}\right)\end{aligned} \tag{2.38}$$

Therefore

$$\begin{aligned}\rho_{22} &= \frac{\Omega_{21}^2(\rho_{11}-\rho_{22})}{\Gamma_{21}} \times \frac{\Gamma_{21}}{\frac{\Gamma_{21}^2}{4}+\Delta^2} \\ &= \frac{\Omega_{21}^2(\rho_{11}-\rho_{22})}{\frac{\Gamma^2}{4}+\Delta_{L,21}^2}\end{aligned}$$

Using the fact that the population is normalised so that

$$\rho_{11}+\rho_{22}=1$$

gives

$$\rho_{22} = \frac{\Omega_{21}^2(1-2\rho_{22})}{\frac{\Gamma^2}{4}+\Delta_{L,21}^2} \tag{2.39}$$

Re-arranging for ρ_{22},

$$\rho_{22} = \frac{4\Omega_{21}^2}{\Gamma^2+4\Delta_{L,21}^2+8\Omega_{21}^2} \tag{2.40}$$

Referring to figure 2.5, the values used in the example given can be put in the equations 2.40 to give the same results. Thus

$$\rho_{22}=0.49$$

2.5 Laser-silver interaction

As previously mentioned, modelling of the laser-interaction with silver is very complex due to the presence of hyperfine structure. The derivation of the general equations of motion in this case follows closely the calculations

performed for sodium and rubidium [71,72]. For the purpose of this thesis which investigates super-elastic scattering using only circularly polarised light, the silver system can be approximated with high accuracy to a two-level system as illustrated in figure 2.6. This is imposed by the selection rules which dictate that the change in magnetic quantum number $m_j = +1$ for σ^+ circularly polarised light and $m_j = -1$ for σ^- circularly polarised light.

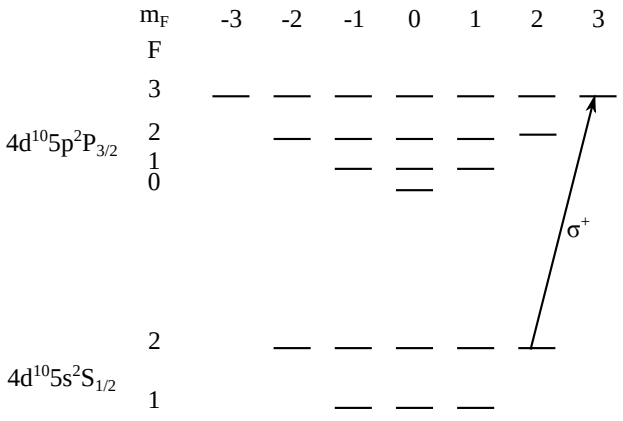

Figure 2.6: *Energy levels of $^{109/107}Ag$ showing the $4d^{10}5s^2S_{1/2}$ ground state and the $4d^{10}5p^2P_{3/2}$ excited state. The use of circularly polarised light at 328.1 nm results in a closed two level system between the $\mid F = 2, m_F = \pm 2\rangle$ and $\mid F = 3, m_F = \pm 3\rangle$ levels. Shown in the diagram is the excitation achieved using left hand circularly polarised light.*

Of particular importance in the theoretical modelling pertaining to the interaction of laser radiation with silver atoms is the consideration of the optical pumping parameters. These parameters are introduced in the interaction of laser radiation with atoms that exhibit hyperfine structure. It has been shown that the magnitude of the optical pumping parameter related to circularly polarised light, K', is close to unity at all but very weak laser intensities [47,88,89]. Typical values are calculated to be $\sim$0.998. For this project, K' has hence been taken as unity.

2.6 Conclusion

This chapter has provided an overview of the theoretical formalism employed in the description of the super-elastic experimental data. A density matrix was introduced to describe the excited atomic system under consideration, whose elements relate to alignment and orientation parameters. These parameters were defined for an S-P transition in calcium. Furthermore, it was noted that the density matrix elements relate to theoretically calculated scattering amplitudes and therefore a comparison between experimental data and theory can be made through these parameters. The above treatment was derived based on the equivalence of the electron-photon coincidence and super-elastic experiments since scattering theories consider inelastic collisions in their derivations.

In the second part of the chapter, a QED model of the interaction of the laser field with calcium was introduced. The general equations of motion were used to allow determination of the population and optical coherences of the two-level system in calcium. An example of the evolution of the atomic system with time was shown and it was concluded that ~ 50 % of the calcium atoms are excited to the 4^1P_1 energy level when the system has reached a steady state. The relevance of the optical pumping parameters in the case of laser-silver interaction was highlighted. Since the experiments on silver used circularly polarised light, it was noted that K', the optical pumping parameter for super-elastic scattering is close to unity. Hence in this thesis the value of K' for the super-scattering experiments with silver was taken as unity when determining the relevant ACPs in chapter 7.

Chapter 3

Experimental Apparatus for Calcium Super-elastic Scattering

3.1 Introduction

Super-elastic studies from calcium were carried out in a special, purpose-built scattering chamber which was evacuated to low pressures of around $2x10^{-7}$ mbar under operation. The chamber housed the atomic beam sources which are the calcium oven and the gas jet. The calcium atoms were excited from the 4^1S_0 ground state to the 4^1P_1 excited state by a resonant laser beam at 423.29 nm. An electron gun generated a beam of electrons with well defined momentum and energy which was directed onto the excited atoms at the interaction region. Electrons that were scattered after collision with the target atoms were detected using an electron energy analyser. All parts of the spectrometer were manufactured from 310 grade stainless steel and other non-magnetic materials, as required due to the sensitivity of the experiment to magnetic fields. The experiment was computer-controlled and could run unmanned so long as no maintenance was required.

The chamber housed the electron gun, electron energy analyser and atomic beam sources. A rotary motion feedthrough was employed to move the analyser around the turntable in order to access a range of scattering angles. A computer-controlled stepper motor connected to the rotary feedthrough was used to move the analyser. The gun and oven were both fixed in position.

This chapter presents the set-up for the electron collision experiments using calcium as described in this thesis. Most of the apparatus was developed prior to the present work and has already been described in detail [84]. The system will here be briefly described in the following sections but the reader may refer to the abovementioned reference for additional details. Section 3.2 introduces the vacuum chamber which contained the essential components that are individually described in the sections that follow on.

3.2 The Vacuum Chamber

The vacuum chamber is a vertical stainless steel cylinder shielded with mu metal to reduce the effects of magnetic fields to less than 3 mG at the interaction region. A flange to which were attached most components of the experiment including the oven and electron gun, rested directly on top of the cylinder. A vacuum seal was created between the flange and the chamber by means of a Viton O-ring. The top flange also carried all electrical connections to the various elements within the chamber via appropriate electrical feedthroughs. A CF-70 window, centrally located on the flange let the laser radiation into the chamber. Four other viewing windows were located on the side of the chamber.

3.2.1 The Spectrometer

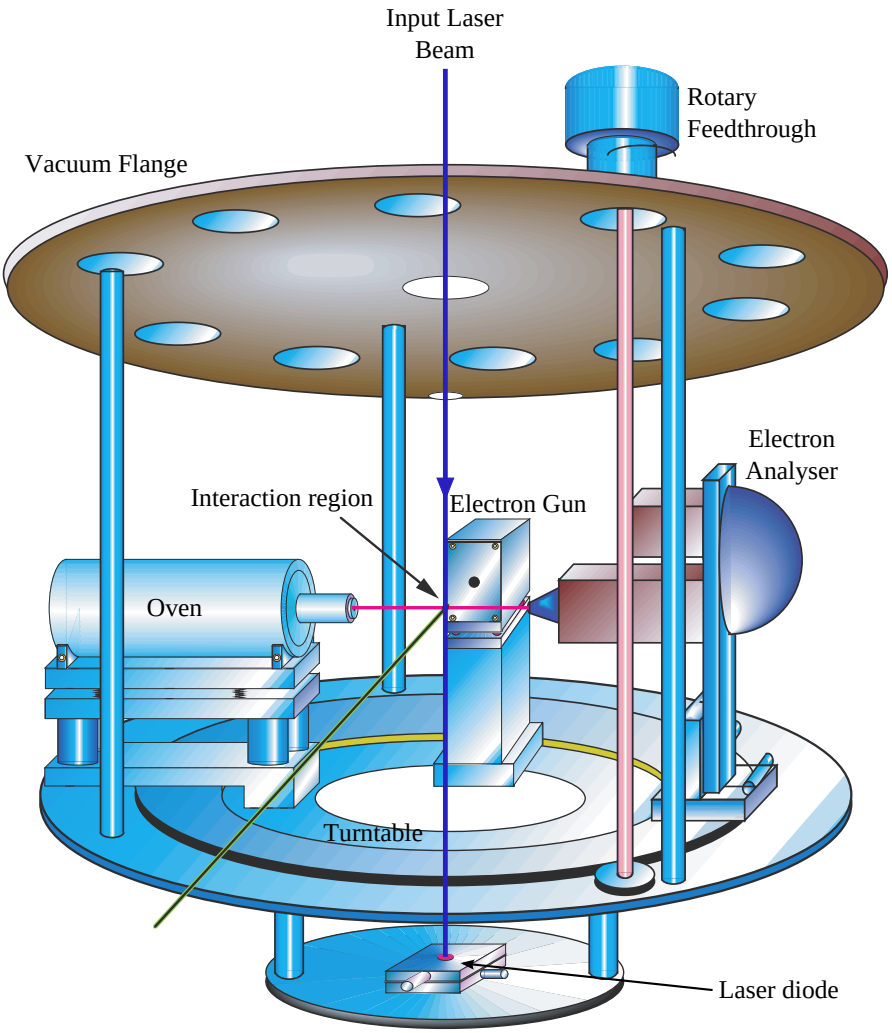

Figure 3.1: *Diagram of the spectrometer used in the study of super-elastic scattering from laser-excited calcium atoms. The relative positions of the oven, electron gun and the energy analyser are shown. The laser radiation was let into the chamber through the central CF-70 window. The atomic beam, electron gun and laser light intersect at the interaction region. Also shown is a laser diode which was used to align the main laser beam to the interaction region.*

The chamber was evacuated using a BOC Edwards E1M18 [90] single stage direct drive rotary pump which lowered the pressure to about 10^{-2} mbar. At this stage a Leybold Turbotronic NT 150/360 turbomolecular pump [91] was switched on to further reduce the internal pressure. The typical operating

pressure was about $2x10^{-7}$ mbar. The vacuum pressure was measured using a Leybold ITR 90 Hot Ion Combi Gauge [92]. A control box was used to power the gauge and this also output the pressure measurement to the controlling computer. The pressure could hence be continuously monitored throughout the experiment. When the chamber needed to be opened for maintenance purposes, it was vented to nitrogen gas after the pumps had formerly been deactivated.

A liquid nitrogen cold trap connected to a cold finger through which liquid nitrogen was circulated, was located directly opposite the oven nozzle. This trapped the calcium atoms that had passed through the interaction region and also lowered the pressure of the tank by cold trapping impurities. A Faraday cup, consisting of a curved metal plate behind a fine tungsten mesh, was also located on the side of the chamber to catch electrons that had passed directly through the interaction region from the electron gun.

3.3 Atomic Beam Sources

3.3.1 Gas Jet Nozzle

Gases including helium and argon were often used especially in the preliminary stages of the experiments for calibration, diagnostic and tuning purposes. Gaseous targets were introduced into the chamber by means of a gas jet nozzle.

Helium was used to calibrate the gun energy. The gas jet nozzle connected via a feedthrough to the external gas line. This gas line could be evacuated using a rotary pump. A needle valve was used to regulate the flow of gas into the chamber. A gas bottle containing the gas of interest connected to the gas-line using a regulator with a valve. With the needle valve closed, the gas-line was then filled with the target gas. The gas bottle was closed and the line was evacuated. This was repeated several times in order to flush the line of any contaminants. The gas bottle was then opened. With a pressure of about 1 bar in the gas line, the needle valve was slowly opened to allow gas into the interaction region in a controlled manner. Typical gaseous pressures that were used are about $1x10^{-5}$ mbar.

3.3.2 The Calcium Oven

The calcium beam needed for the experiment was produced from a custom made non-magnetic 310 grade stainless steel oven. The oven consists of a crucible in a furnace heated by the use of heating coil through which current is passed. A length of about 2.5 m of twin-core wire from Thermocoax (Metraware) [93] was wound along inbuilt helical grooves on the external surface of the furnace. The crucible which contained the target material was a thin-walled hollow cylinder closed at one end and with a 1.4 mm ID nozzle at the other end.

Calcium is a reactive metal and oxidises readily in air to form a grey-white oxide coating. It also reacts slowly but noticeably with water. The calcium charge therefore had to be carefully handled. It was also desirable to maintain the purity of the sample which was in the form of pellets. Calcium pellets were loaded into the crucible. Handling of the calcium and refilling of the crucible were carried out in an Atmos bag filled with argon gas which provided an inert atmosphere to prevent oxidation of the metal. An illustration of the various parts of the assembled calcium oven is presented in figure 3.2.

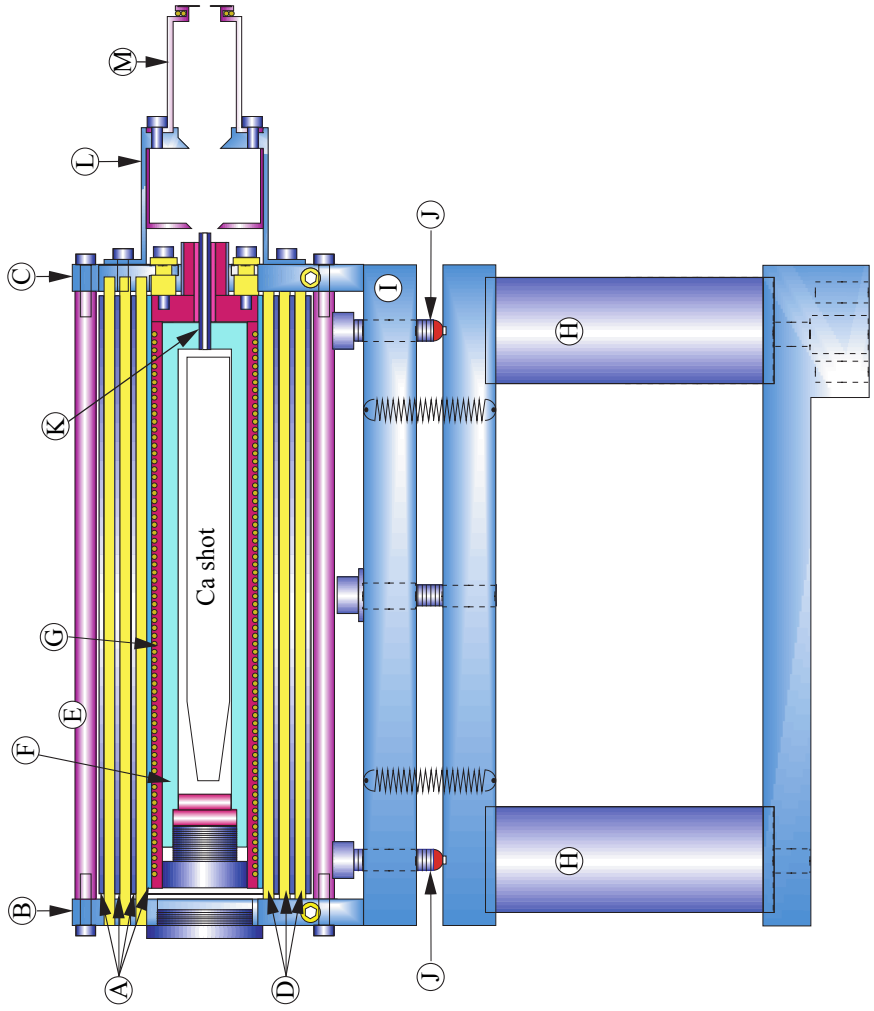

Figure 3.2: *Schematic diagram of the inside of the oven. Various parts are labelled and a short description of each is given in table 3.1.*

Label	Description
A	Heat shields
B	Rear face plate
C	Front face plate
D	2 mm thin-walled ceramic rods
E	Stainless steel rods
F	Oven crucible sealed at the back
G	Oven heater
H	Adjustable stands
I	Base plate
J	Adjusting screws
K	2 mm OD molybdenum nozzle
L	Skimmer assembly
M	Defining aperture for atomic beam

Table 3.1: *Description of the various parts of the calcium oven as labelled in figure 3.2.*

Once filled, the crucible was inserted into the heater furnace, made out of oxygen-free copper and shaped into a cylinder with a spout from which the nozzle of the crucible protruded. An outer jacket made from stainless steel slid onto the furnace thus ensuring optimal contact of the heater wire with the copper surface by pressing the heating coil firmly into the grooves. Current was passed through the heating coil to raise the temperature of the crucible to approximately 800°C. This caused the calcium to sublime and the resulting vapour then escaped the crucible via the nozzle (K).

The atomic beam oven produced a beam of calcium with a density of about 10^9 atoms cm^{-2} at the interaction region [94]. The beam had to be well collimated so as to reduce scatter and unwanted deposition onto internal surfaces of the chamber. Atomic beam collimation was achieved through the use of a skimmer and aperture arrangement at the front of the oven (L, M) as shown in figure 3.2. The purpose of the cylindrically shaped skimmer was to trap a proportion of the atoms that diverged as they left the crucible, the result being a collimated beam with limited angular spread as the atoms leave the aperture at the front of the skimmer. The atomic beam has previously been measured to be approximately 2mm at the interaction region [94].

The beam was directed towards the interaction region by careful alignment, and the atoms condensed onto the liquid nitrogen-cooled plate on the opposite side of the chamber after passing through the interaction region. The task of alignment was achieved by replacing the crucible with a custom-made cylinder into which a laser diode had been fitted. Adjustment of six screws on the baseplate (I) as shown in figure 3.2 allowed the height and tilt of the oven to be altered.

3.4 The Electron Gun

The electron source used in the calcium super-elastic experiments produced a well-controlled beam of electrons, of well-defined momentum and energy, aimed at the interaction region. The design of the electron gun made use of electrodes held at different voltages which cause the electric potential to vary with position thus creating electrostatic lenses whose effects are similar to thick optical lenses.

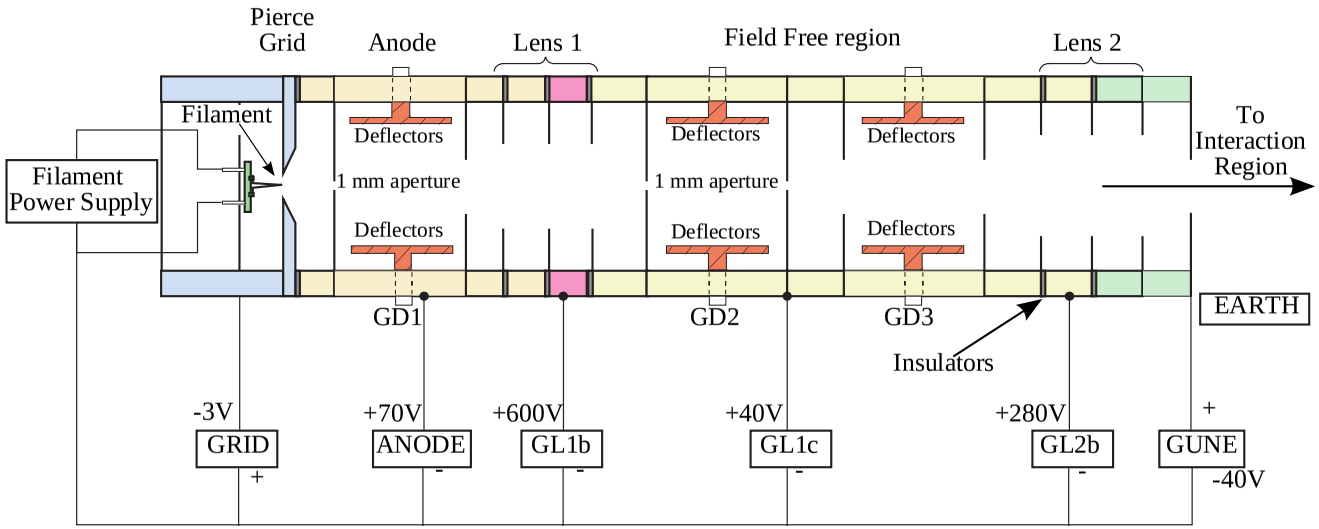

Figure 3.3: *Schematic diagram of the electron gun showing the different elements: grid, anode, lenses and deflectors together with typical voltages required to produce a well collimated beam. GL1b and GL2b are the focussing elements of the lenses and GD1, GD2 and GD3 are the x-y deflectors.*

A schematic representation of the gun is shown in figure 3.3. The gun can be thought of as a two-stage system consisting of an electron generation section and a beam manipulation section which delivers the electrons to the target region. The generation section uses a tungsten hairpin filament cathode which emits electrons thermionically when heated. The filament is heated using an external constant current power supply. After emission, the electron beam is first shaped by the combination Pierce electrode grid and anode as shown in figure 3.3.

Following the anode are two triple-element electrostatic lenses and three sets of deflectors. The function of this section is to accelerate, steer and focus the thermally produced electrons into a well-collimated beam. A series of power supplies mounted in a rack were used to adjust voltages on the lens elements and the deflectors so as to tune and direct the beam. Typical voltages are shown next to their respective element in figure 3.3.

The grid ensures the electron beam is shaped into a relatively collimated beam. The electrons are then accelerated from the filament by the anode held at a positive potential with respect to the filament. The electrons that pass the interaction region are collected on the opposite side of the chamber on a Faraday Cup. With a current of just under 2A through the filament, electrons are released and a current of a few hundred nanoamps is registered at the Faraday Cup.

The lenses and deflectors provide control over the shape and energy of the resulting beam. The first lens is formed from the three potentials marked ANODE, GL1B and GL1C. The second lens is formed by GL1C, GL2B and the exit aperture of the gun which is held at ground potential. The energy of the outgoing electron is determined by the GUNE voltage or gun potential. The filament is held at this voltage (GUNE) and other voltages are referenced to this voltage. Since the final section of the gun is held at 0 V, electrons emerge from the gun with an energy set by $-V_{GUNE}$ in theory. In practice, however the measured energy of the electrons was different due to contact potentials which were measured regularly as noted in section 4.2.1.

The focal lengths of the two lenses are adjusted by voltages marked GL1B and GL2B as shown. The 1-mm apertures in the field-free region, directly before and after the second set of deflectors serve to collimate the beam by defining the pencil and beam angles at the interaction region. The deflectors are used to steer the beam and correct for any mechanical misalignments of the gun elements, using the voltages marked GD1, GD2 and GD3. The deflectors are essentially made of two pairs of parallel plates which allow for transverse adjustment of the electron beam. The final set of deflectors allow the electron beam to be directed to the interaction region. The apparatus sets the beam angle to be zero and the pencil angle to be 2^{o}.

3.5 The Electron Analyser

Electrons scattered from the interaction region were detected as a function of energy and angle by an electron energy analyser. A schematic diagram of the analyser is shown in figure 3.4. The electrons entered the analyser through an aperture in the cone at the front of the analyser as shown and were focussed by a three-element cylindrical electrostatic lens which imaged the selected electrons at the entrance aperture of a hemispherical energy selector. The lens is formed by the analyser aperture section which sits at earth potential, A1L1B and A1AM. The third lens element A1AM accelerates or decelerates the electrons to the energy selector's pass energy, E_o. Voltages to each of the element of the analyser can be controlled by external rack-mounted power supplies.

The hemispherical energy selector consists of two concentric hemispheres constructed out of molybdenum which are held at two different specific voltages. The design is based on the one detailed in the reference [95]. The potentials to the inner and outer hemispheres are controlled externally by means of voltages A1IH and A1OH. Selection of the resolution of the analyser occurs by changing the analyser pass energy which is the desired energy for electrons to pass through the selector. The energy of the electrons selected by the analyser is achieved by setting the residual energy A1RSE which sets a bias voltage to the whole analyser with respect to ground.

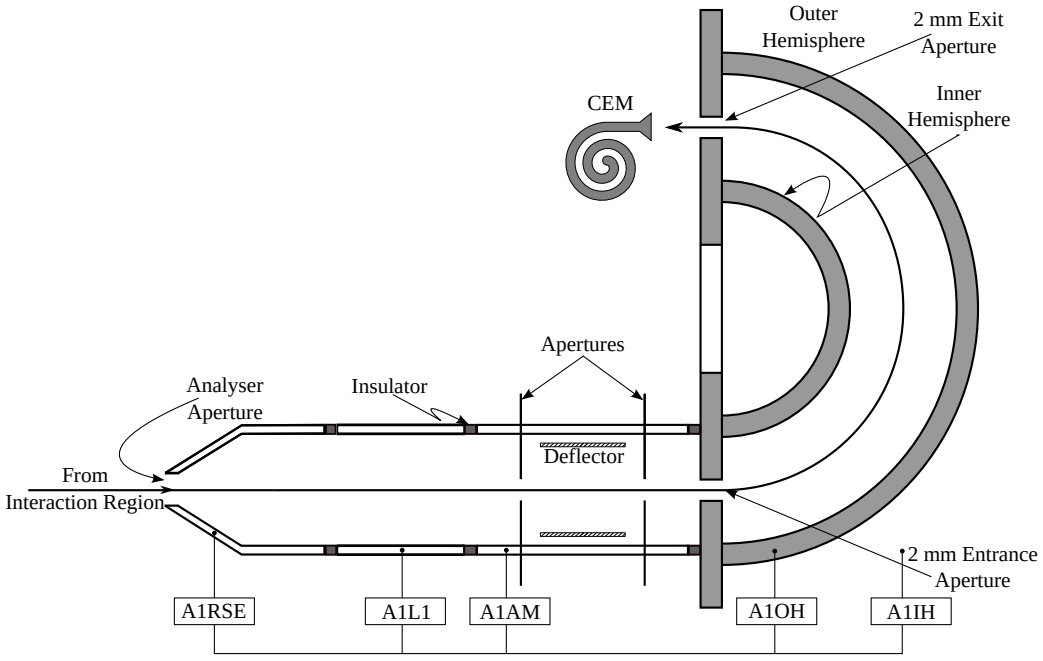

Figure 3.4: *Schematic diagram of the inside of the analyser. Connecting voltage supplies are shown. The potential A1IH is electrically connected to the inner hemisphere. Electrons entering at the residual energy A1RSE are detected by the CEM.*

An electron entering the analyser with an energy equivalent to the residual energy will have its energy altered by the potential A1AM such that it reaches the entrance aperture to the selector with an energy equal to the pass energy. The pass energy is set by the mean voltage, A1AM.

The electric field in the region between the two hemispheres causes the electrons of the required energy to follow a curved path through the selector along the curved path as shown in figure 3.4. The electrons leave the selector through the exit aperture to enter the channel electron multiplier(CEM). On the other hand, if an electron enters the analyser at an energy that is different to the residual energy it will not be at the pass energy at the entrance hole of the selector. Consequently, it will not follow the curved path and will not exit into the channel electron multiplier. Electrons of energy greater than the pass energy will be less deflected whereas less energetic electrons will be more deflected and follow a path of greater curvature.

The voltages to the hemispheres are established using [84]

$$V_1 = V_o \left(\frac{2R_o}{R_1} - 1 \right) \tag{3.1}$$

$$V_2 = V_o \left(\frac{2R_o}{R_2} - 1 \right) \tag{3.2}$$

where V_0 is the potential of the curved path; R_1, R_2 are the radii of the inner and outer hemispheres respectively.

$$R_o = \left(\frac{R_1 + R_2}{2} \right) \tag{3.3}$$

The analyser was fixed to a turntable inside the spectrometer. It could be rotated within the scattering plane whilst always pointing at the interaction region, by turning an external mechanical feedthrough on the top flange of the chamber. By rotating the analyser around the interaction region, electrons at specific angles could be detected. The entrance aperture at the front of the analyser limited the angular acceptance to $\pm 3^o$. Thus the analyser was able to discriminate between electrons for a range of scattering angles, θ_e.

The range of angles that the analyser swept through is determined by the geometrical arrangement of other components in the chamber. The analyser could access angles up to θ_e=+145° in the forward direction before being restricted any further by the gun, and θ_e=-97° in the opposite direction where it ran into the gas nozzle. These geometrical restrictions can be seen in figure 3.1 on page 53. Furthermore, there were additional restricted ranges in the forward direction. Angles from -20° to +20° where the analyser was directly opposite the electron gun were purposefully avoided, because it is known that a high flux of electrons into the analyser could damage the detector. The analyser was also not placed directly in front of the atomic beam sources (calcium oven or gas jet) for the same reason.

3.6 The Channel Electron Multiplier

The electrons exiting the hemispherical analyser were detected by an X719BL Channel Electron Multiplier (CEM) which is a sensitive charged particle detector. The CEM was found inside the analyser at the exit of the hemispheres and it detected the electrons. It consists of a hollow spiral with an open cone at one end where electrons can enter. An HT power supply provided a high voltage of about 3kV which is applied to the CEM.

After entering the CEM, electrons are accelerated and collide with the inner wall. This collision releases more electrons which are again accelerated to produce more collisions. An avalanche effect is thus created which builds up the number of electrons, with a gain of about 10^8. Thus the interaction of a single electron with the inner wall is able to create a current which can then be measured. The channel is curved to prevent ionised molecules from the background gas colliding backwards into the wall of the CEM. This could release more electrons which would give rise to after-pulses thus altering the measurement. The curvature of the channeltron prevents these ions having sufficient energy to produce secondary electrons.

The CEM is able to detect electrons and with the appropriate electronics, it is possible to count single electron scattering events. Each detector event results in a pulse by the emission of secondary electrons. This pulse was pre amplified by a wideband amplifier (Phillips 6954 B50) which amplified the pulse from tens of mV to about 2V for processing in the electronics. The output from the amplifier was then fed into a constant fraction discriminator (CFD) which discriminates the pulses from low level background noise. The pulse from the CFD was then split into three counting devices: (i)a ratemeter Ortec 4492 provided an audible and a visual analogue display of the count rate, (ii) an Ortec 771 digital counter which displayed the accumulated number of detection events since it was last reset and (iii) an Ortec 871 digital counter which displayed the number of detection events over a pre set period of time. The output from the CFD was also passed to a Labview PCI-6621 digital acquisition (DAQ) card inside the control PC of the experiment.

3.7 Liquid Nitrogen Cold Trap

Following emission the atoms leaving the interaction region eventually deposited on a cold trap located directly opposite the atomic beam oven. The cold trap is made out of a non-magnetic stainless steel plate. The cold trap was cooled using liquid nitrogen to a temperature of about -200°C. Liquid nitrogen was fed via copper pipes to the cold plate.

The target atoms condensed on the cold trap after they had gone through the interaction region thus preventing the atoms from depositing onto other components of the spectrometer. This is especially important in the case of certain elements such as calcium, as a deposition of calcium atoms onto other parts of the instrument may degrade them or introduce inaccuracies in measurements. Moreover, the cold trap improved the background vapour pressure inside the chamber by allowing other gases and water vapour internally present to also condense and get trapped. Indeed when the cold trap was activated after the chamber had been formerly evacuated, a significant decrease in pressure was observed from about $3x10^{-6}$ mbar to about $5x10^{-7}$ mbar.

The cold trap was fed via quarter-inch copper pipes from a dewar as shown in figure 3.5 on page 66. This dewar was located above the cold trap so that the liquid flowed under the action of gravity. It is made up of two concentric cylindrical chambers constructed from commercially available 316 grade stainless steel following a previous design [96] . The outer cylinder acted as an external wall while the inner one contained the liquid nitrogen. The space between the two cylinders was evacuated by the pumping process in the main chamber. This limited thermal conduction to the liquid nitrogen.

The dewar was closed using a top flange where an O-ring created a vacuum seal. A length of heater wire was wound around the flange and a current was then run through in order to maintain the seal at a higher temperature (above 0°C) than the rest of the vessel. This ensured the seal did not fail as a result of freezing at low temperatures. Two protruding stainless steel venting holes were welded onto the top flange, one for influx of liquid nitrogen and the other to let out nitrogen vapour from the dewar as the liquid boiled off. A full dewar could

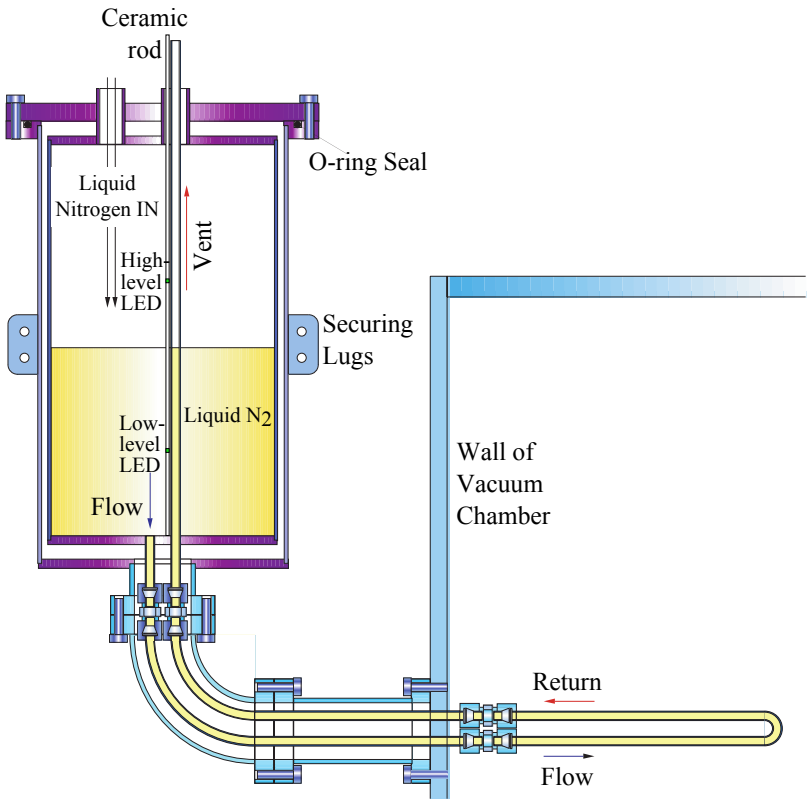

Figure 3.5: *Illustration of the liquid nitrogen dewar as used in the super-elastic experiment.*

last up to five hours when the experiment was running at its operating temperature. The dewar was topped up by an automatic refiller [97]. This switched on a pump that filled the dewar from an external reservoir of liquid nitrogen. The fill level detection mechanism used two green light emitting diodes (LEDs). The changes in potential difference across the LEDs with changes in temperature were employed to detect the fill level. The two LEDs, shown in figure 3.5 were attached at the top end (high-level LED) and bottom end (low-level LED) of a ceramic rod which was suspended from the top plate of the dewar through a purpose built hole. When liquid nitrogen was pumped into the dewar and reached the maximum fill level, the pump stopped the filling process.

As the liquid nitrogen boiled off and reached a level below the lower LED, the controller detected this and restarted the pump in order to refill the dewar. Thus the level of liquid nitrogen was maintained between a minimum and a

maximum level as long as the dewar was connected to an external source of liquid nitrogen.

3.8 The Laser System

The super-elastic calcium experiments conducted in this project were performed using a single-mode continuous wave laser source, a Spectra-Physics Matisse TX Ti:Sapphire laser pumped by a Millenia Pro 15sJS laser. Additionally, the laser was tunable and its frequency could be set to that of the atomic transition in calcium; it was stable and provided sufficient power to carry out the super-elastic experiments. A block diagram of the laser system is presented in figure 3.6. The Millenia Pro 15sJS is a diode-pumped solid state laser which produces continuous wave green light at 532 nm with a power of up to 15W . It consists of a laser head unit and a power supply. This laser utilises a neodymium vanadate crystal as the gain medium inside the laser cavity. Two diodes housed in the laser head pump power to the crystal which lases at 1064 nm. To produce the output radiation at 532 nm, an intra-cavity temperature-tuned lithium triborate (LBO) crystal is employed as the doubling medium for second harmonic generation.

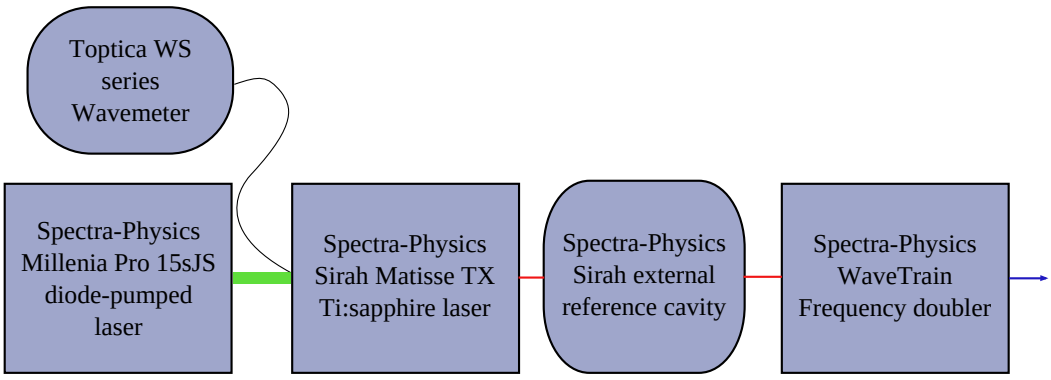

Figure 3.6: *Block diagram showing the laser system used in the super-elastic experiments with calcium atoms. The Millenia Pro laser operating at 532 nm pumps the Ti-sapphire laser which produces a continuous wave, single frequency tunable infra-red laser light. The external reference cavity stabilises the laser frequency. The infra-red light produced from the Ti:Sapphire at 846 nm is then frequency doubled by the Wavetrain frequency doubler. Blue light at 423 nm is then generated.*

The green light output from the Millenia Pro laser is in turn used to pump the Matisse TX laser [98]. Its active lasing element is a titanium sapphire crystal, where sapphire has been doped with titanium ions, Ti^{3+} in replacement of aluminium ions, Al^{3+} at some lattice points. When excited by the incident pump light, the crystal emits radiation over a wide range of frequencies in the infra-red region but a desired single frequency can be isolated by minimising losses at that particular frequency inside the laser cavity. For the super-elastic experiments, the laser was operated at a single frequency and was stabilised during operation by an external reference cavity.

A schematic illustration of the laser system is shown in figure 3.7. The birefringent filter (D) is used for coarse wavelength control. The piezo driven thick etalon further narrows the frequency range and the thin etalon is the final frequency selector which allows fine tuning of the laser frequency. The birefringent filter works by rotating the polarisation of light whose wavelengths differ from the centre wavelength. The Matisse TX laser has a ring cavity implying two counter propagating modes could exist at one frequency. In order to ensure light propagation in one direction only, the Faraday rotator (E) together with mirrors M2 and M3 act as an optical diode ensuring uni-directional light propagation by producing high losses in the opposite direction.

It was important to maintain the laser at the desired frequency for the super-elastic experiments, and so an external reference cavity was employed to carry out this function. The reference station contains the reference cavity and additional optical elements for frequency stabilisation using the Pround-Drever-Hall technique [99]. This method works by measuring the laser frequency using a Fabry-Perot cavity and an error signal is then fed back to the laser to extinguish fluctuations in frequency [100]. By looking at the reflected light from the reference cell it can be established whether the cavity is on resonance or not; no reflected light should be detected when the laser is resonant with one of the cavity modes of the reference cell. When the laser frequency is near resonance with a cavity mode, the reflection coefficient F is proportional to the difference between the laser's frequency and the cavity's resonant frequency δf [101].

However, because the reflected light is symmetric about resonance, by simply detecting the reflected signal, it is not possible to establish whether the laser frequency needs to be increased or decreased to bring it back onto resonance with the cavity [100]. The derivative of the reflected signal (F) with respect to δf, on the other hand, is asymmetric about resonance. Above resonance, with a positive F derivative, the intensity responds in phase with the frequency variation. Conversely, below resonance, the beam intensity responds with opposite phase. The derivative therefore provides an error signal which is proportional to the frequency offset and indicates the direction in which the laser frequency needs to be adjusted.

To determine the derivative of the reflected signal, an electro-optic modulator (EOM) located before the reference cell is used to modulate the laser frequency. After the laser beam has been modulated by the EOM, it passes through the cavity and the reflected signal is measured using a photodetector. The portion of the signal which measures the derivative of the reflected signal can be isolated. This is then fed back into a servo amplifier to adjust the laser frequency in order to bring the laser back to resonate with the reference cavity.

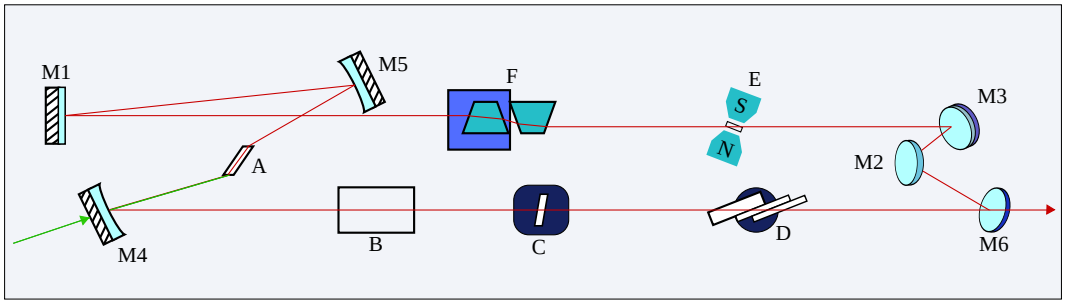

Figure 3.7: *Schematic illustration of the Matisse TX Ti:Sapphire laser showing the principal optical components. (A)Ti:Sapphire crystal. (B) EOM. (C) Thin etalon. (D) Birefringent filter. (E) Faraday rotator. (F) Piezo-controlled thick etalon. (M1) Tuning mirror. (M2) Out-of-plane mirror. (M3) Tweeter mirror. (M4,M5) Folding mirrors to focus pump laser radiation into Ti:sapphire crystal. (M6) Output coupler.*

The Wavetrain frequency doubler [102] utilises an SHG (Secondary Harmonic Generator) crystal to double the frequency of the infra-red laser radiation out of the Matisse TX laser, at a laser wavelength of 846 nm. Blue laser

radiation at the required wavelength of 423 nm is then produced. An optical schematic illustration of the doubler is shown in figure 3.8. The crystal (D) inside the doubler exhibits non-linear optical behaviour such that light passing through it creates optical disturbances at the input frequency as well as at harmonic frequencies. In the case of the SHG crystal, second harmonic waves are generated. By mounting the crystal inside a resonant enhancement cavity, the efficiency of second harmonic generations is greatly increased. The Wavetrain frequency doubler makes use of a triangle-shaped cavity configuration called the DeltaConcept^{TM} and is formed by two mirrors, M1 and M2 and a prism (C). The prism is mounted on a piezo which allows the cavity length to be altered while the output beam position remains unaffected. The EOM(A) modulates the incident laser radiation and the reflected signal from M1 is analysed and the piezo adjusted.

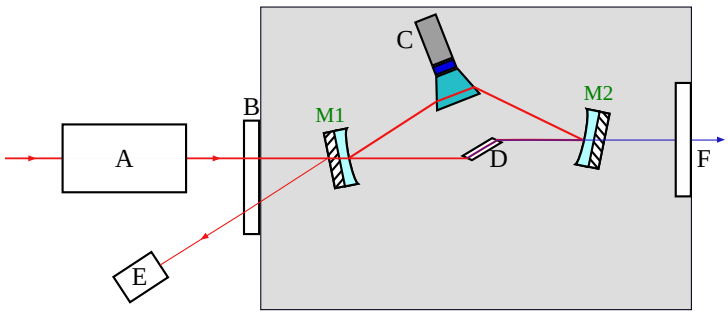

Figure 3.8: *Schematic diagram of the Wavetrain frequency doubler showing the main optical components. Labelled are (A) EOM used for frequency stabilisation using Pound Drever Hall technique. (B) Brewster window. (C) Prism and piezo mount. (D) SHG (doubling) crystal. (E) Fibre-optic coupler for reflected signal. (F) Brewster window.*

3.9 The Laser Locking System

It was necessary to keep the laser frequency on resonance with the atomic transition in calcium in order to maintain a uniform optimal density of atoms in the excited state. Although the laser system was initially set up to be on resonance with the atomic transition, the laser frequency tended to drift slowly over time as a result of external changes such as the ambient temperature. To stabilise the laser frequency over extended periods of time so as to enable data

collection, an external locking system was used based on the observed laser-induced fluorescence of the excited calcium atoms at the interaction region.

In the given configuration used for the super-elastic experiments, the laser light was introduced in a direction perpendicular to the atomic beam oven (i.e. orthogonal to the scattering plane). The atoms exiting the effusive oven spread out of the oven nozzle in a direction orthogonal to the laser beam. The transverse velocity component of the atoms introduced a Doppler shift, whereby only a portion of the atomic beam was on resonance with the laser. Those atoms that were emitted in a line perpendicular to the laser beam had no velocity component in the direction of the laser beam and were therefore exactly on resonance with the laser. However atoms that spread away from the laser beam had a velocity component in that direction and the laser light was shifted towards the blue end of the spectrum with respect to their frame of reference. When these atoms were fluorescing, the position of the fluorescence spot would shift from the centre in the direction of the laser beam. Hence any fluctuations in frequency could be observed as a movement in the laser-induced fluorescence. This is illustrated in figure 3.9.

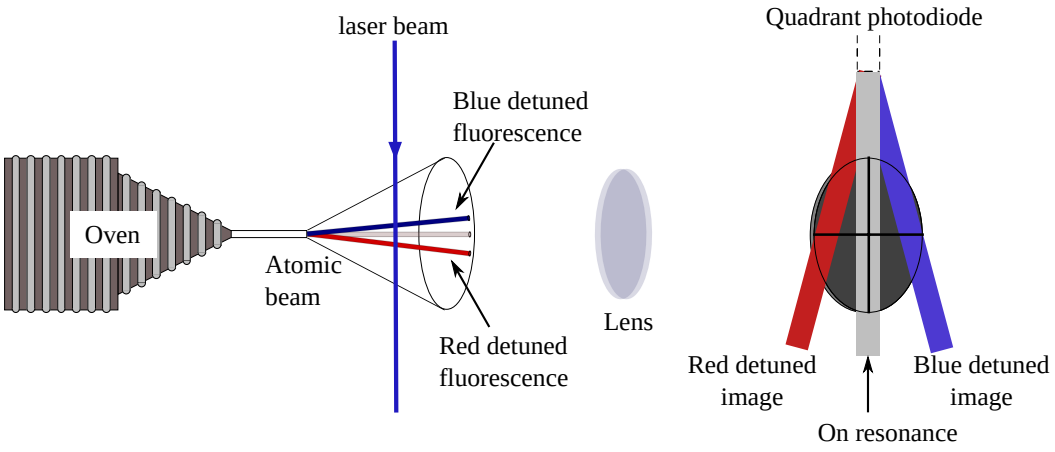

Figure 3.9: *Illustration of the laser-excited atoms imaged onto the quadrant photodiode. The effect of detuning resulting into a shift in the fluorescence spot can be seen.*

The fluorescence produced by the interaction of the atoms with the laser

beam was imaged by means of a lens onto a QD50-5T quadrant photodiode outside one of the side windows of the interaction chamber. Any change in the position of the fluorescence image could be inferred from a change in the relative intensity in each of the quadrants of the photodiode. The photodiode worked in a split way: the sum of the signals from the two left detectors and the sum of the two right detectors constituted the two signals. When the fluorescence was central and both halves of the photodiodes detected equal amounts of light, the difference between their voltages was zero implying the laser was on resonance. On the other hand, any difference between the two halves of the quadrant photodiode was amplified and fed back, via appropriate electronics, to the external scan control of the laser. This feedback worked to adjust the frequency of the laser so as to bring it back into resonance with the atomic transition. This locking system was able to stabilise the laser frequency to better than 3MHz [103]. This then ensured the laser beam remained on resonance with the atomic beam for periods of time up to several days.

3.10 The Optical Setup

The laser system produced laser radiation at 423.29 nm which was resonant with the 4^1S_o- 4^1P_1 transition in calcium. A number of high-quality optical components were used to prepare the laser beam as required for the superelastic experiments. These are illustrated in figure 3.10 on page 73. The beam first passed through a lens which imaged the light such that it produced a spot size of $\sim$2 mm at the interaction region. With this beam size, the probability of atomic excitation increased and the efficiency of the scattering process was in turn improved. A mirror(M1) then steered the laser beam to pass centrally through the vacuum window into the chamber. The beam was accurately aligned to go through the interaction region whilst remaining orthogonal to the scattering plane. This was achieved by making the main laser follow the path of a counter-propagating laser beam from a visible laser diode operating at 650 nm. The visible laser diode was internally located at the bottom of the chamber. Prior to closing the spectrometer the diode was precisely aligned using a set of non-magnetic oil-free vacuum XY translators such that the laser beam

passed vertically upwards through the interaction region. The polarisation state

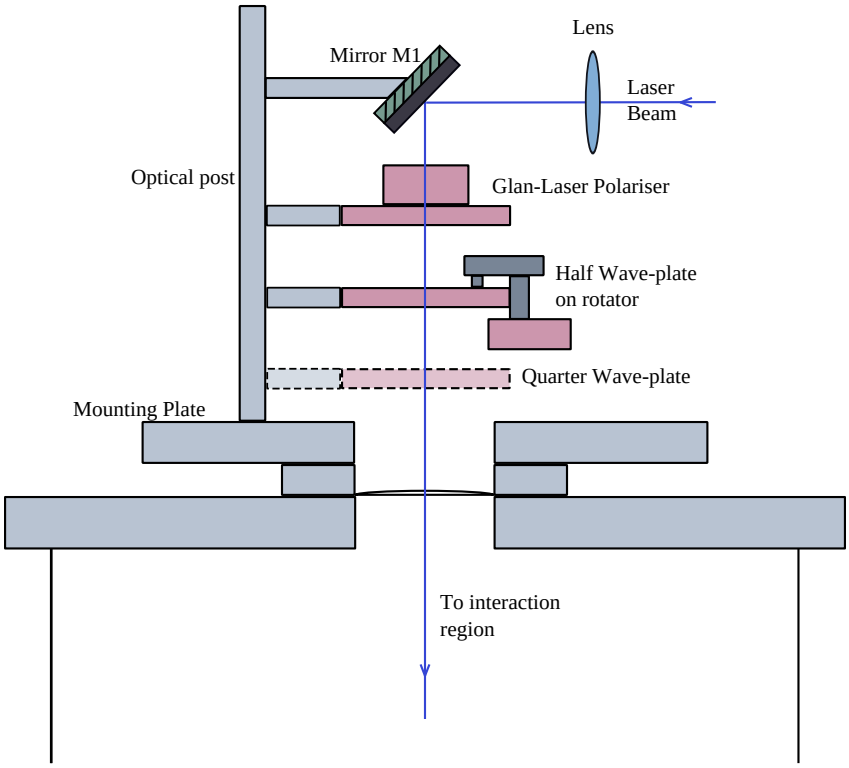

Figure 3.10: *Optical components that steer, focus and deliver the laser beam to the interaction region as required. The laser beam was directed into the chamber by the angled mirror M1 after going through the lens. The Glan-Laser polariser and the two wave-plates provided control of the polarisation of the light. The optical components were mounted on an optical post.*

of the laser was set using a Glan-laser polariser with an extinction ratio of 10^5 which ensured a very high purity of linear polarisation of the laser beam. The next optical element was a zero-order half wave-plate mounted on a rotatable holder controlled by a stepper motor, used during computer-controlled data acquisition. The rotator was clamped to an optical post on the top flange. The wave-plate could be rotated as desired through 360°. A quarter wave-plate was used when required to produce circularly polarised light for measurement of the ACP $L_\perp$. It was inserted after the half wave-plate. A mirror was temporarily inserted after the Glan-laser polariser. The retro-reflected transmitted beam was minimised so as to ensure the correct orientation of the optic axis of the quarter wave-plate relative to that of the half wave-plate. Instead of rotating the quarter wave-plate, it was maintained at a fixed angle whilst the half-wave

plate was rotated through multiples of 45° to produce left- and right- hand circularly polarised radiation.

3.11 Conclusion

This chapter has presented the apparatus used for the super-elastic scattering elements from laser-excited calcium atoms. The various components of the experimental set-up have been described. These include the atomic beam oven which produced a well-collimated beam of target atoms that interacted with electrons of well-defined momentum and energy from the electron gun. The analyser and channel electron multiplier detected and amplified the number of electrons such that the super-elastic signal was measurable. The laser system described here provided laser radiation at 423.29 nm which was resonant with the 4^1S_0- 4^1P_1 transition in calcium. The optical set-up needed to optimise the laser beam for the experiments was also detailed. A locking system was used to ensure the laser beam remained on resonance at the required frequency to enable data collection over extended periods of time.

The next chapter will discuss the measurement procedures for the super-elastic experiments with calcium. An overview of the preliminary steps needed to optimise the spectrometer performance before measurement are started, will be detailed. The measurement process will be discussed. The results obtained will be presented and compared to predictions from theoretical models.

Chapter 4

Low energy super-elastic scattering from laser-excited calcium atoms

4.1 Introduction

This chapter describes the measurement processes involved in the data acquisition for super-elastic scattering experiments with calcium at low energy. A number of ACPs, as described in Chapter 1, were measured for electron impact excitation of laser-excited calcium atoms by the scattering process. Two sets of experiments were carried out in the low energy regime at nominal equivalent incident energies of 10 eV and 12 eV. These are values assumed to be the energies of the detected electrons for the super-elastic measurements. These energies are nominal only as they did not take into account changes that may have occurred in the contact potential of the electron gun or in any stray fields in the spectrometer during the course of the data collection process. Such changes would introduce an error in the nominal energy and will be discussed in sections of this chapter. To compare with a conventional coincidence experiment, the equivalent energy would be the energy of the incident electron from the interaction region.

P_{lin}, γ and $L_{\perp}$, previously discussed in Chapter 1, were determined. P_{lin} and γ were determined using linearly polarised laser radiation directed at the

interaction region orthogonal to the scattering plane. Measurement of $L_{\perp}$ was undertaken using circularly polarised light obtained by inserting a quarter-wave plate after the half-wave plate as shown in figure 3.10 on page 73.

The experiment could be computer controlled and the programs written to carry out the unmanned process are mentioned briefly here. The different approach to data acquisition at low energy is distinguished from the relatively simpler technique previously employed at higher energies [84]. In the low energy regime, the super-elastic count rates are considerably reduced, so that the experiment had to be run for a longer period of time. Several runs of short time intervals were taken then cumulated to produce the signal count rate. This repetition generated a large set of data files which could no longer be processed manually, but had to be handled using an analysis software. This is also discussed in this chapter.

Finally, the experimental results at 10 eV and 12 eV nominal energies are presented in the last sections. The experimental data are then compared with theoretical models and the results are discussed.

4.2 Preliminary Procedures

4.2.1 Calibration of the electron gun energy

The energy of the incident electron beam was set by the gun bias voltage, V_{GUNE} as described in section 3.4. This voltage controlled the potential at the tungsten filament which dictated the energy of the emitted electrons. However, surfaces of dissimilar metals inside the electron gun gave rise to a contact potential which caused the energy of the emitted electrons to differ from the value set by the external power supply. It was therefore necessary to determine this contact potential prior to measurements in order that it could be taken into account during the experimental runs.

A calibration of the gun was undertaken so that the energy of the emitted electrons could be determined. To accomplish this, the apparent beam energy

had to be compared with a known feature in the cross section. In this case, the calibration was done by performing elastic scattering on helium, which has a characteristic 2^2S negative ion resonance as observed by Brunt, King and Read [104]. This feature occurs at 19.366eV ± 0.005 eV [104], has been measured to high accuracy and is easily reproducible. It therefore provides a good reference for calibration purposes. Furthermore, helium is an inert gas and is compatible with all the targets considered in this project so that the contact potential could be measured when the experiment was operating with the metal vapour target.

This feature in helium results from the capture of an electron by the helium atom to form the He^- ion state, followed by the rapid re-emission of the electron due to the short lifetime of the negative ion. The interference of the re-emitted electron with the electrons directly scattered from helium appears as a characteristic structure in the spectrum as shown in figure 4.1.

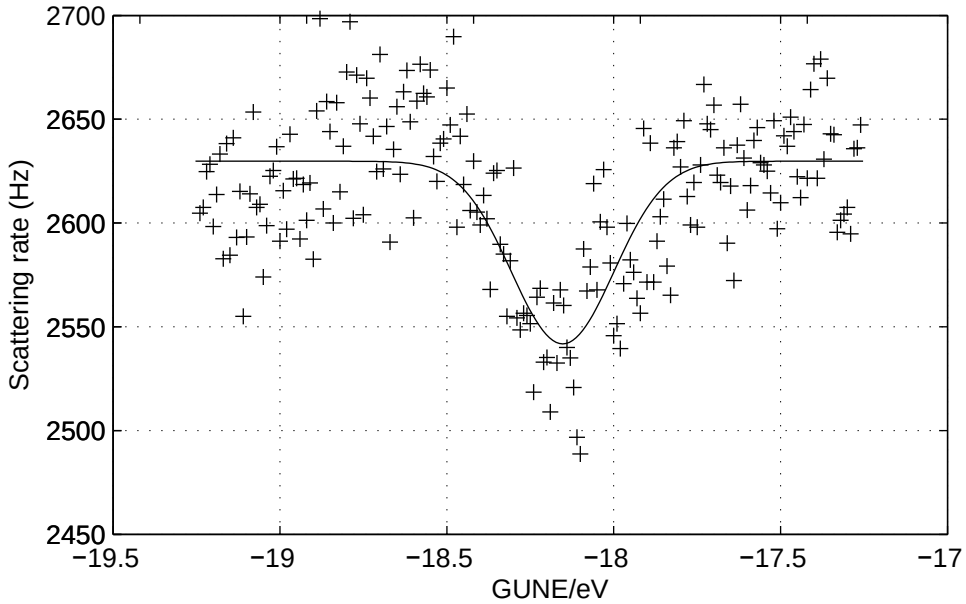

Figure 4.1: *The 2^2S helium resonance feature used to determine the contact potential of the electron gun. The gun and analyser voltages were scanned simultaneously over a range of 2V. The count rate was accumulated for 4s per data point. The graph is a plot of scattering rate as a function of gun voltage. The data has been fitted to a Gaussian curve from which the location of the dip corresponding to the resonance feature was determined to be -18.2 ± 0.1V.*

The following experimental procedure was adopted whenever the gun energy had to be calibrated. A measurement of the count rate of scattered electrons from helium was taken as a function of incident electron energy. This was performed at a scattering angle of 90°. This specific angle was chosen because the characteristic resonance feature that was to be observed is dependent on the scattering angle [104], and is sufficiently prominent at 90° to appear as a dip in the spectrum. The signal to background count ratio is also favourable at this angle and allows graphical analysis of the data to be carried out relatively easily.

Helium gas was injected into the spectrometer via the gas jet nozzle which pointed at the interaction region. As the chamber was evacuated, the flow of helium was adjusted using a needle valve such that an equilibrium pressure was attained. Typical gas pressures of about 10^{-5}mbar were used.

The resonance feature in helium is known to be at ~ 19.366 eV $\pm$ 0.005 eV . In order to determine the contact potential, the electron gun energy was set to 19.37 eV by setting the potential V_{GUNE} to 19.37 eV. Next, the analsyer was set to detect elastically scattered electrons from helium atoms at the interaction region. To do this, the analyser voltage V_{A1RSE} was manually scanned around the gun voltage and adjusted to the maximum observed count rate which effectively corresponded to the elastic peak.

The gun and analyser voltages, V_{GUNE} and V_{A1RSE} were then simultaneously scanned in the same direction and at the same rate. Through this process, elastically scattered electrons of increasing energy were continually being detected by the analyser. By scanning over a sufficiently large range of energies, about 5 eV, the elastic scattering spectrum could be found to include the helium resonance feature. A typical measured spectrum is presented in figure 4.1.

In the example shown in figure 4.1, the He resonance feature can be seen at an apparent gun voltage of -18.2$\pm$0.1 V. This implies an offset between the gun supply voltage, V_{GUNE} and the actual energy with which the electrons are emitted. This corresponds to a contact potential which has a value of -1.2V.

4.2.2 Energy Loss/Gain Spectra

The main preliminary step undertaken prior to any super-elastic experiments was the measurement of energy loss spectra, which determine the scattering cross section as a function of energy loss when the incident electron beam has interacted with the atomic target. Such an interaction may result in several possible processes which then appear in the spectrum. The two principal outcomes are elastic and inelastic scattering. Generally, the elastic scattering process dominates, whereby electrons lose no energy after going through the interaction region. An electron may also be inelastically scattered if it imparts its energy to an atom such that the latter is promoted to a higher energy state. In this case the electron leaves the interaction region with lower energy than the incoming electron beam. In the presence of a laser field that is resonant with an atomic transition, with which the atom is irradiated prior to collision with the electron, the electron may also gain energy from the interaction as the excited atom relaxes to ground or a lower state. In this case, the electron that leaves the interaction has more energy than the incident electron beam and so is super-elastically scattered. The elastic peak can be observed as a relatively large peak compared to the inelastic and super-elastic peaks in the scattering cross-section. An example of such a spectrum is shown in figure 4.2.

4.2.3 Measurement Process

There are two ways of obtaining an energy loss spectrum. The first involves keeping the gun voltage constant and then ramping the analyser energy. The resulting spectrum shows the yield of scattered electrons as a function of residual energy for a fixed incident electron beam energy. The alternative method is to keep the analyser potential fixed whilst the gun supply voltage is ramped. The subsequent spectrum displays the scattering intensity against incident electron energy at a fixed residual energy. In both cases, the elastic scattering feature which appears where the incident electron energy and the residual energy are equal, divides the spectrum between super-elastic and inelastic regions as is observed in figure 4.2.

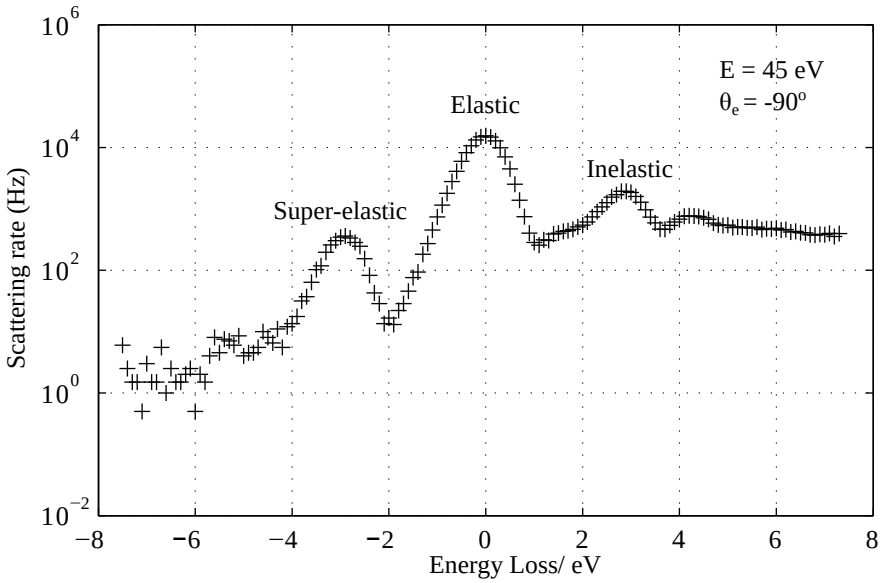

Figure 4.2: *Energy loss spectrum measured for laser-excited calcium atoms plotted on a logarithmic scale, with incident electron beam energy of 45 eV at a scattering angle of -90°. The elastic peak is the most prominent with the highest count rate. The inelastic peak is seen at positive energy loss, indicating the detected electrons have lower energy than the incident electron beam. The super-elastically scattered electrons are on the negative energy loss side having gained energy from the collision process.*

4.3 Experimental Technique

Super-elastic scattering measurements from calcium were carried out at an equivalent nominal energy of 10 eV and 12 eV. The equivalent energies correspond to the energies of the incident electron beam in a conventional coincidence experiment. In this case, these are the assumed energies of the detected super-elastically scattered electrons. The analyser was set to detect electrons of energy 10 eV and 12 eV for the two different sets of experiments. The electron gun was then set to produce electrons at (10-E) eV and (12-E) eV respectively, where E=2.93 eV, corresponds to the energy of the transition from the ground state to the 4^1P_1 state in calcium. The gun was therefore set to 7.07 eV and 9.07 eV respectively.

Previous super-elastic experiments performed from calcium used a computer program called `SuperStep` for data acquisition [84]. However, in the new experiments at low energy, a new computer program called `multiscan` was developed by Alex Knight-Percival at Manchester to record the scattering data [84]. The principal reason for the development of this program was the underlying method of data collection for experiments at low energies (below 17 eV), which differed from the technique used at higher energies. This was required since the count rates are generally higher at higher energies and the data collection time is subsequently small.

In the experiments for a specific scattering angle for high energy data collection, the signal S was taken then the background, B was measured and the difference between the two produced the super-elastic signal, I= S-B. Typically the duration of this process was small such that it could be reasonably assumed that the background count rate remained constant over the period of the measurements. This assumption was valid over the relatively small acquisition times involved at higher energies.

By contrast, at the lower energies investigated in this project, the count rates were considerably reduced and the background signal from different scattering mechanisms was much higher. For this reason, data had to be collected over extended periods of time. At some scattering angles, the super-elastic sig-

nal was so low that acquisition times had to be increased to about 5 minutes per polarisation angle in order to extract super-elastic signal from the collected data. In this case, it was observed that the background count rate would drift over the duration of data acquisition. As a result, the data collection method was modified to allow for this change in background count rates.

Despite the methodology being intrinsically similar, the technique was different for the experiments carried out at low energies. At a given scattering angle, multiple scans were taken which lasted up to 30 seconds each. The total number of scans n, constituted a *set* of scans at that specific scattering angle. A background sweep was taken immediately after each signal sweep by blocking the laser light using a laser shutter. Over this time period, the assumption could be reliably made that the background count rate remained unchanged. The `multiscan` program was developed to assist in this measuring process [84].

As the data collection time was significantly reduced, the quality of the calculated data, obtained by subtracting the background rate from the super-elastic signal, was subsequently poor. The deduced signal from n sets were then combined and the actual signal was determined for a particular scattering angle.

4.4 Method of Data Acquisition

The super-elastic signal for calcium was measured as a function of the polarisation of the laser beam over a range of scattering angles. The `SuperStep` Labview program, developed by Alex Knight-Percival at Manchester, was used in the first instance for this purpose but was then superceded by the newer Labview program `multiscan` [84]. As noted above, the `SuperStep` program controlled the stepper motor which was connected to the half wave-plate and could therefore be used to control the laser polarisation. The program was also able to record count rates from the electron analyser whilst rotating the wave plate. In this way the wave plate could be configured by the user to rotate at regular angular intervals, pause at every specified angle for a predefined time and collect data at that particular angle. Thus, as the polarisation vector was

altered, the super-elastic signal could be collected and eventually used to determine the ACPs.

In the experiments carried out at Manchester, the ACPs were determined directly from the experimental runs. These ACPs can be related to the coincidence experiment via optical pumping parameters as discussed in Chapter 2. For calcium, as mentioned, these optical pumping parameters are equal to unity and therefore the results obtained in the super-elastic measurements relate directly to those from the conventional coincidence technique.

4.4.1 Measuring P_{lin} and γ

Linearly polarised light was used to excite the calcium atoms in order to determine the alignment parameters P_{lin} and γ. The half-wave plate was rotated using a computer-controlled stepper motor. As the half-wave plate rotated through θ_{pol}, the polarisation vector was in turn rotated through $2\theta_{pol}$.

The initial method of taking experimental data is detailed below. With the analyser set to a given scattering angle, the half-wave plate was rotated through 360° around the scattering plane in steps of 10°, corresponding to individual polarisation angles. For each polarisation angle, the signal was collected for 20 seconds or more, depending on the intensity of the super-elastic signal. The wave-plate was then rotated in the opposite direction and the count rate measurement repeated in the same manner. This reverse procedure repositioned the wave-plate to its exact starting point, and eliminated any systematic error in the calibration of the stepper motor which was being used to control the rotation of the wave-plate. An average count rate was then calculated for every polarisation angle. The laser beam was then blocked using the laser shutter and the number of counts was taken over a specified time. The background count rate was then subtracted from the averaged raw signal data to give the actual signal. The analyser was then moved to the next scattering angle (in intervals of 5°) and the above steps repeated.

4.4.2 Measurement of $L_{\perp}$

For the determination of the ACP $L_{\perp}$, a quarter-wave plate was inserted as described in section 3.10 . With the quarter-wave plate fixed in position, the half-wave plate was rotated from 0° in 45° angular intervals so as to produce circularly polarised radiation, through one full rotation thus covering the following angles: 0°, 45°, 90°, 135°, 180°, 225°, 270°, and 315°. This produced circularly polarised light with alternating handedness (i.e. right- and left-hand circular). The half-wave plate was reversed through one full rotation to bring it back to its precise starting position before a new set of data was taken.

4.5 Derivation of the ACPs

The ACPs P_{lin} and γ could be determined from the data acquired using linearly polarised light. In the previous section 4.4, this experimental process has been described whereby the scattering count rate was measured as a function of scattering angle. The count rates changed as the polarisation vector was altered. The background count rates were subtracted from the raw signal count rates to obtain the actual super-elastic signal rate.

A plot of signal count rate as a function of polarisation angle could then be obtained. By fitting the data to an offset sinusoidal curve of the form in equation 4.1, values of the ACPs P_{lin} and γ could be obtained as they relate to the parameters in the equation [42, 56].

$$S\left(\theta_{\mathrm{pol}}\right) = A\ \left(\theta_{\mathrm{e}}\right) + B\ \left(\theta_{\mathrm{e}}\right) cos^{2}\left(\theta_{\mathrm{pol}} - C(\theta_{\mathrm{e}})\right) \tag{4.1}$$

P_{lin} is calculated from parameters A and B obtained from the fit using equation 4.1.

$$P_{\mathrm{lin}}\ \left(\theta_{\mathrm{e}}\right) = \frac{B(\theta_{\mathrm{e}})}{2A(\theta_{\mathrm{e}}) + B(\theta_{\mathrm{e}})} \tag{4.2}$$

The uncertainty in P_{lin} can be determined in the following way.

$$\sigma\left(P_{lin}\right)=\sqrt{\left(\frac{-2B}{(2A+B)^2}\right)^2(\sigma A)^2+\left(\frac{2A}{(2A+B)^2}\right)^2(\sigma B)^2} \tag{4.3}$$

It is less straightforward to obtain a value for the ACP γ in the natural frame. To determine γ, geometrical considerations of the coincidence experiment and the super-elastic process have to be considered. Since the super-elastic experiment can be regarded as the time-inverse equivalent of the coincidence technique, it is possible to compare the results obtained using the super-elastic set-up with those of the conventional process. In the conventional coincidence experiment, the x-axis of the natural frame lies along the electron gun axis as shown in figure 4.3, and scattering angles are measured with respect to this axis. In this case, the natural frame is fixed as the analyser rotates around the scattering plane.

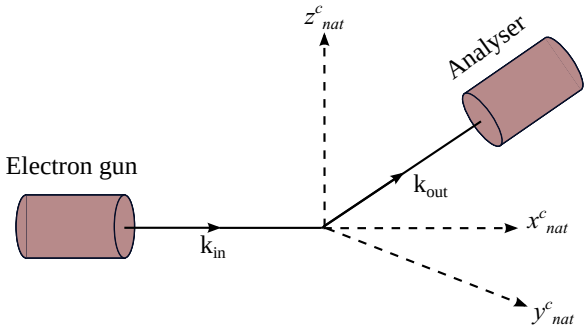

Figure 4.3: *The natural frame $(x^c_{nat}, y^c_{nat}, z^c_{nat})$ in the electron-photon coincidence experiment.*

To compare the results of the two different methods in the natural frame, a geometrical treatment is required. The gun and analyser positions have to be swapped in the super-elastic experiment to match the geometry of the coincidence experiment. However, when the analyser is rotated around the interaction region in the super-elastic spectrometer, this corresponds to moving the electron gun around the scattering plane in a conventional coincidence experiment. This implies a corresponding rotation of the natural frame. This is shown in

figure 4.4. Subsequently the x-axis of the natural frame is no longer static, but moves around the interaction region as the analyser is rotated.

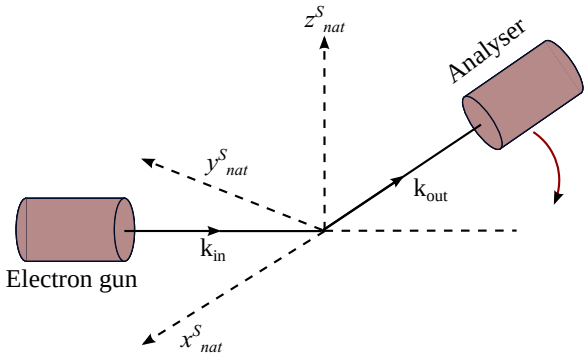

Figure 4.4: *The natural frame $(x^s_{nat}, y^s_{nat}, z^s_{nat})$ in the super-elastic experiment.*

The ACP γ was determined from the parameter C obtained by fitting the experimental data to equation 4.1. Parameter C corresponds to the angle of the polarisation vector for which the super-elastic count rate is maximum. Experimentally this was measured with respect to the gun axis and not the analyser axis. Hence in order to determine γ, a rotation is needed where C can be referenced to the x-axis of the natural frame as defined by the analyser. This is illustrated in figure 4.5.

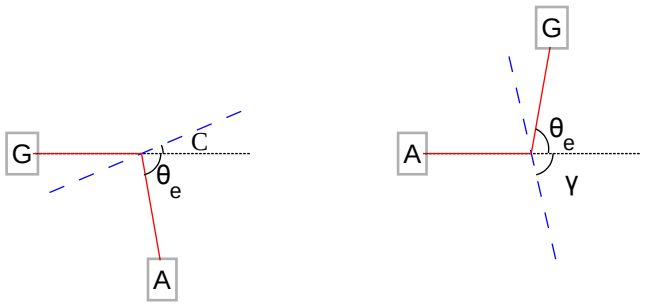

(a) Experimental configuration (b) Rotated configuration

Figure 4.5: *This diagram demonstrates the geometrical treatment needed to obtain the parameter γ from the experimentally determined parameter C in the natural frame. Shown in (a) is the geometry of the super-elastic experiment, showing the relative positions of the gun and analyser as they are in the spectrometer. In (b) the rotated configuration is illustrated which matches the locations of the gun and analyser in the conventional coincidence experiment. The black dashed line corresponds to the x-axis in the natural frame. The solid red line is the trajectory of super-elastically scattered electrons from the interaction region. The blue dashed line marks the direction of maximum scattering intensity.*

The sign of γ is determined by convention which states that θ_e should be positive after rotation. If this is not the case, the rotation configuration is flipped as illustrated in figure 4.6.

The error in γ can be calculated using equation 4.4 as follows:

$$\sigma_\gamma = \sqrt{\sigma_{\theta_e}^2 + \sigma_C^2} \tag{4.4}$$

The parameter $L_\perp$ can be obtained by measuring the super-elastic scattering count rate when the laser radiation exciting the atomic target is circularly polarised light. In the case of calcium, as a result of the optical pumping parameter being equal to unity, the following direct relationship holds.

$$L_\perp = P_3^S \tag{4.5}$$

The experimental configuration for measuring this ACP has been discussed in section 3.10. $P_3{}^S$ was determined from measurements of the scattering yields

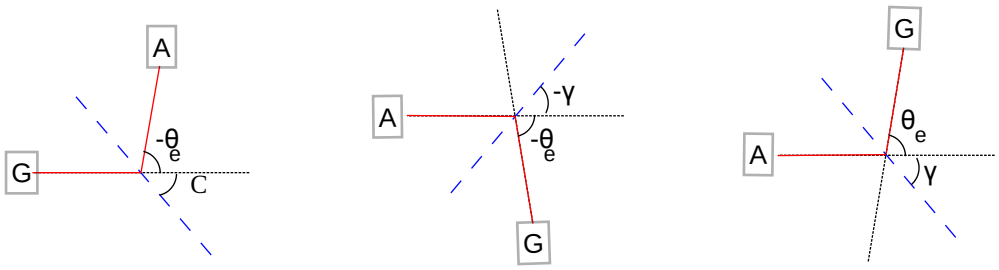

(a) Experimental configuration (b) Rotated configuration (c) Flipped rotation

Figure 4.6: *This diagram illustrates a similar rotation as in 4.5 however θ_e is negative after rotation. Using symmetry arguments, the rotation can be flipped to to produce the configuration shown in (c). This determines the sign of γ.*

with alternating left-hand and right-hand circularly polarised light.

$$L_\perp = P_3^S = \frac{S_{RHC} - S_{LHC}}{S_{RHC} + S_{LHC}} \tag{4.6}$$

The error in $L_\perp$ can be found by normal propagation method as shown below.

$${\sigma_{L_\perp}}^2 = \frac{1}{(S_{RHC} + S_{LHC})^2}\left(\sigma_{RHC}^2 + \sigma_{LHC}^2\right) + \left(\frac{S_{RHC} - S_{LHC}}{S_{RHC} + S_{LHC}}\right)^2 \left(\sigma_{RHC}^2 + \sigma_{LHC}^2\right) \tag{4.7}$$

where σ_{RHC} and σ_{LHC} are the uncertainties associated with the count rates from right-hand and left-hand circularly polarised light respectively.

4.5.1 Results at 12 eV and 10 eV nominal energy

Figure 4.7 shows the experimental results with the 12 eV data on the left and 10 eV on the right.

The top four graphs, a-d, present the plots of P_{lin} and γ as a function of scattering angle for nominal energies of 12 eV and 10 eV respectively. It can be seen that P_{lin} has similar structures at both energies with prominent features appearing at the two energies. The nominal energy quoted here is the assumed energy of the electrons detected by the analyser for the super-elastically scattered electrons. Owing to changes in the contact potential discussed in section

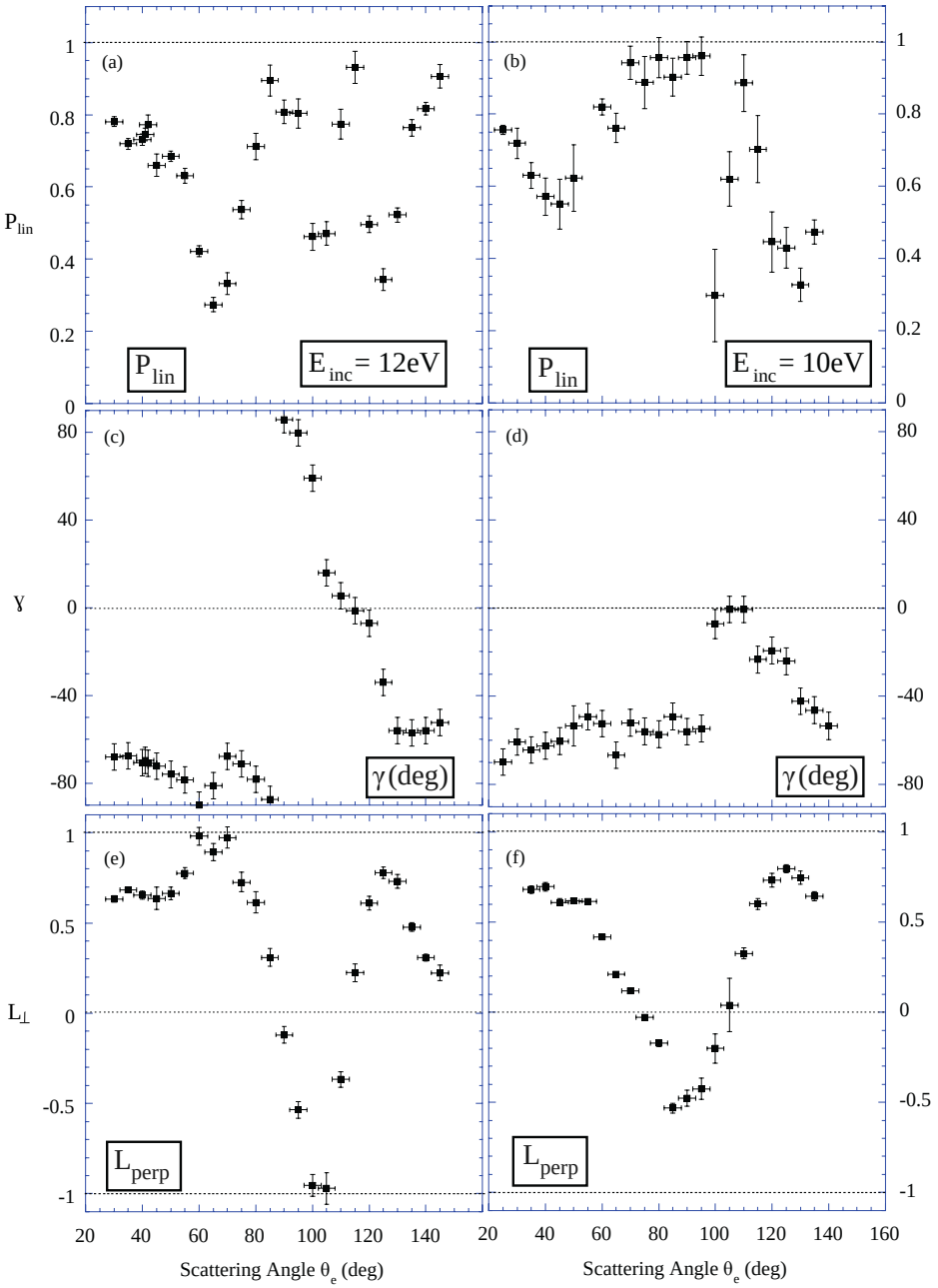

Figure 4.7: *Graph showing the ACP measurements at 10 eV and 12 eV nominal energy.*

4.2.1, this nominal energy may have a certain error associated with it and this will be further discussed in later sections.

Three minima can be observed on the graph of P_{lin} at 12 eV at scattering

angles of 60°, 100°, 125°. At these angles, P_{lin} has a corresponding value of 0.27, 0.46 and 0.35 respectively. The deepest minimum occurs at the smallest scattering angle. For the rest of the scattering angle range, P_{lin} is seen to vary continuously and approaches unity at an angle of 115° where it has a value of +0.93.

The structure of P_{lin} at 10 eV shows two distinct minima occurring at 60°, as was the case with the 12 eV data, and 125°. At this energy, the minimum at 60° is less deep going down to 0.55 only as compared to the dip in P_{lin} at 12 eV at the same angle. There is evidence of a third minimum at 80° which could be likened to the minimum observed at 100° with the 12 eV data. However the statistics are poor and cannot be relied upon to predict a feature with certainty. It is worth noting that the data used to calculate P_{lin} at 100° has been produced from a set of 14 runs which were the useful ones from over 200 attempted runs due to the low count rates at this scattering angle. This helps to explain the relatively poor quality and large uncertainty associated with this data point.

Graphs c and d in the middle show plots of the alignment angle γ as a function of scattering angle, with the 12 eV data again on the left. At smaller scattering angles, $30° < \theta_e < 70°$, there is little variation in γ at 12 eV. At these angles, it remains around -80, dipping only slightly at $\theta_e = 60°$, where the charge cloud is aligned perpendicular to the electron beam direction. Thereafter, the variation of γ with scattering angle becomes larger. After the minimum, the charge cloud changes direction again at $\theta_e = 70°$. γ decreases again and crosses through zero at $\theta_e \approx 115°$. The graph then shows a plateau at $130° \leq \theta_e \leq 145°$ in which range γ remains relatively unchanged at around -55°.

For the 10 eV data, the variation of γ for smaller scattering angles remains relatively constant. Over the relatively large angular range $25° \leq \theta_e \leq 95°$, little variation can be seen as γ changes from -70° at the lower scattering angle to -55° at 95°. Over the whole scattering angle range γ remains negative, however it rises rapidly to $\sim 0°$ at $\theta_e \sim 110°$. Thereafter, as was observed with the 12 eV data, γ decreases as θ_e increases.

Plots e and f show the variation of $L_\perp$ with scattering angle. The graphs at both energies have simpler forms than for P_{lin} and γ at the corresponding energies. They are similar with one salient feature in the form of a single sharp dip. This minimum occurs at $\theta_e \approx 100^o$ at 12 eV. At this energy, the value of $L_\perp$ extends over the full range of allowed values -1 to +1. In contrast, $L_\perp$ lies in the range -0.53 $<\perp<$ +0.80 for a nominal energy of 10 eV. At 10 eV, the minimum is seen to occur at an angle of $\theta_e \approx 85^o$. In both cases, a peak occurs at $\theta_e \approx 125^o$. A second peak can be seen at 12 eV whereas no other peak can be confirmed for the data at 10 eV.

4.5.2 Comparison between theory and data at 10 eV nominal energy

This section presents a comparison of the 10 eV nominal energy data with theoretical results produced by four different models. These calculations have been taken from publications which provide the Stokes parameters. The ACPs have here been derived from those data using the relationship in equation 4.8 to 4.9 [4] in order to allow direct comparison with the experimental data.

$$P_1 + iP_2 = P_{\text{lin}} e^{2i\gamma} \tag{4.8}$$

from which,

$$P_{\text{lin}} = \sqrt{{P_1}^2 + {P_2}^2} \tag{4.9}$$

$$\gamma = \frac{1}{2} arctan\left(\frac{P_2}{P_1}\right) \tag{4.10}$$

The four models under consideration are the Relativistic Distorted Wave (RDW) calculation [105], the R-matrix (RM) calculation [106], the R-matrix using B-splines (BSR) calculation [107] and the Convergent Close-Coupling (CCC) method [108].

Figure 4.8 shows a comparison of the data with the above theoretical models. It can be clearly seen from the graphs that there is only poor agreement between experiment and theory. Each model predicts different positions and magnitudes for both peaks and dips, as will be discussed below.

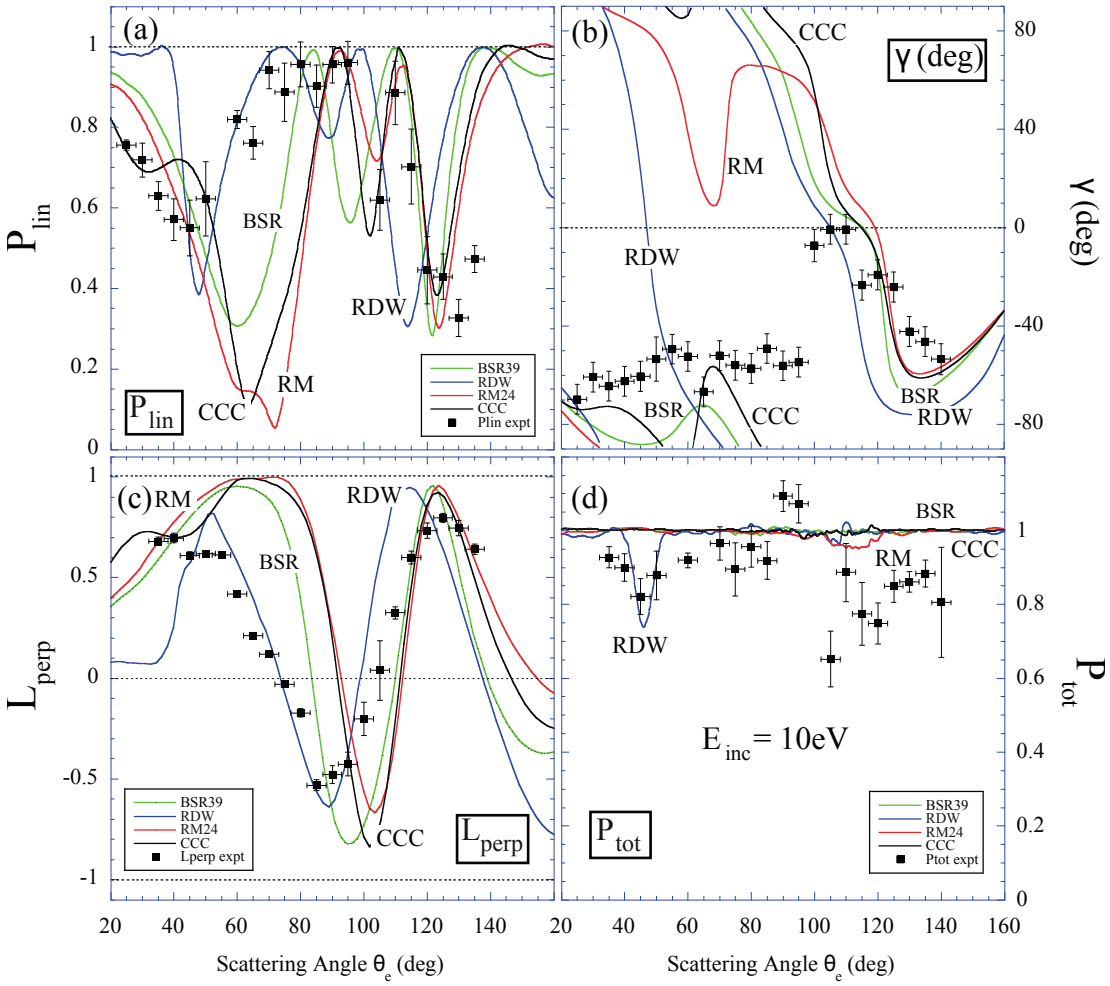

Figure 4.8: *Graph showing the measurements at 10 eV nominal energy compared with theoretical calculations at 10 eV.*

The first graph, (a) is a plot of P_{lin} together with the four models. The dip at θ_e=125° is predicted by all models with evidence of an additional feature at $\theta_e \approx 100°$. However, all models seem to show poor agreement with experiment at smaller scattering angles. The feature at around θ_e=50° is predicted by the RDW model, but there is little agreement between the same model and measured data at smaller scattering angles. Both the R-matrix and the CCC

models predict a sharp dip at $\theta_e \approx 80^o$ but this feature is not seen in the experimental data.

Similarly, the models agree poorly with the measured ACP γ as shown in 4.8(b). The graph can be split in two sections, where $\theta_e < 100^o$ and $\theta_e > 100^o$. For the smaller scattering angles, the experimental data is mostly constant whereas the models all predict some structure. At higher angles, the models predict a trough in the region 130°-140° which can be related to the small dip observed in the data, indicating some weak agreement in this angular range.

The graph for $L_\perp$ shows relatively better agreement in the overall structure between theory and experiment. All models predict a single large minimum which is obvious in the experimental data albeit at a smaller scattering angle than that predicted by the theoretical calculations. Additionally, the width of the feature is predicted to be smaller, whereas it appears as a relatively wider trough in the experimental data.

The final graph shows the calculated quantity P_{tot} which is a fourth ACP, being compared to the values calculated from theoretical predictions. P_{tot} is calculated using equation 4.11.

$$P_{\text{tot}} = \sqrt{P_{lin}^2 + {L_\perp}^2} \tag{4.11}$$

P_{tot} is a measure of the coherence of the scattering process. It is equal to unity for a fully coherent interaction. In this case, loss of coherence is observed especially at $\sim 40^o$, correctly predicted by the RDW model but the loss of coherence in the experimental data at $\theta_e \sim 100^o$ is not predicted by any of the models.

4.5.3 Comparison between data at 12 eV nominal energy and 10 eV data

As discussed in section 4.2.1, the contact potential was subject to variations as the experiment proceeded over extended periods of time. This is believed to have been caused by a gradual deposition of calcium on the internal surfaces of

the vacuum chamber. These layers then charged up, giving rise to stray electric fields which could affect the energy of the incident electron beam, an effect which has been previously reported. This caused an estimated uncertainty of $\sim$ 2eV in the calibrated incident electron beam. For this reason and additionally, as a result of the poor agreement between experimental data at 10 eV nominal energy and the calculations provided by the models at 10 eV, the experimental results at 12 eV were compared against the predictions of the models at 10 eV.

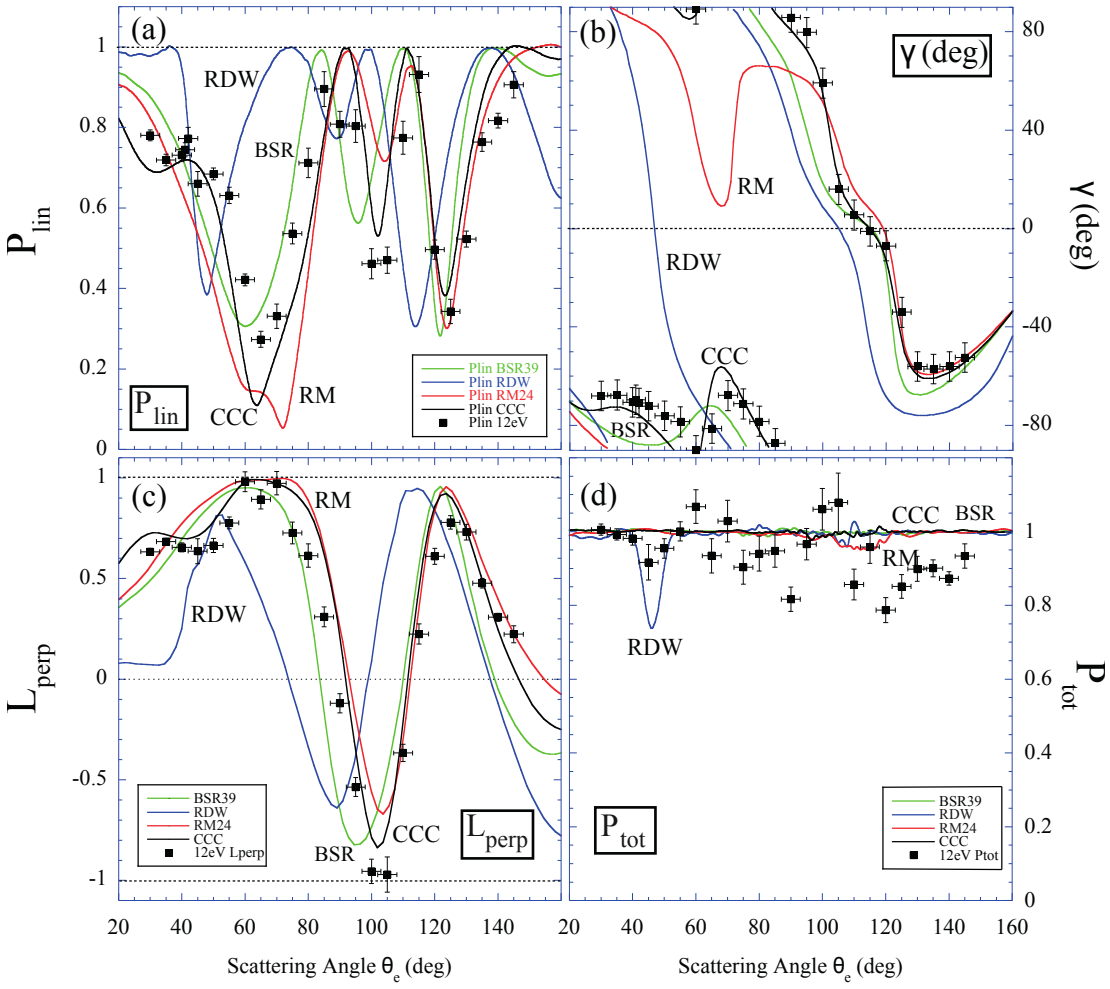

Figure 4.9: *Graph showing the measurements at 12 eV nominal energy compared with theoretical calculations at 10 eV.*

Figure 4.9 presents the comparison of data measured at 12 eV nominal energy with the theoretical calculations at 10 eV. An immediate observation is that there is better overall agreement between the data at 12 eV nominal en-

ergy and the 10 eV theoretical predictions. The RDW model still does not agree with experiment but the BSR and CCC models now far more accurately predict the data.

In the case of parameter P_{lin}, the RDW model predicts three troughs which do not corroborate with the data. The other three models give better predictions, although the RM model shows an additional feature in the deepest dip which is not apparent in the data. The BSR model correctly calculates the magnitude of the two largest minima whereas the CCC shows better angular agreement with the features found in the experimental data.

Graph b is a plot of γ against theory. Once again, the BSR model obtains more accurate magnitudes rather than positions of the features which are better reproduced by the CCC calculation. Indeed, the CCC model agrees well with the results for γ particularly for angles $\theta_e > 70^o$. For $\theta_e < 70^o$, an angular offset can be observed despite the structure being correct. The RM model shows some agreement at higher scattering angles especially for $\theta_e \leq 100^o$. At smaller angles, this model does not match the data predicting a feature which does not appear. The RDW model shows features that are not reproduced in the data, and therefore fails to predict the experimental results.

For $L_\perp$, the RDW model again shows no agreement with the experimental results. The CCC, BSR and RM models all reproduce the same structure as the experimental curve, particularly the width of the minimum. The CCC shows very accurate agreement with the data, correctly predicting the maximum value for $L_\perp$ as well as the remaining features. The width of the large dip also matches well with the CCC model.

Comparison of P_{tot} shows that none of the models predict the loss of coherence in the interaction that appears as the scattering angle increases. The RDW predicts a relatively large loss of coherence at $\theta_e \sim 40^o$ which occurs only as a much smaller feature in the data.

The satisfactory agreement between most theoretical models at 10 eV and

the experimental data at 12 eV confirms the postulate that an offset of ∼2 eV in the incident energy does occur. This implies that the nominal energy of 12 eV was in fact equivalent or closer to 10 eV. Overall, the CCC model gives the closest overall prediction of the data. CCC calculations at 8 eV were hence requested from Professor Igor Bray [109]. The new calculation was then compared to the experimental results obtained at 10 eV nominal energy as presented in figure 4.10. It can be seen that there is now good overall agreement , further confirming the 2 eV offset in energy of the nominal values as discussed. It can be seen that the CCC model correctly predicts all features in the measured ACPs.

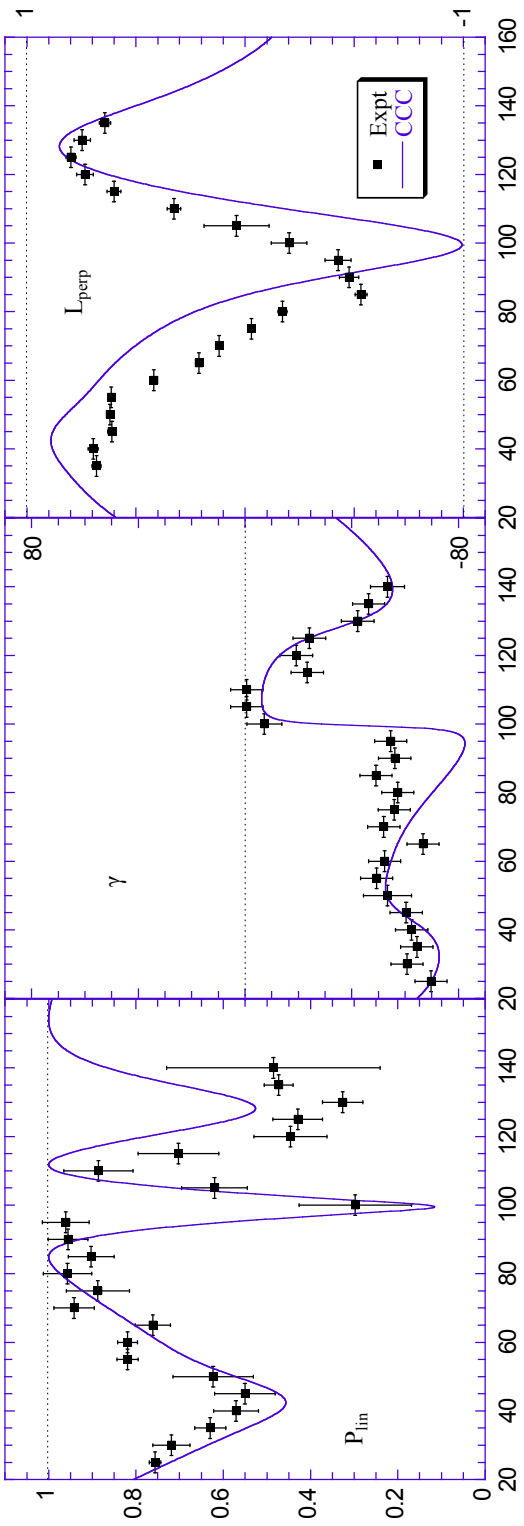

Figure 4.10: *Graph showing the measurements at 10 eV nominal energy compared with theoretical calculations using the CCC model at 8 eV.*

In the case of P_{lin}, the three minima occurring in the experimental data are all reasonably well predicted by the model. The deepest trough, formed primarily by one single data point is confirmed in magnitude at the same angular position. The dip at the larger scattering angle, at $\theta_e \simeq 90^o$, is however underestimated in theory by about 50%.

The calculated trend for γ appears to agree extremely well with the measured curve. An additional feature in the form of a dip at $\theta_e \approx 95^o$ is not observed in the experimental results, but all other features predicted by the model are apparent.

The graph for $L_\perp$ shows the same structure in the experimental data as in the theoretical calculation however there is an obvious angular shift whereby the model overstates the positions of most features. The occurrence of the large single dip is confirmed by theory but the magnitude is not correctly reproduced. The CCC model predicts a dip to $L_\perp \simeq -1$, whereas a fall to $L_\perp = -0.55$ is observed experimentally. The maximum value at lower scattering angle, $\theta_e \simeq 40^o$ is overestimated by the calculations, but the peak value at $\theta_e \simeq 130^o$ is reproduced. The angular positions of the two maxima on either side of the dip, as predicted by the model, match relatively well with the experimental results.

Overall, the CCC model calculations at 8 eV shows very good agreement with the results at nominal energy of 10 eV. This, coupled with the good comparison seen between the same model at 10 eV and the results at 12 eV nominal energy, provides evidence of the 2 eV offset in energy of the incident electron beam.

4.5.4 Conclusion

This chapter has elaborated the technical methods of data acquisition for the super-elastic scattering measurements from calcium atoms at low energies. The preliminary procedures undertaken to prepare the spectrometer for measurements, including the calibration processes have been outlined. The experimental approach to data acquisition using existing computer programs has

been described.

The results for super-elastic scattering of electrons from laser-excited calcium atoms at 10 eV and 12 eV nominal outgoing energies have been presented and discussed. Furthermore, these have been compared to theoretical calculations from four different models namely RM, RDW, BSR and CCC models. Poor agreement was found between the 10 eV nominal energy data and calculations at the same energy. It was found that there was an uncertainty of about 2 eV in the values of the calibrated energy of the spectrometer. Hence, the experimental results at 12 eV nominal energy were compared to the theoretical predictions at 10 eV. Good agreement was observed indicating there was an offset of 2 eV between the actual and measured values for the incident electron energy. In this case, the BSR and CCC calculations were found to better match the experimental results.

Taking into account the 2 eV discrepancy in the incident electron beam energy, the data at 10 eV was then compared to CCC calculation at 8 eV. The agreement between experiment and the model was found to be excellent, confirming that there was indeed a 2 eV offset in energy between the nominal energy values quoted for the measurements and the actual energy of the electrons.

Chapter 5

Design and Characterisation of a New High Temperature Atomic Beam Oven

5.1 Introduction

A major part of this project involved the design and construction of a new oven that could reach high temperatures (1200°C-1500°C) in order to investigate the heavier targets of interest. The existing oven [94] used for the experiments carried out with calcium could not be used for the new targets (silver, gold and copper) which need significantly higher temperatures for vaporisation. A new high temperature atomic beam oven has therefore been designed and built to deliver well collimated beams of these targets.

The following sections detail the research required to realise this oven. The challenges facing the design of the oven are considerable since it not only had to operate at high temperatures but also had to be inert and non-magnetic. Additionally the oven had to be compatible with all targets of interest and this imposed further restrictions mostly on the range of materials that could be used for the construction of various parts of the oven. The solutions to these problems will be discussed in this chapter. The design will be reviewed in light of the mentioned criteria and the tests carried out on the prototype before the final design was agreed on will be presented.

5.2 Design and Characteristics of the Oven

The new high temperature effusive atomic beam source was required to perform super-elastic experiments from silver, copper and gold. The temperatures required to produce a vapour pressure of 10^2 mm Hg are shown in table 5.1 [46]. For comparison, the corresponding temperatures for calcium have also been provided. From the table, the quoted temperature required for calcium to reach a vapour pressure of 10^{-2} mm Hg is 600°C. In practice however a higher crucible temperature of about 800°C is required to produce an atomic beam of sufficient density in order to collect data. Hence it was predicted that the data in the table should act as a guide and the temperatures required would almost certainly be higher.

Element(°C)	Melting Point(°C)	Boiling Point(°C)	Temperature for v.p of 10^{-2} mm Hg(°C)
Cu	1083	2580	1250
Au	1063	2660	1420
Ag	962	2212	1030
Ca	850	1440	600

Table 5.1: *Table comparing temperatures required to melt, boil and vaporise the targets of interest.*

The guiding principles behind the design of this new oven drew on those for the oven used to vaporise calcium (as discussed in chapter 3). The new oven was required to heat the relevant element in a crucible inside a surrounding furnace. The furnace was to be heated directly or indirectly and convey the heat to the crucible by thermal conduction. An aperture was required to allow evaporated material contained in the crucible to be discharged in a fine, high density beam which would ideally be well collimated in order to minimise its transverse Doppler profile. A well defined beam would also ensure minimum undesirable deposition of target atoms onto other surfaces inside the vacuum chamber, which could otherwise react with or damage sensitive experimental components.

The main aspects involved in the design of the new oven were its geometry and the materials used for its construction; these features had to be tailor-made

to meet the specific requirements of the experiment as well as the existing chambers into which the oven should fit.

The principal factors governing the choice of materials used in the new oven and its supporting parts were:

i. The ability to withstand high temperatures and multiple heating cycles

ii. Mechanical strength and durability

iii. The ability to be easily machined

iv. Cost-effectiveness

Additionally, all materials used in the construction of the new oven had to be non-magnetic. The consideration of certain specific materials has dictated the design of the new oven as detailed in this chapter. Since the oven was expected to operate at temperatures in excess of 1000°C, materials with low outgassing rates at such elevated temperatures had to be chosen. One of the main challenges of a high temperature oven is achieving the actual temperature in a stable, controlled manner whilst ensuring the substances that have been used in the construction of the oven do not react with each other or with the sample material. In their paper 'High Temperature Metal Atom Beam Sources', Ross and Sonntag summarised the suitability of different materials to be used for crucible fabrication for a range of elements [46]. The relevant crucible materials that can be used for this project are tabulated in Table 5.2.

Element	Crucible Material
Cu	C, Al_2O_3,W,Ta,Mo
Ag	C,Mo,Ta
Au	C,Mo

Table 5.2: *Compatibility of various crucible materials with the elements of interest.*

The fact that the oven was to be compatible with all three abovementioned elements implied that carbon and molybdenum were the two options most appropriate as crucible material. Indeed, graphite was deemed to be a sensible

choice as crucible material, boron nitride was found to be suitable for the furnace, and refractive metals including tantalum, molybdenum and tungsten were used for any other parts of the oven as will be discussed in following sections.

5.3 Methods of heating

Several methods have been successfully employed for the generation of heat to produce atomic beams. These include electron bombardment, inductive heating and resistive heating [46]. Electron bombardment techniques were ruled out for the purpose of this project due to the concerns of maintaining a near-zero magnetic field in the scattering chamber and also due to the generation of electrons in the chamber. A number of sources briefly describe the achievement of desired high temperatures by means of inductive heating but the lack of detailed specifications and the limited experience with these types of oven within the group at Manchester implied that this choice was not considered. On the other hand, since the group has had success with resistively heated sources, it was decided to adopt resistive heating approach instead.

Resistive heaters employ a number of heating techniques. Use has been made of resistively heated cylinders, made up of graphite or tantalum, which then heat up an internal crucible. This method has been employed in the vaporisation of chromium [110]. In experiments where magnetic field reduction or elimination is critical, a pair of concentric such cylinders have been utilised to attain the required temperatures [111]. The arrangement ensures a negligible residual magnetic field. However, this design requires high currents for adequate power production [46]. Indeed, Ross and Sonntag report achieving 1500^{o}C with a power of about 2 KW at a current of 100A. However, the intention was that the power supplies would ideally be inexpensive, in-house built and therefore non labour-intensive. Thus, it was essential to keep the requirements easily achievable.

The other option was to heat the crucible using a wire configuration similar to the one employed for the calcium oven which uses a coil of Thermocoax wire wound in a spiral fashion along grooves in the heater jacket that houses the

oven crucible [94]. However, as noted by Ross and Sonntag, the need to reach temperatures above 1000^{o}C complicates matters; Thermocoax, for example, can only be used to attain temperatures lower than 1000^{o}C. Above this temperature, pure metal wires of either molybdenum, tantalum or tungsten have to be used. Carbon, known to withstand heating to high temperatures was also considered as a potential heating element. At an initial stage, carbon rods and fine-stranded carbon fibre were tested. It was observed that the resistance of the carbon element dropped with increasing temperature so that the power required to reach the desired temperature was high. This option was therefore abandoned for lack of efficiency, in favour of metal wires. At this point, it was therefore necessary to establish which of the three above mentioned metals would be best suited for the purpose.

5.3.1 Wire-winding style

Before tests were carried out for the selection of heating wire, it was essential to determine the wire-winding style that would be adopted. The principal and decisive criterion here rested on the fact that the resulting magnetic field produced by the current in the wires had to be negligible. Tests were performed using copper wire wound around various types of ceramic rods, and the relationship of the magnetic field as a measure of the current in the wires was noted. Copper wire was used as it is relatively cheap and easily available and the relative rather than absolute magnetic field effect was being measured. The styles investigated include a single spiral of wire wound around a single bore ceramic rod (A); double parallel running spirals along a single bore ceramic rod (B); a four-bore ceramic rod with a wire running up and down each hole (C). By choosing different methods it was then possible to establish which design would produce the minimum field. Style B or C which have currents running in opposite directions in different halves of the wire were expected to cancel the effects of magnetic field (by the logic of equal and opposite currents producing self-offsetting magnetic fields). For each winding style, a current of up to 8 A was passed through the wire, in increments of 1 A, and the magnetic field generated from the wires was measured at a distance of 63 mm from one end of the ceramic rod, thus reproducing the approximate distance of the interac-

tion region from the oven in the super-elastic experiment. The results from the study are shown in figure 5.1. The non-inductive style of closely wound double

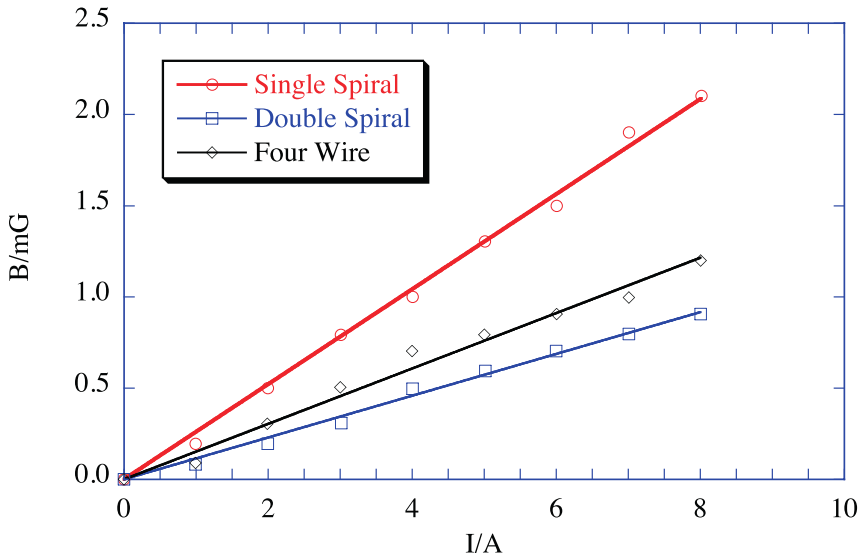

Figure 5.1: *Graph showing the measurement of magnetic field generated by various winding styles. The current passing through the wires is plotted on the x-axis and the resulting magnetic field for each configuration is shown on the y-axis. The uncertainties were smaller compared to the data points and are therefore not shown.*

spirals around a single-bore ceramic rod was found to be the best configuration, with a residual magnetic field of less than 1.0 mG at the interaction region for a current of 8 A. This winding style was therefore adopted.

5.3.2 Selection of heating wire

Once the most effective winding style had been established, the next step was to determine which metal should be used as heating wire. Tests were performed on heating elements made up of molybdenum, tantalum and tungsten wires. The same lengths of wire were used in each test but the diameter varied. This investigation involved winding the particular wire in double spirals along the length of a single bore ceramic rod. The available metallic wires which were tested were: 0.3 mm diameter molybdenum, 0.3 mm tungsten and 0.25 mm tantalum. Once wound, the heater element was placed inside a test chamber under vacuum, and current was passed through the wire while the temperature was monitored using a pyrometer. This revealed that all the heaters could reach a

temperature in excess of 1700°C, which was required for gold to be vaporised. However, their reaction to heating cycles was different.

Molybdenum and tantalum were found to expand considerably and the tantalum wire did not then regain its original shape. This was a significant problem as the success of the heaters depended on the double spirals remaining apart from each other. The fact that the wires sagged when heated also meant that the supporting ceramic rod was cooler than the wires themselves. It was found that both molybdenum and tantalum wires could resist several heating cycles without losing their ductility. At the highest temperatures used (2000°C), tungsten was found to expand the least, but it became very brittle after the first heating cycle. Indeed, the performance of the wires rested heavily on their expansion and ductility as well as the coefficient of linear expansion which increases from tungsten to molybdenum to tantalum. The outcome of these tests was that all three metals could effectively be used to attain the high temperatures needed. Although important characteristics of the wire when subjected to heating cycles were revealed through these tests, it was concluded that the final decision regarding the selection of heating metallic wire could only be made after each wire had been tested with the oven prototype. The oven was therefore assembled so that further tests could be carried out. The method of assembling the oven is detailed in section 5.11.

The 0.25 mm thick tantalum wire was the first to be used as heating wire around the ceramic rods and this was tested in the test chamber. In this case, the oven using Ta wire did not easily reach temperatures in excess of 1100°C, which is appreciably below the target temperature. This is because its resistance was found to drop sharply and suddenly at this temperature and therefore a considerably higher power was needed to increase the temperature further. The heater was then turned down and the chamber opened to assess the test. It was found that the tantalum wire had left a metallic coating onto the walls of the boron nitride hole into which it was located. This was possibly due to the vaporisation or burning out of the outer layer of the Ta wire at the high operating temperature. It was postulated that this could explain the observed drop in resistance of the wire, since as it heated up it expanded considerably

(as revealed by former testing) and touched the metallic coating thus shorting the wire. This then decreased the apparent resistance of the tantalum wire, as measured externally. The test was repeated with new tantalum wire and the same observation was noted.

To ascertain and address this problem, the other metal wires were tested in the same way (for similar lengths of wire) and in the following order: tungsten 0.3 mm and molybdenum 0.5 mm thick whose relatively lower resistance required a higher power input to reach temperature; and finally tungsten 0.125 mm. The thin tungsten wire gave most satisfactory results, in terms of power efficiency and lack of reaction or sign of vaporisation. The main difficulty with this heater was that it was particularly difficult to spot weld wires of such small diameter onto the molybdenum pieces onto which they were held (more details in section 5.8). Furthermore, even though tungsten could resist multiple thermal cycles *in situ*, it could not be handled easily *ex situ* as it would crumble due to its brittleness after being heated and cooled. This made maintenance difficult since the wires had to be replaced more frequently due to breaking.

5.4 Oven Design

The assembled oven consisted of a graphite crucible at the centre, which was a hollow cylindrical vessel closed at one end with a nozzle at the other end. It was filled with the target of interest and enclosed into a boron nitride furnace which was resistively heated by six individual heaters housed in radial, evenly distributed holes inside the furnace. The furnace was directly heated by the heaters and it then radiated heat to the core by conduction. This geometry thus ensured uniform heating of the crucible. On heating, the oven reached high enough temperatures to melt and eventually vaporise the target. The furnace was shielded to reduce heat loss. The assembled oven was also contained inside a water-cooled jacket which kept the external body at a reasonably lower temperature to minimise heat radiation to other components inside the spectrometer. The oven was designed in Claris CAD software [112] as illustrated in figure 5.2.

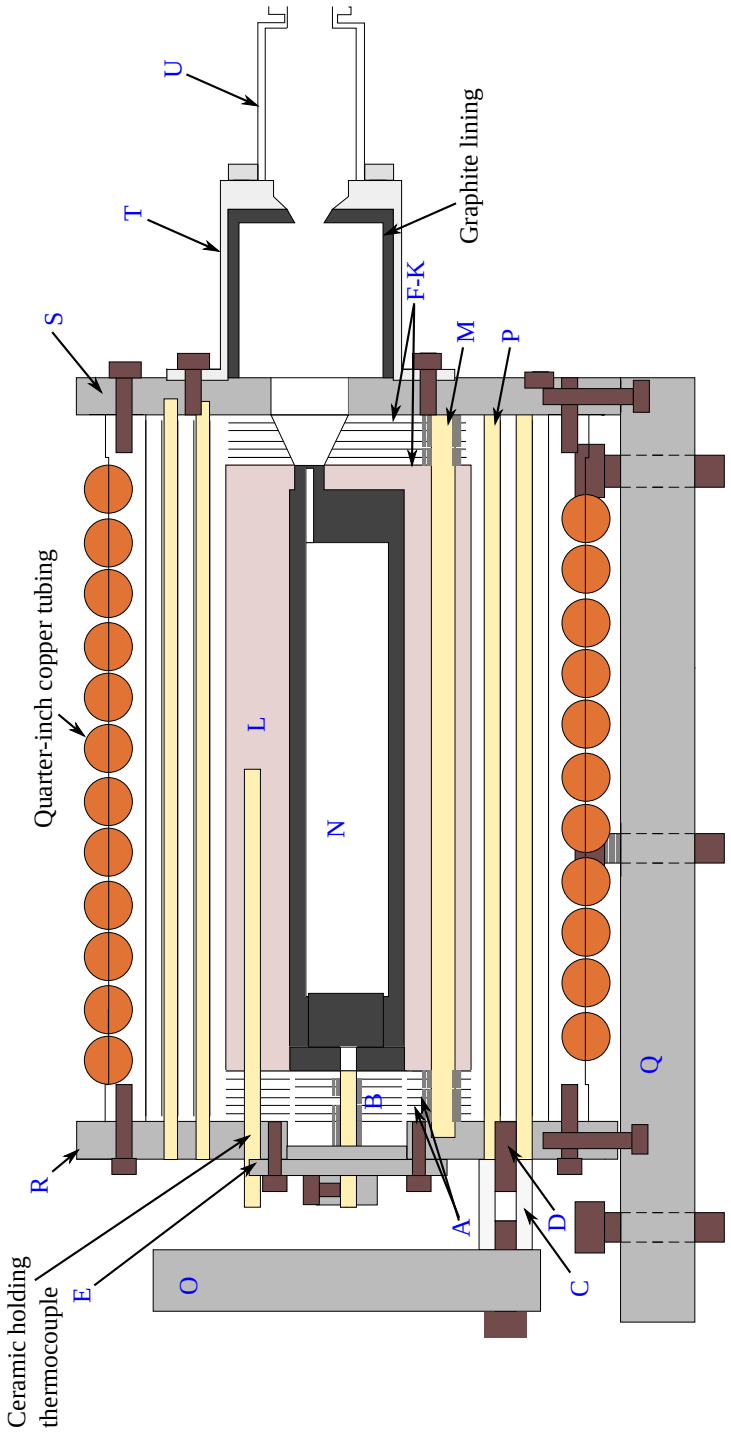

Figure 5.2: *Illustration showing composite view of the high temperature oven as designed using Claris CAD software. The parts are labelled according to table 5.3.*

The sections that follow will detail the various components as shown in figure 5.3 that make up the oven. Various parts will be referred to according to their labelling on the picture.

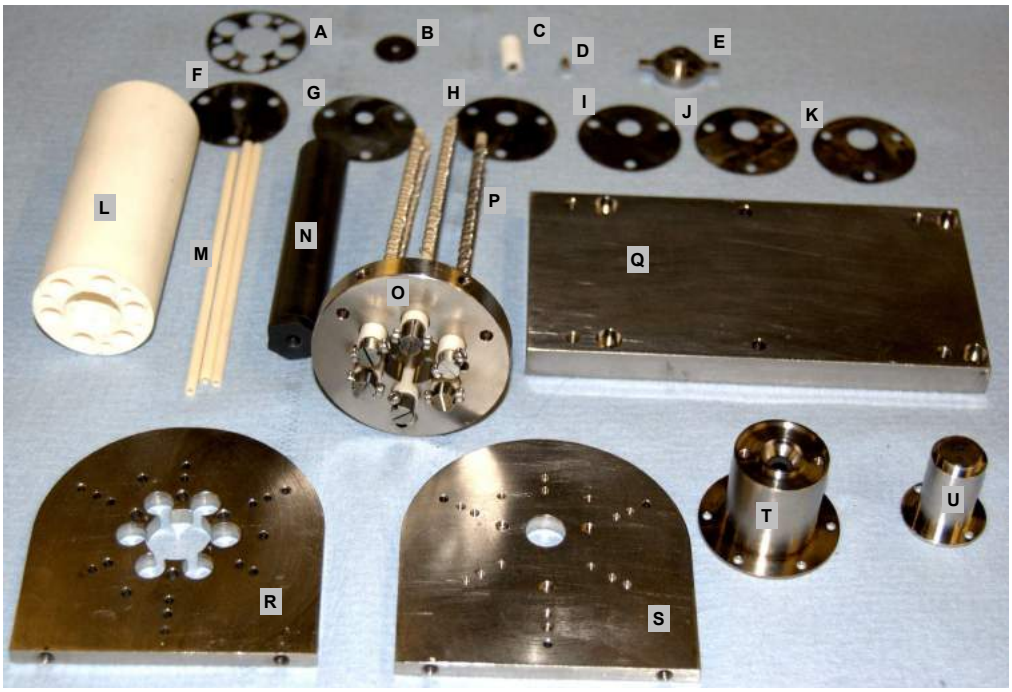

Figure 5.3: *Photograph showing the various parts needed for the oven. Further description is provided in the text.*

The oven assembly was mounted between two face plates, a front plate (S) and a back plate (R). These were fixed onto the oven yoke (Q) using four 2 mm A4 grade stainless steel screws. All screws used in the construction of the oven are A4 grade stainless steel which are non-magnetic. The assembled oven then rested onto a base plate inside the spectrometer using four M4 screws which could be screwed in or out to allow height adjustment of the oven. The base plate was fixed onto the mounting plate of the chamber via four 20 mm posts and held down using M4 screws. Such a design facilitated the removal of the complete oven body either for recharge or inspection without disruption of its alignment to the interaction region.

Element	Crucible Material
A	Heat discs (back)
B	Heat discs (central, back)
C	Macor screw holder
D	Screw for part E
E	N plate at the back
F-K	Heat discs at the front
L	Boron nitride furnace
M	3 mm OD Al_2O_3 ceramic rods
N	Graphite crucible
O	Heater support plate
P	Heater element
Q	Oven yoke
R	Back plate
S	Front plate
T	Skimmer cylinder
U	Small skimmer cylinder with aperture

Table 5.3: *Description of various parts of the oven as shown in figure 5.3. Further details are provided in the text.*

5.5 Heat shielding

The inclusion of effective heat shielding is crucial to the efficient operation of high temperature atomic beam sources [46] . In order to keep the power required to operate the oven down at practical levels, it was essential to reduce the amount of heat loss. Limiting the heat loss can significantly reduce the power consumption of the oven by confining the energy which would have otherwise been lost to the oven core. Generally, heat flow can occur by conduction, convection and radiation. In this case, heat loss by convection was minimal as a result of the high vacuum under which the experiment was performed. Conduction was minimised by careful design and construction of the oven. As an example, the oven was supported by the use of thin-walled ceramic rods, which isolated the assembly from the surrounding base plates and other structures which were generally made of metal and were therefore conductive.

Radiation however, which is the most significant mode of heat loss, could not be be thus limited and so this required the use of heat shielding. The method employed here utilised a number of metal shields in the form of cylinders sepa-

rated by a vacuum gap thus resisting the flow of radiation. Each shield reflected back approximately 50% of the energy radiated onto it back to the oven furnace.

Increased power efficiency was of utmost importance in this experiment. Ideally, power consumption needed to be minimised otherwise the actual delivery of the necessary power to the oven would be problematic. Cables and electrical connections had to be able to withstand the electrical load needed to generate the power and it had to be ensured that no material was unduly heated.

In the case of the prototype oven, the furnace had an exposed surface area of approximately 80 cm^2, neglecting the end faces. In equilibrium, an ideal black body of the same dimensions would radiate a power of approximately 2300 W. The furnace is not a black body and boron nitride has emissivity <1 hence the power loss was lower but still too large to be easily delivered in practice. For the purpose of this project it was considered vital to keep the power supply unit simple and inexpensive, whether it was built in the workshop or purchased commercially.

By using a number n of heat shields, the power required to heat up and maintain the crucible at the required temperature could be considerably reduced. The effect of heat shielding on power efficiency can be easily demonstrated. For an unshielded oven in thermal steady state, the power loss at the required temperature is P. Consider shielding the oven with metal shields. The shields are assumed to be infinitely long cylinders with negligible wall thickness such that the power radiated inward by the shield is equal to the power radiated outward. Consider the effect of n number of shields, S_0 to S_n. For the first shield only, the power radiated is P_0 both inward and outward. However it also absorbs power P from the oven core and P_1 from the outer neighbouring shield. Hence, in equilibrium

$$\begin{aligned} 2P_0 &= P_0 + P + P_1 \\ P_0 &= P + P_1 \end{aligned} \tag{5.1}$$

For heat shield S_1, similar power considerations dictate

$$2P_1 = P_0 + P + P_2 \tag{5.2}$$

and for shield S_n

$$2P_{n-1} = P_{n-2} + P_n \tag{5.3}$$

By substituting 5.1 in 5.2 and through repeated substitutions, it can be shown that

$$P_n = P_0 - nP \tag{5.4}$$

Since $P_n = P$ by conservation of energy

$$\begin{aligned} P(1+n) &= P_0 \\ P &= \frac{P_0}{(1+n)} \end{aligned} \tag{5.5}$$

It can be concluded that the power needed to maintain the oven at the desired temperature is reduced by a factor (n+1) by the use of n shields. Whilst it has been demonstrated that an increased number of heat shields inevitably reduces power consumption, in practice a compromised number of shields had to be used. The number of heat shields was restricted by the geometrical dimensions of the experiment. The oven was designed to be installed into existing spectrometers and the space into which it could fit was therefore limited by the size and position of other components in the chambers. In part for this reason, it was decided to use five shields. From the mathematical treatment above, it can be postulated that the theoretical power required would be approximately 450W which was considerably reduced.

Description of heat shields

Five concentric heat shielding cylinders, made from 0.127 mm thick molybdenum sheet surrounded the oven furnace as shown in figure 5.4. The number

Figure 5.4: *Photograph showing the five heat shields cut from thin molybdenum sheets and spot welded using a thin piece of tantalum strip. When mounted around the crucible, they are separated by thin-walled ceramic rods.*

of heat shields chosen for this design was established after preliminary tests revealed the effect of one heat shield in the first instance, and the subsequent addition of more heat shields, on the power needed to reach the target temperature. Five heat shields were deemed reasonable for the improved power efficiency. Furthermore, as already mentioned, the geometric considerations imposed by the fact that the oven had to fit in the spectrometer restricted the total size of the oven. The heat shields were made from flat foil molybdenum sheet, cut to the right dimensions, rolled up and spot welded together with a strip of tantalum as shown in 5.4. The tantalum strip was necessary because molybdenum does not easily spot weld to itself. The cylinders were separated by 2 mm OD thin walled alumina ceramic rods (M) which located into guide holes in the two face plates (R and S). These secured the shields in place, whilst simultaneously ensuring equal space between any two of them and ensuring minimal contact. The heat shields were 92 mm long, slightly more than 1 mm shorter than the oven, in order to further reduce physical contact (with the face plates) and hence heat loss by conduction.

5.5.1 Heat shields at the back of the oven

Additional heat shielding was necessary in order to minimise thermal losses from the front and back of the oven. Six 32 mm diameter heat discs (B), made from 0.127 mm thick molybdenum sheet were designed for shielding the back of the oven crucible. They were mounted onto a 2 mm OD ceramic tube which was fitted through a hole to a plate (E) as shown in figure 5.5. The plate was made of tantalum and was essentially a 24 mm diameter, 2 mm thick circular

Figure 5.5: *Photograph showing the "N-plate" holding a ceramic rod onto which six heat discs are mounted.*

plate, with a stepped down 3 mm thick, 8 mm diameter plate. It secured the centrally located ceramic rod via an M2 A4 screw which then held all the thin heat discs, spaced apart by ceramic spacers. These shielded the crucible. For more effective shielding, the outer part of the boron nitride furnace was also shielded by using six discs (A) machined to match the cross-section of the furnace which the discs cover at the back. They were supported on the oven support rods and kept apart using ceramic spacers. The heat discs had holes drilled to accommodate the heaters and thermocouple that were inserted into the boron nitride furnace.

5.5.2 Heat shields at the front of the oven

Six additional heat discs (F-K) between the boron nitride furnace and the front face plate helped to minimise heat losses. They were 31.5 mm in diameter, machined from 0.127 mm thick molybdenum sheet with three 3 mm holes in each for the ceramic oven supports to go through. A central hole was drilled in each, in increasing size further away from the boron nitride furnace, in order to allow for the spread of the atomic beam as it emerged from the nozzle of the oven. This design prevented unnecessary material deposition onto the heat

discs when the oven was in operation.

5.6 Graphite Crucible

The crucible contained the material to be vaporised. The oven crucible used was a one-piece hollow cylindrical vessel which was open at one end and with a nozzle at the other end. The 1.2 mm ID nozzle at the front is shown in figure 5.6. The crucible was constructed from high density graphite into an 80 mm long cylinder with internal and external diameters of 10 mm and 16 mm respectively. The rear of the crucible had a threaded 10 mm hole into which a graphite screw was inserted to tightly seal the oven.

Figure 5.6: *Photograph showing the nozzle at the front of the graphite crucible. The nozzle acts as emission hole from which the target vapour escapes the oven. As can be seen, it is offset from the centre to allow the maximum possible amount of sample to be loaded into the crucible.*

As the crucible was heated, the material melted and then vaporised. The pressure inside built up and the element was released as a fine beam through the nozzle at the front. The nozzle which delivered the target atoms into a quasi-collimated beam had an internal diameter of 1.2 mm, an external diameter of 4 mm and was 10 mm in length. It was offset from the centre to the top of the main cylindrical body of the oven to allow the maximum possible amount of material to be charged into the crucible, whilst ensuring that once melted, the liquid material did not overflow.

The maximum amount of material that could be loaded into the crucible was calculated in order to ensure it was never overfilled. The cross section of the part of the oven that can be filled is as shown in figure 5.7.

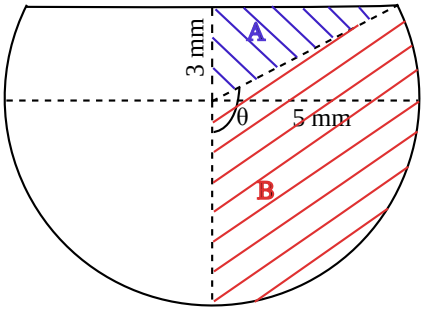

Figure 5.7: *Illustration of the cross-section of the oven representing the part that can be filled.*

The length of the crucible that could be occupied excluded the length of the threaded hole at the back and was therefore 70 mm. To determine the volume of charge that could be fitted without overflow, the area of the cross section had to be calculated. This is equivalent to twice the area (A+B) from figure 5.7. Area A and B are calculated as:

$$A = (0.5 * 3 * 4)mm^2 = 6mm^2 \tag{5.6}$$

$$B = (2\theta/2\pi) * \pi * r^2 = 8mm^2 \tag{5.7}$$

The total cross sectional area is therefore 28 mm^2 and the volume is ~1.96 cm^3. Since the density of silver is ~ 10.5 g cm^{-3}, the maximum amount of silver that could be charged into the crucible was therefore approximately 20g. In practice, a cylindrical charge of dimensions 30 mm length x 7 mm diameter was used, with a mass of about 12 g, which is safely below the maximum limit of 20 g. It was thus ensured that any material to fit into the space would occupy a smaller volume than the calculated maximum threshold.

5.7 Boron Nitride Furnace

The furnace was machined from commercially available high-purity boron nitride into a cylinder, 80 mm long and 32.5 mm in diameter. Six 77 mm long

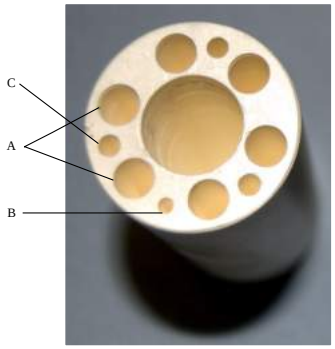

Figure 5.8: *Photograph showing the cross section of the boron nitride furnace. Six 6mm diameter holes marked A were drilled to contain the six individual heaters. The hole into which the thermocouple was inserted is labelled B. Three 3 mm holes housed the ceramic support rods.*

through holes of 6 mm diameter housed the six individual heaters. This is illustrated in figure 5.8.

These holes were stepped down to 3.5 mm at the front of the furnace in order to locate and stop the Al_2O_3 ceramic rods [113] used for the heaters. A 2 mm hole was drilled half-way along the length (40 mm) to hold a thermocouple in order to monitor the temperature inside the furnace. The thermocouple junction was thus located mid-way along the furnace and provided an accurate measurement of the temperature inside the oven. The thermocouple was constructed in house and as a Type C tungsten rhenium one, made by joining a tungsten-5% rhenium alloy wire to a tungsten-26% rhenium alloy wire [114]. Three 3 mm holes were also drilled through for the support rods which were 3 mm OD thin walled ceramic rods. A 4 mm ID hole at the front of the furnace allowed the nozzle of the graphite crucible to fit in. The furnace used a 4 mm ID hole as output hole into which slot the nozzle of the crucible. This also directed the atomic beam towards the interaction region.

5.8 The Heaters

Figure 5.9 shows the assembled heaters. There were six of these which mounted into the boron nitride furnace. Each heater consisted of a pair of molybdenum plugs, half-cylindrical in shape, a ceramic rod, tungsten wire, M2 screws and a flat piece of 0.6 mm thick ceramic, 19 mm by 6 mm in dimensions.

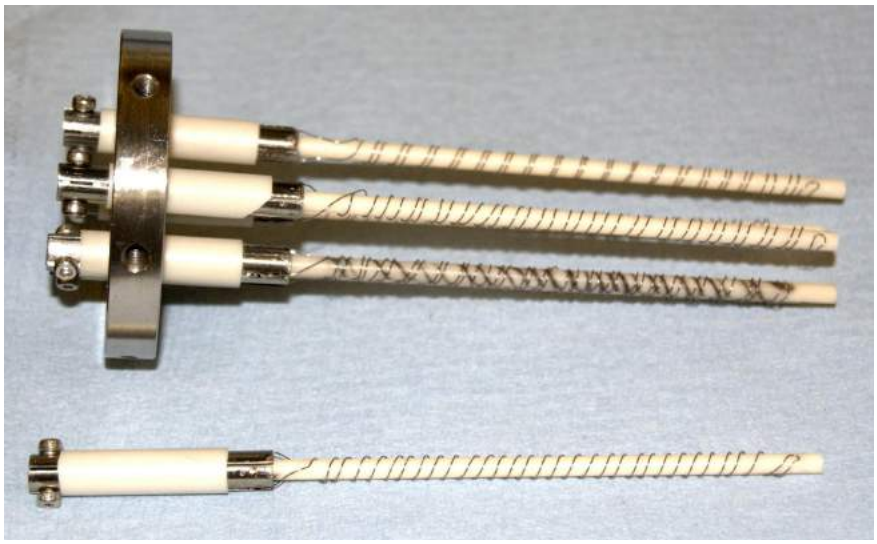

Figure 5.9: *Photograph showing an assembled heater and all six heaters mounted onto the heater support.*

The molybdenum plugs were machined in matched pairs. Each pair was made from a 6 mm molybdenum rod 37 mm in length. A 3 mm ID 17 mm long hole was drilled at one end in order to secure the 3 mm OD ceramic rod (M). The molybdenum cylinder was then halved to produce a matched pair of plugs.

A 300 mm length of 0.125 mm tungsten wire, approximately 300 mm long, was turned halfway along the length so as to form a 150 mm length of parallel running wire, connected at one end only. This was passed through two bores of a four-bore ceramic tube to ensure they remained parallel and uniformly spaced. The "double-wire" thus obtained was wound spirally along the length of the thin walled 3 mm OD ceramic rod. The windings ended with two short lengths of straight tungsten wire which were each spot welded onto a molybdenum plug from a matched pair, whilst the ceramic rod located inside the grooves

of the molybdenum halves. With the ceramic rod thus secured between the molybdenum plugs, the flat piece of ceramic sheet was inserted between the plugs at the other end. This ensured the molybdenum halves did not touch.

5.9 The Skimmer

Located at the front of the oven furnace, the skimmer assembly collimated the crude beam emanating from the nozzle into a fine beam. This was achieved by using two cylindrical pieces made of 310 stainless steel. These were the skimmer, 26 mm long with a 22 mm OD and a 24 mm long 12 mm OD collimation chamber. The collimation chamber was screwed onto the skimmer using two M2 screws. The skimmer reduced the flux of atoms entering the collimation chamber which had an aperture of 2 mm at the end. A piece of thin advance sheet, cut to size, with a 1.0 mm aperture was spot welded at this end. This resulted in an atomic beam with angular spread of $\pm 1.5^{o}$. The skimmer was not directly heated and therefore remained at a lower temperature than the crucible. Upon exit from the nozzle, the atoms that did not eventually go through the aperture condensed on the inside of the skimmer. The internal surfaces of the skimmer cylinders were in fact lined with 1.5 mm thick high density graphite. Unwanted vapour therefore collected on the graphite rather than the stainless steel interior surfaces. Such a design allowed the easy reuse of the material deposited in the skimmer by sacrificing the graphite coating.

5.10 Water-cooled Copper Jacket

Due to the projected high temperature and power requirements of the oven, it was deemed necessary to water cool the chassis (i.e. whole oven body). This was expected to help keep the front and back plates of the oven reasonably cool and minimise the heat radiated to other components inside the vacuum chamber. This was essential as certain components, e.g. channeltrons, can be sensitive to high temperatures and indeed may even be damaged beyond a certain temperature.

Figure 5.10: *Photograph showing the graphite lining inside the skimmer cylinder. This ensured the skimmer remained re-usable by preferential sacrificing of the graphite.*

A water-cooled jacket was therefore designed for this purpose. A 93.5 mm long hollow cylinder was constructed from solid copper, 64 mm in diameter. The ID of the copper jacket was 53.5 mm, thus dimensioned so that it rested against the outermost heat shield. The jacket was also the right length to hold the whole oven together, hence acting as a supporting chassis in lieu of supporting rods. Grooves 63.5 mm wide, 3.175 mm deep and 0.5 mm spaced apart were machined along the exterior wall of the copper cylinder to accommodate quarter-inch copper tubing. The copper tubing was wound along the copper vessel and ended in two straight pieces of approximately 100 mm to which were connected two stainless steel flexible tubings via quarter-inch swage lock fittings. The stainless steel tubings could be flexed and were connected to a water feedthrough which made the connections to the external water pipes.

A thermocouple was attached to the copper jacket in order to monitor its temperature when the oven was heated up. Under operation of the oven, water was run through the copper pipes and this maintained the chassis at a temperature below 150°C. Prior to this the oven prototype had been tested without the flow of water in the pipes. With the furnace at a temperature of 950°C the temperature of the copper jacket (i.e. external surface of the oven) reached

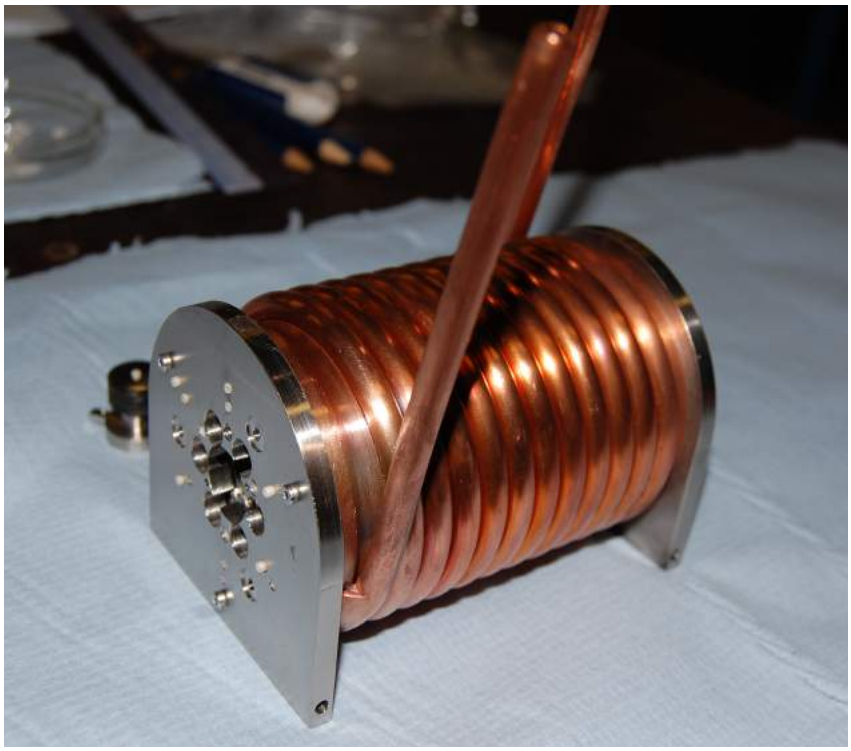

Figure 5.11: *Photograph showing water cooled copper jacket mounted onto the oven. Steel tubings are connected to the ends of the copper tubes using sewage locks.*

$\sim$300°C which confirmed the necessity of the water-cooled copper jacket.

5.11 Assembling of the Oven

The following describes the way in which the oven was put together using the previously described parts. Various parts are referred to by their labels from figure 5.3.

With the boron nitride furnace (L) lying flat on a surface, the three ceramic support rods (M) were inserted into corresponding holes in the boron nitride. The front heat shielding discs (F-K) were then mounted onto the rods, separated from one another by $\sim$1 mm custom made ceramic spacers. The furnace (L) together with the shields (F-K), was mounted onto the front plate using three locating holes into which the rods (M) were inserted. This partial assem-

bly was placed with the front plate flat so that the remaining parts could be fitted. The six back heat shielding discs (A) were then fit onto the protruding ends of the ceramic rods (M).

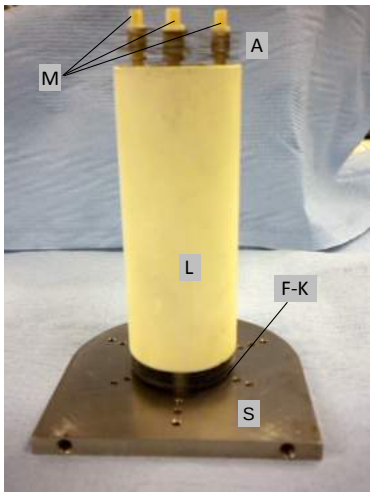

Figure 5.12: *Photograph showing partially built oven.*

A set of 2 mm OD think-walled ceramic rods were placed in radially equidistant blind holes around the furnace. The first smallest heat shield was slid onto the rods. This was repeated until all five heat shields had been inserted, each separated from the other using 2 mm ceramic rods. The water-cooled copper jacket was next inserted onto the last shield, and fixed to the front plate (S) using three M2 screws.

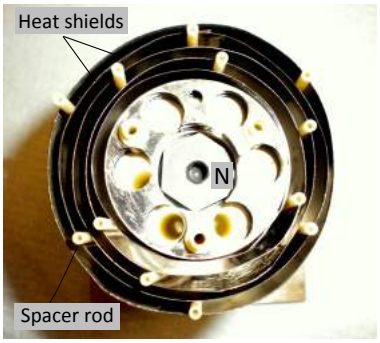

Figure 5.13: *Photograph showing partially built oven.*

The back plate (R) was inserted using the guide holes which located onto the support rods (M) and the ceramic spacers. The back plate was screwed onto the copper jacket using three M2 screws. The oven assembled to this point is as depicted in figure 5.14.

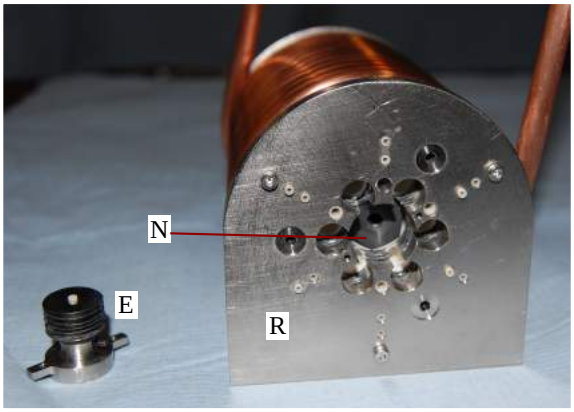

Figure 5.14: *Photograph showing partly built oven. The N-plate (E) with the heat discs can be inserted at the back of the crucible. It is screwed onto the back plate using two 1.6 mm A4 screws. Also shown are the back plate(R) and the graphite crucible(N) which has been inserted inside the furnace.*

The six heaters mounted onto the support plate as shown in figure 5.9 on page 118 were then added as one unit through the back plate and secured using three M4 screws. The thermocouple was then also inserted into its designated hole.

5.12 Power delivery to the oven

All six heaters were used to operate the oven at the desired temperature. The power was provided by passing currents through each heater which typically had a resistance of about 2Ω. The power required to reach the operating temperature of 1200°C was about 230 W. To provide the necessary input power a current of ∼1.6A was passed through each heater at a voltage of ∼24V. The drive current was supplied by three high power sound reinforcement double output power amplifiers by Behringer, EP4000 2x2000W [115].

These amplifiers provided a reliable, simple and inexpensive supply of power. They had been initially considered as a means to potentially eliminate any magnetic fields produced by the heater current. This is because the sinusoidal current could be momentarily switched off at the zero crossing of the AC signal whilst the data signal was being collected and then turned on immediately after. For the current project however, the magnetic field at the interaction region was measured to be less than 3 mG and therefore the AC signal interruption method was not necessary.

5.13 Alignment of the Oven

Prior to operation, the oven had to be aligned to the interaction region, as defined by the gun and analysers. A cylindrical mount of equivalent dimensions to the oven crucible was machined out of phosphor-bronze to facilitate the alignment of the oven. This is shown in figure 5.15.

Figure 5.15: *Photograph showing the custom-made alignment tool which substitutes the oven crucible in the process of aligning the oven to the interaction region.*

A laser diode, which lases at 650 nm, fit at the rear of this mount. A defining aperture could be inserted in front of the diode to define the diameter of the beam emerging from the oven skimmer. The oven alignment could then be carried out: height adjustment was achieved through the use of a variable number of washers inserted under the screws that held the oven base plate onto the pillars. Lateral positioning could be changed by pivoting the complete oven mount about the front screw. Once satisfactory alignment was achieved, the screws were locked down to secure the oven. A complete description of the alignment process is provided in chapter 6.

5.14 Testing of the Prototype Oven

Several tests had to be run before the oven could be deployed for use in actual super-elastic experiments. It was essential to establish several performance characteristics. The oven was turned on for the first time in a test chamber, evacuated to produce similar working conditions as the super-elastic spectrometer. The operating conditions that were being assessed are summarised as follows:

i. Production of a beam of material and deposition of the emitted atoms onto a cold surface.

ii. Temperature measurement and final temperature that could be reached with the oven at full capacity.

iii. Power requirements to reach above temperature.

iv. Stability of the oven and reliability of the filaments.

v. Expansion and subsequent contraction of material subjected to repeated and sustained heating cycles.

vi. Pressure and outgassing rates of materials.

From the above criteria, it would then be assessed whether the oven needed any modifications. The oven was first tested with copper as crucible material. The oven was slowly turned up at a rate of about 100°C an hour. The pressure rose steadily whilst the oven was being brought up to temperature due to outgassing of materials and it was essential to allow the pressure to stabilise before the oven could be further turned up. Once at high enough temperature (1300°C) the oven was left operating for a few days to assess its stability. The first tests concluded with the successful operation of the oven and when the test chamber was eventually opened, a spot of copper could be seen on the cold trap which indicated the oven had vaporised the metal and the nozzle did not get blocked during the heating process. The oven was therefore transferred to the experiment spectrometer.

The first experiments with copper were started. However, even though the oven could be heated to generate a beam of copper atoms, the temperature had to be significantly increased beyond the predicted temperature in order to sustain a stable and high density beam. For this reason it was decided to switch to silver as a target in order to commence the first series of experiments as silver requires a lower temperature for vaporisation.

5.15 Oven Operation

The crucible was filled with a piece of silver cut from a commercially bought rod into a 30 mm x 7 mm cylinder. The oven was operated at a temperature of 1200°C. At this temperature, the silver charge inside the crucible was in the liquid state and it generated a sufficiently large amount of silver vapour which was emitted through the nozzle.

With the oven filled the spectrometer was closed and evacuated. The pressure was allowed to fall down to $\sim$5 x 10^{-6} mbar. The oven was then gradually heated from room temperature, at a rate of 100°C an hour. At a temperature of about 400°C, liquid nitrogen was passed through the cold trap (detailed in chapter 6) so as to activate the trap. Gases and impurities present inside the chamber condensed onto the trap, resulting in further reduction of the internal pressure.

The oven was able to reach full operating temperature in just under two days, the pressure being allowed to drop and stabilise overnight. When not in use, the oven was kept at a temperature of about 900°C, just below the melting point of silver. This allowed the oven to be brought back up to operating temperature when needed in a short period of time while avoiding damage due to rapid repeated thermal cycles.

Any interruption in the operation of the oven occurred mostly as a result of the failure of individual heater filaments. It was noted that one failed heater element would soon be followed by another broken one in what seemed to be

an avalanche effect. This was because failure of any one of the six heaters subsequently implied a heavier average load on each of the remaining five, thus further limiting their lifetime.

5.15.1 Problems and Redesigns

Despite testing of the oven prototype, a number of problems were encountered only when the oven had been running inside the super-elastic spectrometer. The heater elements were identified as a main weakness. During repeated maintenance sessions, different causes were established for the failure of the filaments. Firstly, mainly the spot welded end of the filament would break and lose contact with the molybdenum plugs thus resulting in a short circuit. At other times, burnt out spots were not uncommon. The creation of weak points by the gradual wearing out of the filament cross section resulted in local concentration of high currents in the elements. These eventually burnt and created short circuits.

Certain problems were encountered and overcome only after the oven had been running for a longer period of time (continuous weeks). On one occasion, it was observed that the data signal was decreasing over time until none could be detected at all. The temperature of the front plate of the oven was seen to have risen considerably. After eliminating any other possible causes (such as failure of the water cooling copper jacket), it was concluded that the oven had been blocked. The chamber was opened. The skimmer was removed from the front in order to check whether the nozzle was blocked as shown in figure 5.16. Indeed it was noted that the nozzle was blocked and this had caused an excessive deposition of emitted silver atoms onto the front heat shielding discs, which had fused together. Thus the heat shields were no longer effective as they were in contact with one another and the front plate. The oven had to be dismantled. The heat shields were cleaned and it was decided to exclude the foremost one when the oven was reassembled.

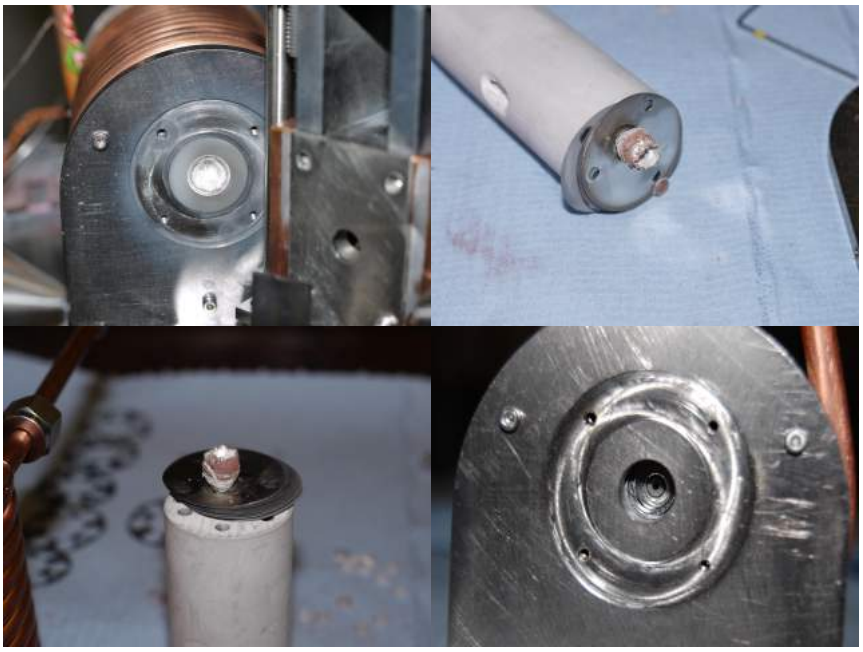

Figure 5.16: *Photograph showing, clockwise from left to right, the blocked nozzle after the skimmer had been removed for inspection while the oven was still mounted in the spectrometer; blocked nozzle showing the front heat discs fused together by the solidified silver; side view showing the piece of silver that blocked the nozzle; and for comparison, the unblocked nozzle.*

5.16 Conclusion

A new high temperature atomic beam source has been designed and constructed to deliver beams of silver, copper and gold. A temperature of about 1400°C could be reached and sustained. The oven has successfully produced beams of silver and copper but gold has not been used so far as a target. As a result of the design of the oven, the graphite crucible can easily be replaced with one made from another material thus making the oven potentially compatible with a large range of atomic targets. The oven has been used to investigate inelastic and super-elastic scattering from silver as described in chapter 7.

Chapter 6

Experimental Apparatus for Silver Experiment

6.1 Introduction

This chapter presents the set-up for the super-elastic experiments carried out using silver as the atomic target. The experiments were conducted inside an existing evacuated chamber previously used in coincidence experiments [116] and so it housed all the essential components. The experimental apparatus comprised of the evacuated chamber, the atomic beam sources (oven and gas jet nozzle), electron source and two detectors, laser system and optical components including mirrors, polarisers and wave-plates.

Figure 6.1 shows a schematic illustration of the arrangement of the apparatus. The instruments are arranged inside the vacuum chamber in a crossed-beam configuration. The electron gun and detectors as well as the atomic sources all point to the *interaction region* defined by the intersection of their axes with the laser beam. The principle of the experiments is identical to the ones performed using calcium as described in Chapter 3. However, in these experiments a second electron analyser was also used. Briefly, a resistively heated, high temperature effusive oven operating at $\sim$1200^{o}C produced a collimated beam of silver atoms. The design of the oven has been described in Chapter 5 and produced a beam with angular spread of $\pm$ 1.5^{o}. A single-mode, continuous wave laser system generated a polarised UV light beam at 328.163

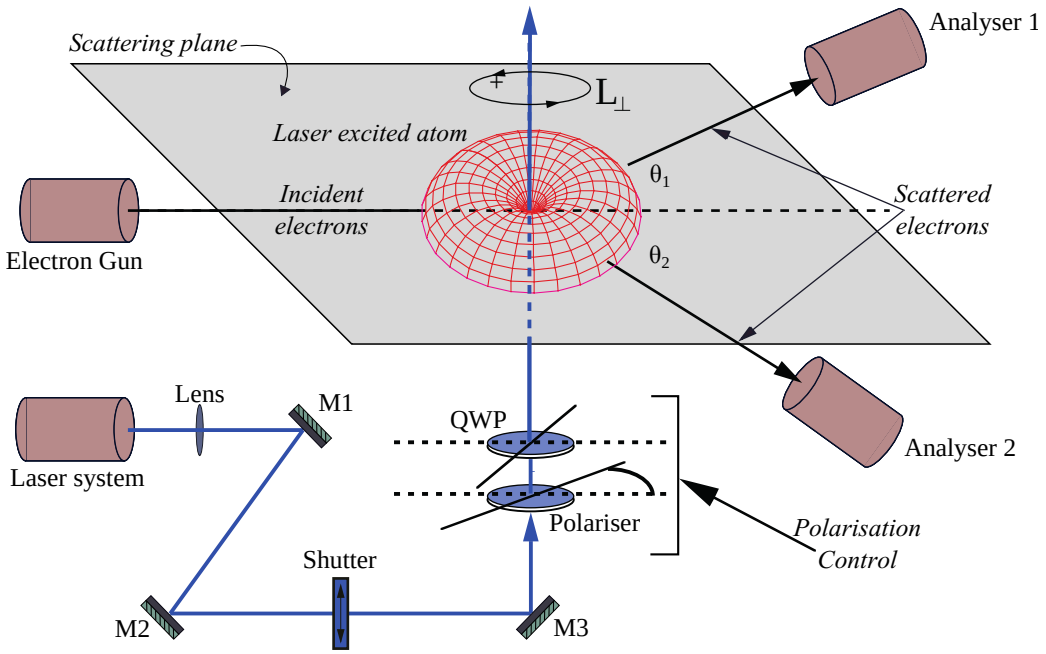

Figure 6.1: *Schematic illustration of the apparatus used for the super-elastic scattering experiments performed with silver. Laser radiation at 328.163 nm excited silver atoms emitted by the oven. Incident electrons from the electron gun collided with the excited target atoms which then relaxed to the ground state. Electrons that had gained energy collisionally and which were scattered at angles θ_1 and θ_2, were detected by analyser 1 and analyser 2 respectively. The scattering plane is defined by the momenta of the incident and outgoing electrons. The laser system and optical set-up shown here are discussed in sections 6.7 and 6.8*

nm which was used to excite the silver atoms from the $5^2S_{1/2}$ ground state to the $5^2P_{3/2}$ excited state. Optical elements were used to direct and define the laser beam before it entered the vacuum chamber. These include UV mirrors used to steer the laser beam into the chamber, and polarisers and a quarter-wave plate to control the polarisation of the laser beam as required for super-elastic experiments. An electron gun generated a source of electrons with well-defined energy which then collisionally de-excited the laser-excited atoms at the interaction region. The super-elastically scattered electrons were detected, as a function of scattering angle and laser polarisation, by a pair of identical analysers located in the detection plane. The analysers were energy selective and super-elastic scattering events from the silver atoms could be discriminated from other energy-dependent interactions such as inelastic scattering or ionisa-

tion. The relationship between the incident and outgoing energies for electrons in a super-elastic scattering event was

$$E_{out} = E_{inc} + 3.778eV \tag{6.1}$$

The data was acquired using measurement electronics and computer-based programs. These will be discussed in following sections. Controlling voltages, currents and signals were passed from the exterior to the interior of the spectrometer via electrical feedthroughs located underneath the bottom plate of the chamber. Via these feedthroughs, the connections to various thermocouples were made in order to monitor the temperatures at various points in the chamber. The main components of the experiment will be described in this chapter. Data was taken using circularly polarised light which allowed the determination of the parameter $L_{\perp}$. This was carried out over a range of energies from 20 eV to 100 eV across a range of scattering angles from $\theta_e = 20^o$ to $\theta_e = 130^o$.

6.2 The Spectrometer

The super-elastic studies on silver were performed inside a chamber which was vacuum sealed to a low pressure of $\sim 3\text{x}10^{-7}$ mbar when no gas was being injected. The apparatus had been commissioned prior to the start of this project and had been extensively used in previous experiments, as described in preceding literature [117]. It was originally designed for coincidence studies, hence the presence of two electron detectors as will be discussed in the following sections. It could however be easily adapted, with minor changes for the super-elastic experiments conducted here.

The spectrometer comprised the necessary components including the atomic beam oven, electron gun and the two electron detectors which were mounted on the top surface of a baseplate internally fixed at the bottom of the chamber. The electron gun was fixed in position such that the generated beam of electrons was incident in the scattering plane as shown in figure 6.1. The analysers

were located on two separate concentric turntables and could be rotated around the interaction region using rotary feedthroughs. On the external surface underneath the bottom flange were located twelve CF-70 flanges which served to make the connections to the spectrometer. The temperature of various parts of the chamber could also be monitored via specific feedthroughs connected using these flanges.

When the baseplate and components needed to be accessed, the chamber could be lifted using four high pressure pneumatic cylindrical rams. This allowed the chamber to be either lifted or lowered smoothly.

The spectrometer and laser system could be computer-controlled making continuous operation feasible without the need for user intervention. This was particularly useful at lower energies where the signal to noise ratio was reduced, necessitating longer operating times.

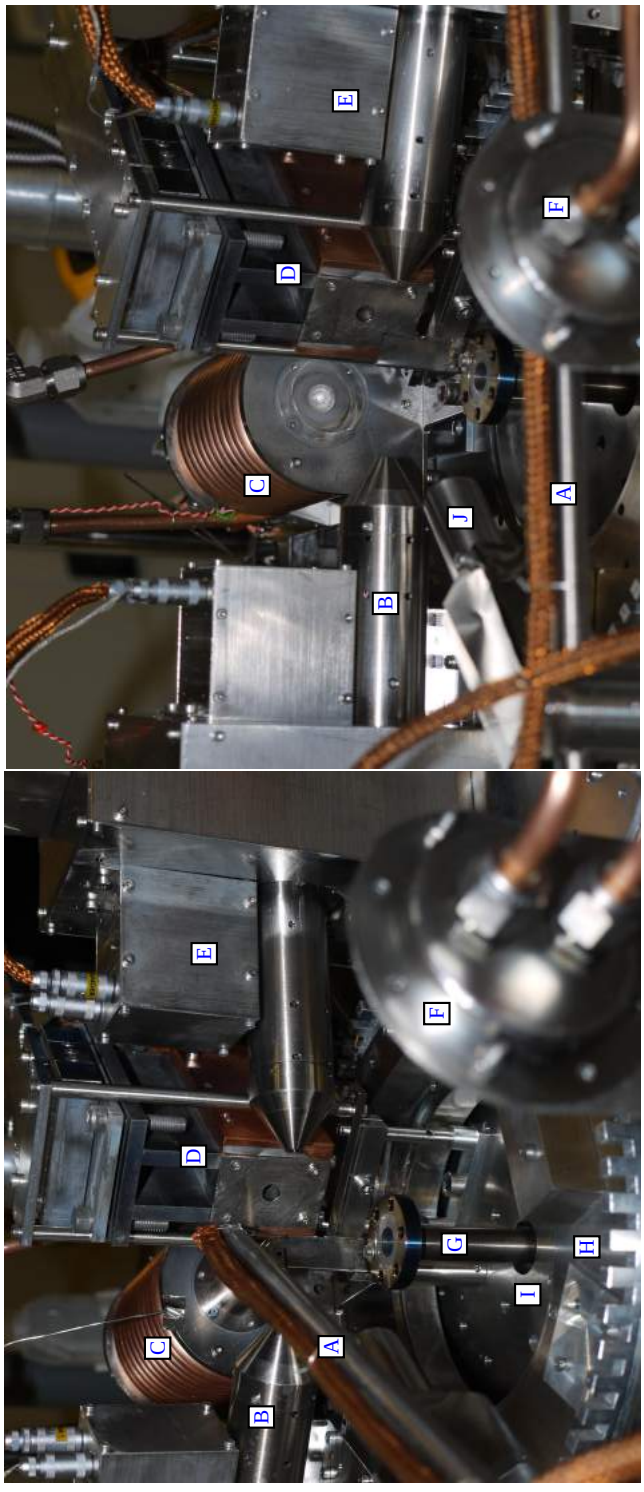

Figure 6.2: *Photographs, from two slightly different angles, illustrating the arrangement of the main components of the spectrometer around the interaction region as follows: (A) Gas jet, (B) Analyser 2, (C) Atomic beam oven (D) Electron gun (E) Analyser 1 (F) Cold trap (G) Oven "obstructer" (H) Inner turntable (I) Baseplate (J) Faraday cup.*

6.2.1 The Vacuum Chamber

The super-elastic spectrometer was located inside a 600 mm high cylindrical chamber with a diameter of 760 mm, constructed out of 310-grade stainless steel which has negligible magnetic permanence. The chamber could be lifted to access the spectrometer. The top flange of the chamber rested onto a bottom flange and formed a seal via a Viton O-ring situated within a circular groove on the bottom base plate of the chamber. Four viewpoints spaced 90^{o} apart were located on the side of the chamber. They were used for experimental viewing when the chamber was closed and for the detection of fluorescence from the excited atoms. The chamber was lined on the inside with mu metal to minimise the effects of external magnetic fields down to about 5 mG at the interaction region. All other components of the experimental apparatus were manufactured from non-magnetic 310 grade stainless steel, molybdenum or titanium. Aluminium was also used, but only sparingly because of its high outgassing rate in vacuum.

It is essential to perform electron-atom collision experiments in a high vacuum environment. This is to ensure minimal interaction of the beam of atoms with background gases. The low pressure condition ensures that the mean free paths of the projectile electrons and the target atoms are greater than the physical dimensions of the apparatus. Additionally, the maintenance of high vacuum is also necessary for the production of an atomic beam through resistive heating. A sufficiently low pressure must be maintained to minimise oxidation of the refractory metals used in the construction of various parts of the oven.

The chamber was hence pumped by a TURBOVAC 340M turbomolecular pump [118] which was backed by a 30 l/s EDWARDS XDSi 750 rpm scroll pump. The chamber was first closed ensuring the proper location of the O-ring into the groove. The sealed chamber was then evacuated by the scroll pump until a pressure of about 10^{-3} mbar was achieved. After the initial pumpdown, the turbomolecular pump was switched on whence the pressure decreased to $\sim 10^{-7}$ mbar. Activation of a cold trap, located opposite the oven, further reduced the pressure. The pressure inside the chamber was monitored using an ionisation gauge.

6.3 The Electron gun

The electron gun used for the experiments with silver is conceptually identical to the one used in the calcium spectrometer. It was initially designed by Woolf [119]. Briefly, the gun consists of a tungsten filament which thermionically emits electrons, two apertures for collimation, two electron lenses for focussing and three XY deflectors that correct for any misalignment of the beam. The energy resolution of the gun is dictated by the process of thermionic emission from the cathode and was estimated to be about 600 meV. The incident energy of the emitted electrons could be varied from $\sim$5 eV to 100 eV. The principle of operation of the gun has already been described in section 3.4 and will not be reiterated here.

A Faraday cup, in the form of a metal plate, as shown in figure 6.2, was mounted directly opposite the electron gun, onto which electrons were collected after going through the interaction region. The Faraday cup was connected to an electrometer and therefore provided a measure of the beam current. When operating at 100 eV, the gun was able to provide a collimated electron beam with a current of up to 5 μA at the interaction region, as measured by the Faraday cup.

The energy of the electron gun was calibrated against the elastic helium resonance spectrum which has a characteristic structure at 19.366 eV. This procedure, described in section 7.2.1 was essential to determine contact potentials which are principally due to the filament work function and the use of dissimilar metals in the chamber.

The electron gun was fixed in position to the mounting plate inside the vacuum chamber. This is shown in figure 6.2. As already mentioned, proper alignment of the components of the spectrometer to the interaction region is crucial in these experiments in order to reduce uncertainties in the experimental data, and also to maximise the super-elastic signal. It has been observed that

small misalignments can lead to significant decrease in the super-elastic yield, which render measurements more challenging. A laser diode fixed at the back of the electron gun aided in the alignment of the gun. Since the gun was fixed, the laser diode effectively defined the path of the electron beam that was generated when the gun was running. The alignment process could be achieved using the laser diode fitted into the gun, together with two other alignment lasers that could be inserted into the back of the analysers, a trace laser running vertically downwards and the actual laser beam, as well as a laser diode placed in the oven. In this way, the components could be aligned and be made to coincide at the interaction region. Further details of the alignment procedure are given in section 6.6.

6.4 The Electron Analysers

Two identical electron detectors were used to detect scattered electrons from the interaction region. They are similar in design to the analyser used for the experiments with calcium. These two analysers were originally developed and used for coincidence studies [116]. Their principle of operation is similar to the analyser previously described in section 3.5 and will therefore not be detailed here. Briefly, each of the analysers consists of a three-element electrostatic lens system that imaged the electrons from the interaction region onto the entrance aperture of a hemispherical energy selector. The entrance apertures to the lens system limited the angular acceptance to $\pm 3^{o}$. Each selector was able to discriminate electron energies and allowed only electrons with the selected pass energy to pass through to channel electron multipliers (CEMs). Two custom-built preamplifiers, following a previous design [120] then amplified the signal from the CEMs. The amplified signals were then passed to ORTEC 473A constant fraction discriminators, which produced slow NIM pulses that were displayed on ORTEC 449-2 rate-meters. The NIM pulses were also counted by the controlling computer using a data acquisition card as discussed in Chapter 7.

The analysers, referred to as A1 and A2, are mounted on two concentrically arranged turntables, in the form of rings, inside the scattering chamber. A1

is mounted on the external turntable whilst A2 is fixed to the inner turntable. Each turntable is connected to a drive pulley which can be rotated from outside the vacuum chamber by means of rotational feedthroughs. The analysers are oriented such that they always point to the interaction region. They could be accurately aligned to the interaction region using two custom-made diode lasers that were made to fit at the back of each analyser. This is detailed in section 6.6.

The analysers could thus be rotated around the scattering plane whilst always pointing at the interaction region. The rotation of the analysers was however restricted by the physical dimensions of the electron gun, the atomic beam oven and the Faraday cup. The angular range that could be accessed by the analysers is illustrated in figure 6.3. As can be seen, the scattering angles that could be accessed by A1 lie between $\theta_1 = 65^o$ and $\theta_1 = 130^o$. At $\theta_1 = 130^o$, A1 runs into the electron gun and therefore could not access higher scattering angles. The lower angular limit was imposed to prevent damage of the analyser due to a high flux of atoms from the oven. A2 could rotate from $\theta_2 = 20^o$ to $\theta_2 = 80^o$, its higher angle of rotation being restricted by the atomic beam oven. Analyser A2 was limited to $\theta_2 \geq 20^o$ to minimise scattering of the incident electron beam from the side of the analyser.

For any particular scattering event, the analysers detected electrons with energy E_{out}. In the case of super-elastic scattering, E_{out} corresponded to the energy of electrons that have gained energy of 3.778 eV during the collision process. The analysers were located on opposite sides of the incident electron beam, as can be seen from figure 6.3, hence when $|\theta_1| = |\theta_2|$ then $L_\perp(\theta_1) = -L_\perp(\theta_2)$. This relationship was true for a range of angles which could be accessed by both analysers from $|\theta_1| = |\theta_2| = 65^o$ to $|\theta_1| = |\theta_2| = 80^o$ For these angles, it was possible to define a common scattering angle $\theta_e = |\theta_1| = |\theta_2|$. The data from A1 and A2 at these common points could be compared and their relative equivalence allowed direct assessment of the quality of the data.

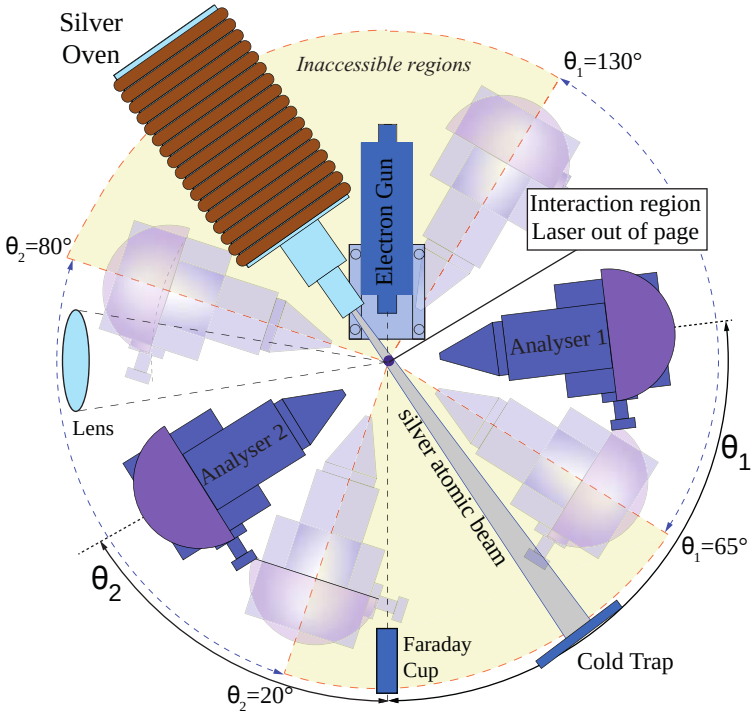

Figure 6.3: *Illustration of the spectrometer as viewed from above the scattering plane, showing the atomic beam oven, the electron gun, two electron analysers A1 and A2, the Faraday cup and the cold trap onto which atoms are deposited after passing through the interaction region. The regions that are inaccessible to the analysers are also marked.*

6.5 Atomic Beam Sources

6.5.1 Noble Gas targets

As was the case with the calcium spectrometer, gaseous targets were sometimes needed for calibration. Gas targets could also be used to diagnose a number of problems such as poor performance of the electron detectors, thus avoiding the need to interrupt the experiment in order to open the spectrometer. Lastly, a beam of argon atoms was occasionally used for tuning purposes especially for the analysers. To ensure the analysers were correctly tuned, inelastic scattering from argon was detected prior to attempting scattering from silver. By tuning onto the known inelastic peaks of the gaseous targets, the voltages of the analysers could be optimised. The gases were injected into the spectrometer by means of a gas jet nozzle. The gas flow rate could be varied by means of an externally located needle valve. Helium and argon were the two gases used during the course of the experiments. The procedure to use them is identical to the one employed in the case of the calcium spectrometer, detailed in section 3.3.1.

6.5.2 Atomic Beam Oven

As described in chapter 5, a beam of silver atoms was produced using a purpose-built high temperature oven. The oven had been designed for intended use with copper, silver and gold. The design consisted of a crucible containing the target material (in this case silver) resistively heated by six individual heater wires. The oven also had an exit nozzle from which the vaporised material exited the oven. This happened when the metal was heated to a sufficiently high temperature ($\sim$1200^{o}C for silver) so that the beam was vapourised and then emitted from the oven via the nozzle. Details of the design, initial testing and operation of the oven have already been given in Chapter 5. During operation, the temperature of the oven was monitored and adjusted in order to ensure the density of atoms at the interaction region was sufficient to produce an observable super-elastic signal, without significant radiation trapping of the laser beam.

6.5.3 Liquid nitrogen cold trap

A cold trap was constructed out of a sheet of molybdenum metal about 3mm in thickness which was positioned directly opposite the atomic beam source, 210 mm beyond the interaction region. This is shown in figure 6.2. A gravity-fed liquid nitrogen metal tube system, similar to the one described in section 3.7, held the cold trap at a temperature of ∼-200°C. After passing through the interaction region, silver atoms emitted from the oven deposited on the cold trap where they condensed and were therefore "trapped" as a result of the low temperature.

The cold trap was crucial in providing a surface where the silver atoms were effectively dumped. This prevented the deposition of silver onto other surfaces, particularly analyser 1 which, at forward scattering angles, was in close proximity of the atomic beam line. Without this system in place, vapourised silver would collect on the analyser thereby degrading its performance over time.

The inclusion of the cold trap also helped maintain a better vacuum environment inside the chamber, as was also noted for the calcium spectrometer in chapter 3. As was the case with the calcium spectrometer, 3.7, when the cold trap was started with the oven running at approximately 200°C, a significant decrease in the internal pressure was noted from low 10^{-6} mbar to about $5x10^{-7}$ mbar. This was the result of water vapour and other gases condensing on the cold plate and therefore being trapped.

6.6 Alignment

The atomic beam, incident electrons and laser beam had to intersect at a single spot, the interaction region, in the scattering plane in order for a superelastic scattering event to be registered. For this reason, it was essential to ensure that the atomic beam source, electron gun and detectors as well as the laser beam were aligned to the interaction region. Alignment of the components excluding the laser beam, was facilitated by the use of diode lasers fitted into them. The diode lasers were Roithner Lasertechnik ADL-65052TL diode lasers

at 650 nm. These lasers were made to coincide at the interaction region whilst ensuring they were propagating in the scattering plane.

A diode laser was fixed behind the electron gun which passed through the gun, the interaction region and finally the Faraday cup. A custom-made brass cylinder with the same dimensions as the oven crucible, into which a laser diode was fitted, could be inserted in the oven in place of the crucible. With the crucible removed, the alignment laser tool was slid into the boron nitride oven furnace. This laser passed through the skimmer assembly, interaction region and ultimately hit the atomic beam dump. A defining aperture was placed at the back of the tool and the exit hole in the skimmer acted as a second aperture. The analysers could each be fitted with a purpose built alignment tool, also made of brass and fitted with a 650 nm diode laser. These could be inserted at the back of the analysers after their back cover plate had been removed. A trace laser beam was located on a metal bar above the interaction region. This was fixed so that the laser beam propagated vertically downwards, orthogonally to the scattering plane. The trace laser diode was used to align the main laser beam used for the super-elastic experiments. The main beam was made to counter-propagate collinearly along the trace laser beam. In this way, it was ensured that the main laser beam travelled vertically through the interaction region, and not at an oblique angle.

The alignment procedure was carried out each time any of the components was moved, adjusted or removed from the spectrometer for maintenance purposes. The laser had to be re-aligned at the start of every experiment after it had been switched off and on again. The diode lasers were run from a single power supply unit. They could be run independently using the corresponding individual switches. To carry out the alignment procedure, the lasers were turned on and a viewing card was used to observe the propagation of the beams. Translational and height adjustments were made to the gun, analysers and oven until their respective diode laser beams coincided at a single point in the scattering plane as seen using the viewing card. This defined the interaction region. At this point, the trace laser diode above the interaction region was switched on. The main laser beam, operating at low power was then aligned to the in-

teraction region.

6.7 The Laser System

The super-elastic experiments on silver were performed using a single-mode, continuous wave Spectra Physics Dx-series dye laser [98]. The laser system was located on a laser table directly adjacent the spectrometer, which made beam delivery relatively easy, as is explained in section 6.8. The laser frequency could be adjusted so as to remain on resonance with the silver transition of interest. It was imperative that the laser remained stable at the required frequency, since the data collection process ran over several days. This was particularly true at low energies where the count rates were low.

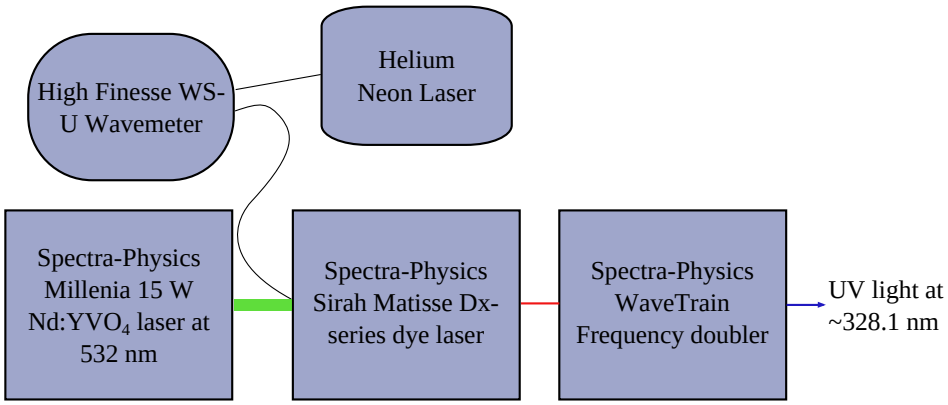

Figure 6.4: *Block diagram of the laser used for the super-elastic scattering experiments with silver atoms. The Spectra Physics Millenia 15W Nd:YVO_4 laser pumps the Dx-series dye laser. A frequency doubler was used to double the output frequency of the dye laser to produce radiation at ∼328 nm with a power of 160 mW. A High Finesse WS-U wave-meter was used to constantly monitor the frequency of the dye laser. The wave-meter was itself calibrated at 5 minutes interval. The laser frequency was thus maintained on resonance with the atomic transition for long periods of time.*

The dye laser was pumped by a diode-pumped solid state continuous wave laser, a Spectra Physics Millenia 15W Nd:YVO_4 operating at 532 nm. A schematic diagram of the dye laser is shown in figure 6.5. The green light from the solid state laser is coupled in through mirror M1 (figure 6.5) which steers and focusses the pump laser radiation into the dye jet. An external pump

and circulation system circulate the dye which passes through the laser cavity. The excited molecules of the dye fluoresce over a wide range of frequencies. A single frequency can be isolated by minimising losses at that particular frequency.

The birefringent filter (C) consisting of three quartz plates provides an initial coarse wavelength selection. It can be rotated using a stepper motor and in turn rotates the polarisations of light at wavelengths different to the selected frequency. The various Brewster angled surfaces in the laser then cause losses at these wavelengths. Further wavelength filter is provided by the thick etalon (E) and the thin etalon (F). A terbium-gallium-garnet (TGG) plate (D) acts as a Faraday rotator and in combination with the out-of plane mirror M6, form an optical diode that ensures light propagation in one direction only.

A Spectra Physics Wave-train frequency doubler was used to double the frequency of the output radiation from the dye laser in order to produce the final radiation at 328.163 nm. The design and principle of operation of the dye doubler is identical to the one used for calcium experiments and described in section 3.8.

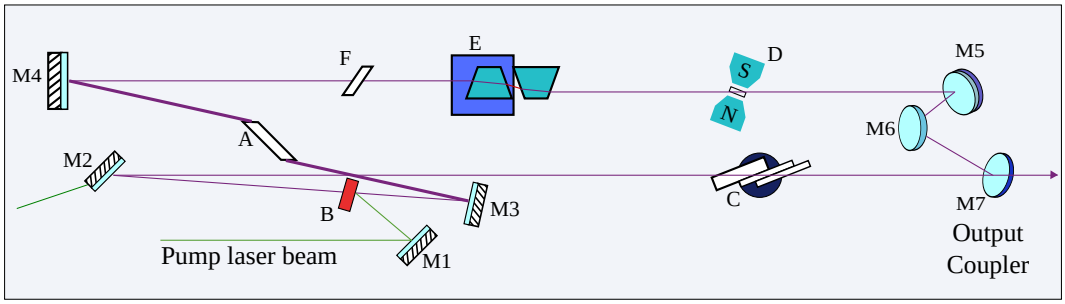

Figure 6.5: *Schematic illustration of the Matisse Dx-series dye laser showing the main optical components. (A) parallel displacement rhomb. (B) DCM dye jet. (C) motor-driven birefringent filter, consisting of three plates. (D) unidirectional device. (E) Motor-driven thick etalon. (F) Motor-driven thin etalon. (M1)- (M6) Mirrors. (M7) Output coupler.*

6.7.1 Laser Shutter

In the optical path was also located a laser shutter which was used to block and unblock the laser beam using a TTL signal. This allowed measurement of the signal count for super-elastic scattering events when the laser shutter was open and conversely the collection of background count with the laser shutter activated. The shutter is a commercially available, gravity-fed laser shutter (LS-10-12). When switched off, the laser shutter inserted a beam stop which interrupted the laser beam and prevented it from entering the vacuum chamber. With the device adequately powered the beam stop was raised letting the laser radiation through to the interaction region. A simple control unit was built to control the shutter, based on the one used for the calcium super-elastic experiments as described in chapter 3. The circuit could be controlled using the experiment computer via the main data acquisition program.

6.7.2 Laser Locking

The laser must remain stable and on resonance with the atomic transition for the entire duration of data accumulation, which could require a couple of weeks. As mentioned before, the laser was initially set to be on resonance with the transition frequency at 328.163 nm at the beginning of the experiments. However, small changes in the laboratory environment such as temperature and pressure changes may cause the laser frequency to drift. The frequency of the beam could not be allowed to change while data was being collected, otherwise it comes out of resonance with the atomic transition and the density of excited atoms changed. For this reason, it was imperative to monitor and offset any such changes. To maintain the laser at the correct frequency, the dye laser was first stabilised to about 10 KHz using intra cavity optics and electronics. The frequency of the dye laser was then controlled by a High-Finesse WS-U wave-meter to an accuracy of 1 MHz. To ensure the frequency measured by the wave-meter was accurate, it was in turn continuously calibrated every five minutes to a frequency-stabilised helium-neon laser whose absolute wavelength was set to $\sim$10 KHz.

6.8 Beam Delivery and Optical Set-up

The laser system delivered the required radiation into the vacuum chamber through a high quality fused silica CF-70 window centrally located on the bottom flange of the spectrometer. The laser radiation out of the laser assembly was at the correct wavelength, however the polarisation was not yet defined. Several optical components were needed in the optical path to collimate the beam, change its direction and control its polarisation.

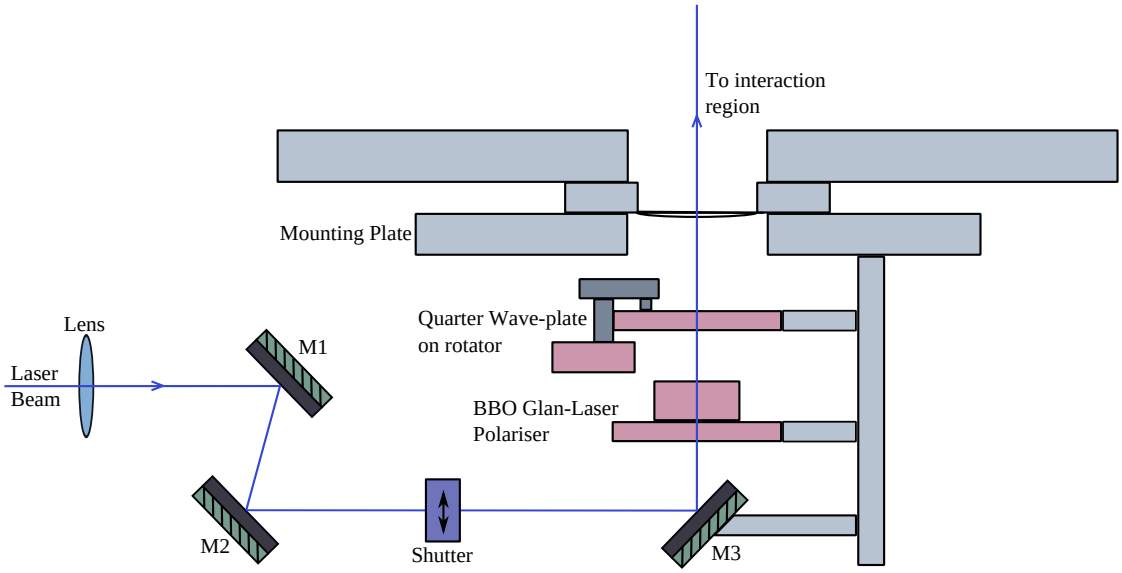

Figure 6.6: *Optical Set-up and components used to deliver the beam to the interaction region. Mirrors M1 and M2 change the path of the beam and direct it onto mirror M3 which can be used to steer the beam onto the interaction region. The Glan-Laser polariser and the quarter wave-plate were used to control the polarisation of the laser beam and produced circularly polarised light.*

The optical set-up is shown in figure 6.6. The horizontally directed laser beam exiting the doubler at 328.163 nm first passed through a 750 mm focal length lens which focussed the beam in order to produce a beam waist of about 2 mm at the interaction region. Two UV grade mirrors M1 and M2 then steered the light towards a 45° angled mirror, M3. The third mirror redirected the radiation such that it was vertical and orthogonal to the scattering plane. The beam was aligned so that it passed directly through the interaction region. A trace laser diode was used for this purpose. The laser diode was located

on a custom made metal bar approximately 15 cm above the interaction region. When it was turned on, the main laser beam was steered so that its path coincided that of the trace laser. This alignment had to be carried out with the oven at low temperatures as it was observed that the trace laser did not function properly when the oven was operating at higher temperatures.

A BBO Glan-laser polariser [121] was located after mirror M3 and was used to define the polarisation of the laser beam, thus ensuring that the beam entering the chamber was strongly polarised. The next optical component in the path of the laser radiation was a zero-order quarter wave-plate mounted on a rotator. The rotator, driven by a computer-controlled stepper motor, allowed the polarisation vector of the radiation to be altered.

6.8.1 Alignment of the Quarter Wave-plate

A quarter wave-plate was used to produce circularly polarised light [122]. It was mounted in a rotatable holder with a scale marked in degrees. This enabled a measurement of the relative rotation of the quarter wave-plate to be made. However, to obtain an absolute measurement, it was essential to establish the direction of the quarter wave-plate with respect to the experiment.

The optical axis of the quarter wave-plate was set relative to the polarisation axis. In these experiments, the polarisation axis was arbitrarily chosen to be relative to the gun axis inside the spectrometer. In order to set this, the laser radiation was retro-reflected back through the quarter wave-plate and the BBO Glan-laser polariser. A mirror was temporarily inserted in the optical path after the quarter wave-plate and a viewing card was used to detect the retro-reflected light. When the intensity of the returning beam was minimised, this indicated the quarter wave-plate was at a 45^{o} angle to the polarisation axis. A measurement of the scale reading on the rotator was taken and it was then manually rotated to detect further minima. These angles were noted for reference. A computer-controlled stepper motor was then used to rotate the quarter wave-plate in order to obtain right- and left-hand circularly polarised radiation at the interaction region.

6.8.2 Fluorescence measurement

The observation of resonance fluorescence from the excited target atoms is specially important during the preliminary procedures of the experiment. The detection of fluorescence is a direct indication of the emission of atoms from the atomic source but this can also be used to ensure the laser radiation is exactly resonant with the atomic transition. For this reason, a 50 mm diameter 75 mm focal length fused-silica lens located inside the scattering chamber was used to image the fluorescence produced by the laser-excited silver atoms onto a silicon carbide (SiC) quadrant photodiode located outside one of the windows of the vacuum chamber.

After passing through one of the four fused-silica CF-70 window on the side of the chamber, the fluorescence was imaged onto an external silicon carbide quadrant photodiode. This allowed the laser-induced excitation of the silver beam to be monitored. The photodiode was only sensitive to UV light and in spite of the surrounding visible light that was present, no band-pass wavelength filters were required. The photodiode was aligned by placing a piece of white paper directly in front of it, onto which the imaged fluorescence could be observed as it appeared as a blue spot. The position of the photodiode was then adjusted using three XYZ adjusters in order to maximise the output signal. The wavelength of the laser was then scanned until the observed fluorescence was maximum. In this manner, the fluorescence was regularly monitored to ensure that the laser wavelength was set to produce the maximum population of excited targets at the interaction region.

6.9 Conclusion

This chapter discussed the design of the spectrometer used to carry out super-elastic scattering experiments on silver. The spectrometer was originally designed for use in coincidence experiments. Most of the components had been constructed prior to this project and have been detailed in past literature [116]. The newly built high temperature effusive atomic beam source discussed previously in Chapter 5, was fitted in this spectrometer. When heated to about

1200°C, it was able to produce a beam of silver atoms. This provided the atomic target for the super-elastic process which was then irradiated with a UV laser beam. The laser system has been described. A quarter-wave plate was used to produce circularly polarised light in order to measure the ACP $L_{\perp}$. The excited atomic target was then bombarded by a fine beam of electrons of specific energy generated by an electron gun. The electrons scattered from the excited atoms as they relax to ground state were detected by two identical electron energy analysers. The next chapter will describe the procedures undertaken to collect super-elastic scattering data using the spectrometer.

Chapter 7

Super-elastic scattering results from laser-excited silver atoms

7.1 Introduction

This chapter presents super-elastic scattering data obtained for the first time from the transition metal silver. Naturally occurring silver consists of two main isotopes, ^{107}Ag and ^{107}Ag. ^{109}Ag atoms were excited from the $5^2S_{1/2}$ ground state to the $5^2P_{3/2}$ excited state using a single-mode, continuous-wave UV laser at $\sim$ 328.1 nm. A quarter wave-plate was used to produce circularly polarised light, as detailed in section 6.8. The radiation was then used to excite the silver atoms. An electron beam of well-defined energy collided with the excited atoms. After the collision these atoms were de-excited, so that the electrons gained energy. These super-elastically scattered electrons were detected as a function of scattering angle by two analysers. This process enabled the measurement of the atomic collision parameter $L_\perp$, conducted for six outgoing electron energies namely, E_{out}= 100 eV , E_{out}= 50 eV, E_{out}= 40 eV, E_{out}= 30 eV, E_{out}= 25 eV and E_{out}= 20 eV, where E_{out} is the energy of the outgoing electrons. At 20 eV, the super-elastic count rates were significantly reduced which necessitated long operation and acquisition times.

This chapter is divided into 5 parts. The preliminary procedures preceding the actual super-elastic measurements are first detailed. The methods of data acquisition and data analysis are then explained. A new computer program was

developed to fully computer control the experiment and this is also detailed in this chapter. Finally the results obtained for the measurement of the parameter $L_{\perp}$are presented.

7.2 Preliminary Procedures

This section discusses the necessary steps preceding the super-elastic data acquisition with silver. Several procedures are similar to those already described in chapter 4, but they will be reiterated for the sake of clarity and completeness.

7.2.1 Calibration of the electron gun energy

The electron gun used in this experiment is similar in design to the one used for the super-elastic experiments with calcium. As was the case previously, the energy of the electron gun also had to be calibrated. The electron gun energy had to be compared to a known feature, in order to measure the contact potential which resulted from contact between dissimilar surfaces inside the gun. This meant that there was a discrepancy between the energy of the incident electron beam and the potential that the electron gun was set to using the controlling power supply.

The incident electron energy was calibrated using the helium 2^2S resonance feature at 19.366 eV [104]. The procedure carried out was identical to the one described in section 4.2.1 and is hereby summarised. A measurement of the elastically scattered electrons from helium atoms was required as a function of incident electron energy. One of the analysers was rotated to 90°. At this scattering angle, the resonance feature is prominent and appears as a dip in the continuum spectrum. The gun voltage, V_{GUNE} was set to -19.4 eV. The analyser voltage, V_{AIRSE} was then manually adjusted until the maximum count rate from elastic scattering at 90° was detected. By simultaneously ramping V_{GUNE} and V_{AIRSE} at the same rate and in the same direction, the analyser was able to detect elastically scattered electrons of different energies. When the gun emitted electrons at the appropriate energy, the $2S_{1/2}$ resonance feature appeared in the spectrum. An offset contact potential of ∼1 eV was determined

using this procedure.

Since helium is an inert gas and does not react with silver, this procedure could be conveniently repeated whilst the super-elastic experiment was running. Typically, the electron beam energy was calibrated several times and at various stages of an experimental run. This is because silver was being used for the first time as a target at Manchester, and the behaviour of the spectrometer using this target was yet to be established. The contact potential was found to remain generally constant for a constant filament current. In contrast to the experiments with calcium, where surfaces inside the spectrometer charged up due to deposition of calcium, no such problems were observed in the case of silver. Indeed, the electron beam energy was found to be stable over extended operating times.

7.2.2 Calibration of the electron analysers

The ideal voltages for the analyser elements are dictated by their design, which sets the required voltages for the hemispheres and the pass energy using computer simulation. In practice however, there may be an offset between the calculated voltage and the actual potential of the detector, which leads to small offsets in the energy of the detected electrons. The energies of the analysers are therefore calibrated prior to measurements in order to account for these differences. This is specially important in this experiment, due to the use of two analysers. Their voltages had to be fine-tuned so that the energy of the detected electrons on both analysers were equal for a particular scattering event.

Once the electron gun had been calibrated as described in the previous section, the electron detectors were calibrated using both elastic and inelastic features. On certain occasions, the calibration of the analyser was performed immediately after the gun calibration whilst helium gas was still flowing into the vacuum chamber. The filament current was reduced typically to tens of nanoamps so as to limit the count rates to a few kilohertz at the elastic peak. This was to avoid saturation or damage of the CEM due to high count rates.

With the gun energy V_{GUNE} set to E_{inc}, the analyser residual energy, V_{A1RSE} was adjusted to $E_{sel}= E_{inc}- \varphi$ where φ is the total contact potential previously determined. The potentials of the inner hemispheres were then adjusted to maximise the observed count rate for the elastic scattering peak.

Typical voltages to the various elements of the analysers for selecting and passing electrons of energy E=25 eV are shown in Table 7.1.

Element	Analyser 1/V	Analyser 2/V
Lens	81.4	81.0
Outer Hemisphere	7.8	7.8
Inner Hemisphere	31.4	31.3
Pass energy	15.1	14.9
Deflectors X^+X^-	0.1	0.7
DeflectorsY^+Y^-	0.2	0.9

Table 7.1: *Table showing typical voltages of the components of the analysers when electrons of energy E=25 eV are being detected.*

7.2.3 Energy Loss Spectra

An important step before data acquisition was the measurement of energy loss spectra as previously described in section 4.2.1. It was essential to establish whether any super-elastic counts were being registered. By detecting scattered electrons from atoms at the interaction region, it was possible to determine whether the atomic beam oven was operating as expected. This was a particularly important step especially in the early stages of the project with silver, as the behaviour of the atomic source was yet to be fully determined. Additionally, the detection of super-elastically scattered electrons inferred information about the physical alignment of the laser, analysers and the atomic beam oven.

Generally, as a first step, it was possible to establish whether the oven was emitting silver atoms by detecting fluorescence from the laser-excited atoms. An energy loss spectrum was then taken to detect super-elastically scattered electrons from the interaction region. The super-elastic signal can be observed only when the laser radiation and atomic and electron beams overlap. At the same time, the analysers must also accurately image the scattered electrons

onto the input of the energy selectors. Thus, detection of the super-elastic signal is a rigorous test of the alignment of the system. During this process, if the count rate detected was low, the mirror M3 from figure 6.6 (page 146), was adjusted to try and maximise the scattering yield. This was performed with the analyser set to detect super-elastic events. With the gun potential at V_{GUNE} eV, the analyser energy was set to (E_{sel} + 3.778 - φ)eV. Mirror M3 was then adjusted whilst the count rate was monitored visually and audibly. Once the super-elastic signal was observed, the wavelength of the laser was locked as described in section 6.7.2. Energy loss spectra were obtained after the mirror position had been finely adjusted. This was carried out in an iterative manner till a maximum in the super-elastic yield was observed. Once a maximum count rate was achieved, measurements could be started. An example of an energy loss/gain spectrum is shown in figure 7.1. This was measured with analyser 2 at θ_e= 25° for an outgoing energy of 40 eV.

7.3 Experimental Technique

In the super-elastic measurements with silver described in this chapter, only ACP $L_\perp$ was determined. Circularly polarised light obtained using a quarter-wave plate was used to excite the silver atoms. The UV radiation coming from the laser system at 328.16 nm had a power of $\sim$ 160 mW out of the frequency doubler and before the optical mirrors, wave plate and polariser. This corresponded to a calculated intensity at the interaction region of $\sim$ 10 mW/mm^2. As described in Chapter 6, the optical axis of the quarter-wave plate was set relative to the polarisation axis (gun axis), by retro-reflecting the laser radiation through the combination of quarter-wave plate and BBO Glan-laser polariser. The intensity of the retro-reflected beam was then minimised. A stepper motor was used to control the rotation of the quarter-wave plate. The stepper motor could in turn be computer-controlled such that the rotation of the quarter-wave plate could be controlled by the computer.

The ACP $L_\perp$ was determined in the following way. The quarter-wave plate optic axis was set at 45° to the BBO Glan-laser polariser. With the analysers

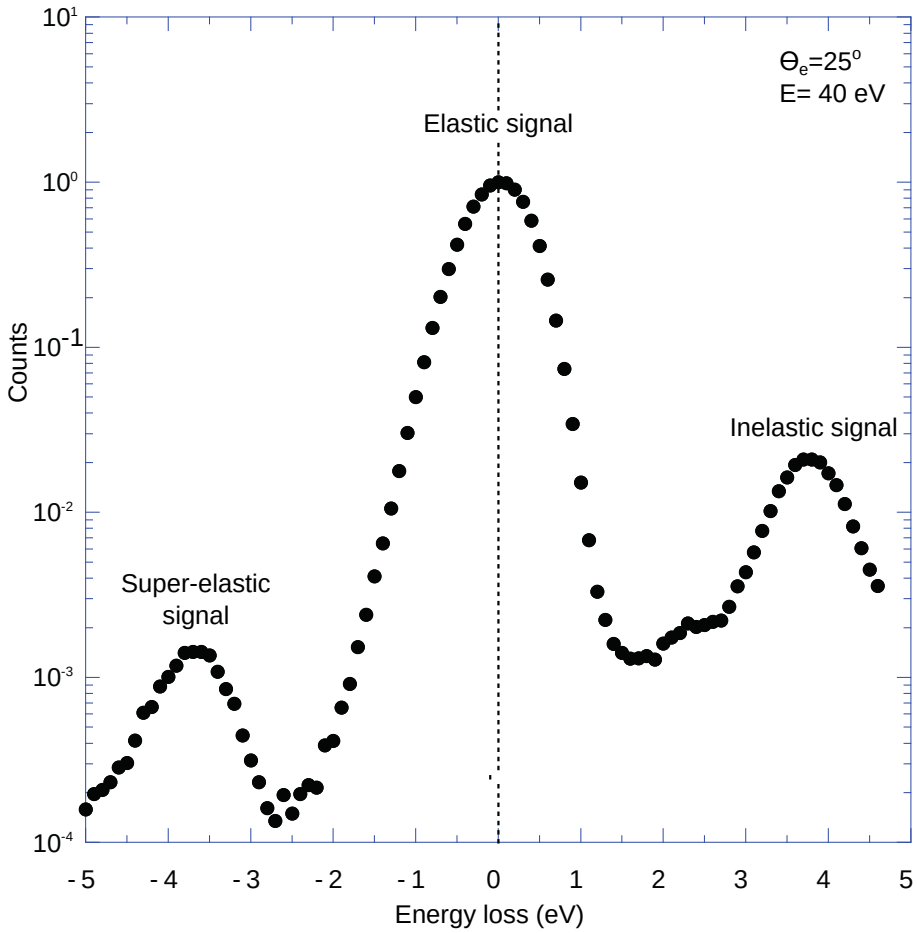

Figure 7.1: *Energy loss/gain spectrum from laser-excited silver atoms in the interaction region, plotted on a logarithmic scale and referenced to the position of the elastic peak. The elastic peak, set at zero energy loss, dominates the spectrum. The inelastic yield has a smaller peak at a positive energy loss of +3.78 eV, about 50 times smaller than the elastic peak. The super-elastic peak occurs at a negative energy loss of -3.78 eV and is about 700 times smaller than the elastic peak.*

at specific scattering angles θ_1 and θ_2 , the retardation plate was then rotated in steps of 90° through three complete rotations. This produced pure circularly polarised laser radiation of alternating handedness at every increment for a total of thirteen points. The first position of the quarter-wave plate corresponded to σ^- polarisation and thereafter, the handedness alternated such that six data sets were collected using σ^+ polarisation and seven data sets using σ^- polarisation. The count rate of super-elastically scattered electrons was then measured, at every position of the quarter-wave plate, for up to 500 seconds at each angle of the quarter-wave plate. After each signal measurement, a laser shutter was inserted in the optical path to block the laser beam so that a background count rate could be taken. This was measured for the same time interval, t as the measurement with the laser. Direct subtraction of the background count rate from the signal count produced the nett super-elastic signal at the angles θ_1 and θ_2. $L_\perp$ was then determined for each analyser angle. The analysers were then moved to new scattering angles, ${\theta_1}^{\text{new}}$ and ${\theta_2}^{\text{new}}$, and the above process repeated. Data was collected over a scattering angular range from θ_e= 20° to θ_e= 130°, every 2.5°.

Using the above method at each scattering angle, the six data points obtained using σ^+ polarisation, and seven data points collected with σ^- polarisation were used to compute an average value of count rate for each handedness. The results produced $\langle S_{\sigma^+}(\theta_e)\rangle$ and $\langle S_{\sigma^-}(\theta_e)\rangle$ respectively. From these, the angular momentum transferred to the atom $L_\perp$ was then determined from equation 7.1.

$$L_\perp = K^{circ}\left(\frac{\langle S_{\sigma^-}(\theta_e)\rangle - \langle S_{\sigma^+}(\theta_e)\rangle}{\langle S_{\sigma^-}(\theta_e)\rangle + \langle S_{\sigma^+}(\theta_e)\rangle}\right) \tag{7.1}$$

where K^{circ} is the optical pumping parameter for circularly polarised radiation. K^{circ} is expected to be close to unity, ~ 0.998 [47]. It is assumed to be equal to one in the data acquired in this project.

In these experiments, the sign of $L_\perp$ was determined following the convention usually adopted for the scattering angle, as noted by Andersen et al [123], which defines θ_e to be positive for scattering events on the right of the incident

electron path, when the scattering plane is viewed from above. In addition, $L_\perp$ is positive if the angular momentum is given by the right hand rule for the z-axis in the direction of the laser beam. In the experiments described here, the sign of $L_\perp$ calculated for analyser 1 was reversed to follow the conventions.

The data acquisition process was computer-controlled and the program used will be discussed in the next section.

7.3.1 Data Acquisition Software

The super-elastic scattering experiment from silver was run using a dedicated computer program. The computer controlled the operation of the spectrometer. This was achieved by using a data acquisition (DAQ) card which was able to pass signals from the spectrometer to the computer.

The DAQ card used in this project was a National Instruments PCI-6221 [124]. The DAQ card was located inside the controlling computer and an input/output connector block from the card made the necessary connections from the various instruments of the spectrometer to the controlling computer. Using such a card, digital and analogue signals from the experiment could be acquired by the computer.

A main computer program was written in LabVIEW [124] to assist in data acquisition. The user interface of this program, `FullProgram.vi` is shown in figure 7.2. The data acquisition program eliminated the need for manual intervention for so long as a scan was ongoing after having commenced. This was particularly useful for data collection at lower energies where the count rate decreased substantially and longer running times were required. To increase efficiency, the experiment could be run overnight using the operating computer. The program performed several tasks which were required to automatically collect super-elastic scattering data. This was achieved by using a number of sub programs, known as `sub vi`'s in the software terminology, that performed individual tasks. For example, one such `sub vi`, `stepperctl.vi` controlled the motion of the stepper motor using user-defined parameters. This had previously

been written by Alex Knight Percival at Manchester [84]. The program could be run on its own when it was desired to rotate the quarter-wave plate when measurement was not ongoing. When the main program was run, it called on the `sub vi` to rotate the quarter-wave plate. Likewise, the program called on several other `sub vi`'s to carry out specific individual tasks.

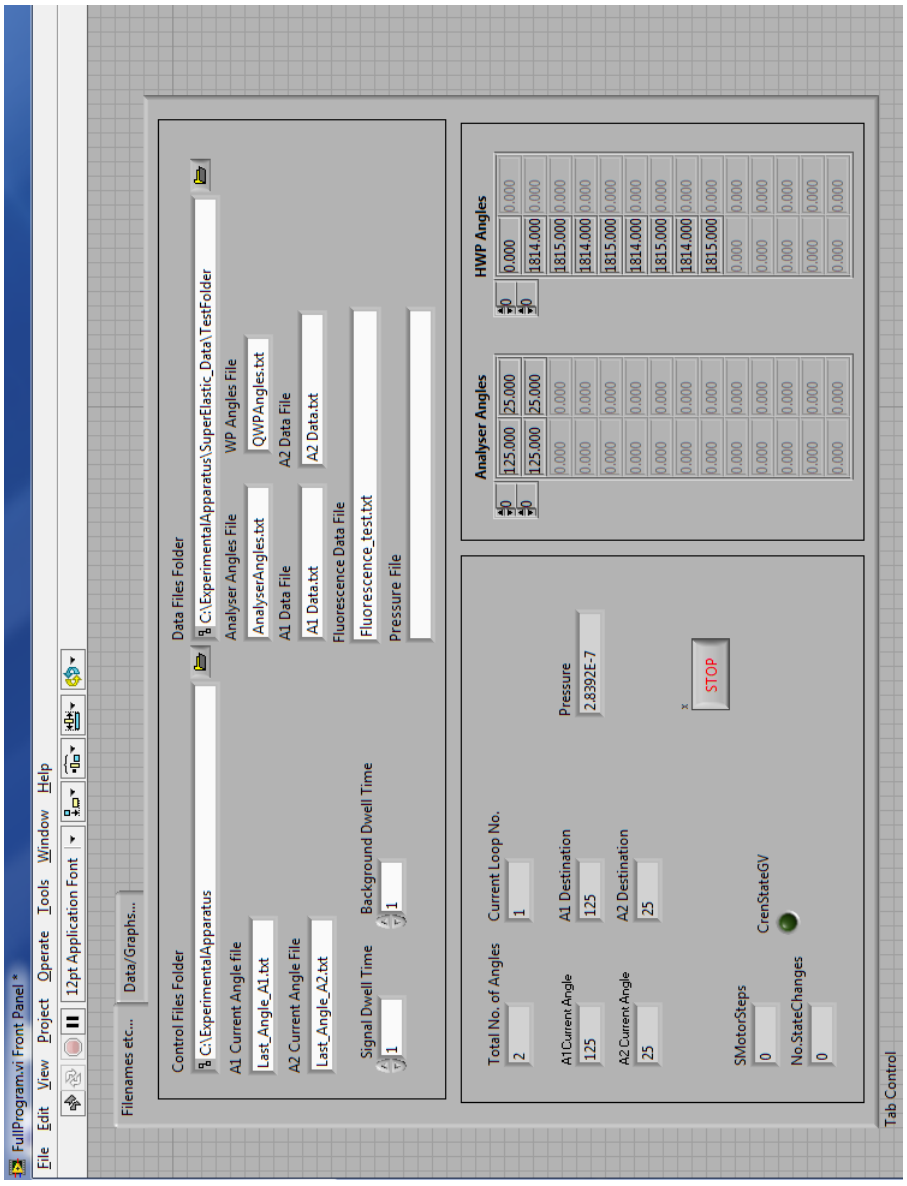

Figure 7.2: *Snapshot of interface of main program. Details are in the text.*

The interface to the main program, or *front panel* as shown in figure 7.2 enabled the user to enter the necessary parameters before a scan. These are shown in order of appearance, from left to right, in table 7.2.

Label	Description
Control files folder	User entered folder where all necessary input files were saved and output files generated by the program stored.
A1 current angle file	Text file where the current position of analyser 1 (at the start of the run) was entered and saved by the operator.
A2 current angle file	Equivalent to above but for analyser 2.
Signal Dwell time	Specified time in seconds for which the count rate was to be accumulated whilst the laser is exciting the silver atoms.
Background Dwell time	Specified time in seconds during which the background count rate was taken with the laser shutter blocking the laser beam.
Total No. of angles	Number of analyser angles listed for which data would be collected. Each angle corresponds to one *scan*.
Current loop number	Current order number in the list of analyser angles. Corresponds to the nth ongoing scan.
A1 current Angle	Indicator displaying the current angular position of analyser 1.
A2 current Angle	Indicator displaying the current angular position of analyser 2.
A1 destination	Angular position that analyser 1 moved to for the next scan, from its current angle.
A2 destination	Angular position that analyser 2 moved to for the next scan, from its current angle.
S Motor Steps	Indicator verifying the motion of the quarter-wave plate.
No. of state changes	Indicators showing the motion of the analysers.
Cren. State GV	Same as above.
Data Files Folder	Folder where data files were located.
Analyser Angles File	Text file containing two lists of angles to which the analysers would be moved to.
WP Angles File	List of angles at 90º interval through which the wave-plate was rotated
A1 Data File	Destination file for data from analyser 1.
A2 data File	Destination file for data from analyser 2
Fluorescence file	File that stored measurement of the fluorescence at the interaction region.
Pressure file	Optional file that stored measurement of the pressure at regular time intervals.

Table 7.2: *Description of the various parameters of the main data acquisition program.*

Before any measurement could be started, it was ensured that the laser was resonant with the atomic transition. In this case, the wavelength had to be set to 328.16 nm. The laser alignment was then fine tuned by maximising the super-elastic scattering count rates from the two analysers. The alignment was adjusted using mirror M3 as shown in figure 6.6 on page 146. Once the count rate had been maximised, the data collection process could be started.

The above mentioned `FullProgram.vi` program was used for the purpose. The program could only be started after the input parameters shown in table 7.2 had been entered. The necessary text files were also written or modified and saved in the specified folder. The quarter-wave plate was first set to the starting position. This corresponded to the rotation angle of the quarter-wave plate which aligned its polarisation vector with the gun axis. This was a previously determined angle.

When data had to be collected, the quarter-wave plate was first set to the starting position. The necessary parameters which included the time for which signal would be collected, had to be entered in the main program. Referring to figure 7.2, the dwell time is in fact the user-specified duration for which count rates were collected. The current file folder was entered which contained the files that populated the analyser angles contained in the `AnalyserAngles` file in the example shown, as well as quarter-wave plate angles found in the `WPAngles.txt` file. These files had to be located in the specified folder for the program to run successfully.

The program was then started and proceeded in the following sequence. The analysers were moved from their current angle to the first specified angle in the file `Analyser Angles`. The analysers 1 and 2 were set to θ_1 and θ_2 respectively. The signal count S was measured for the duration `Signal dwell time` in seconds. These counts were recorded as the first column of the analyser data files. The computer-controlled laser shutter was then introduced into the path of the laser beam and the background count, B was taken for `Background dwell time` seconds. These background counts were entered into the data files as the second column. The subtraction of B from S constituted one data point. The

quarter-wave plate was then moved to the next rotation angle corresponding to the first entry line in the file `WP Angles File`. The signal S′ and background B′ counts were taken; this constituted the second data point, with polarisation of opposite handedness to the first point. This was repeated for a total number as specified by the number of angles listed in the files `WP Angles`. In this case, this totalled 13. The thirteen data points thus obtained constituted one scan. The analysers were then moved to a new set of angles $\theta_1{}'$ and $\theta_2{}'$, corresponding to the second row of angles entered in the file `Analyser Angles`.

As the data collection proceeded, the data points were output and saved in the specified files. Data from analyser 1 was saved in `A1 Data File` and that from analyser 2 in `A2 Data File`. The program also stored measurements of the fluorescence from the laser-excited atoms at the interaction region. The measurement in volts was taken from the quadrant photodiode at regular time intervals, as specified by the operator. The fluorescence data provided a direct check of the proper operation of the laser shutter. When the laser shutter was activated and was blocking the laser beam, the fluorescence would be at its minimum value. Thus, at any point in time, the fluorescence measurement could be verified to indicate whether the shutter was working properly. The fluorescence measurement also provided an indication of whether the atomic beam oven was emitting as expected. Should the oven fail for instance as a result of the output nozzle being blocked, or if the oven was running out of the silver, this would be indicated by an obvious decrease in fluorescence.

Additionally, a measurement of the internal pressure of the chamber was also recorded. at user-specified time intervals. The measurement of the internal pressure was useful in controlling the stability of the cold trap. Furthermore, it was observed that the pressure would increase if the temperature of the oven had been increased as required for the experiments and any subsequent outgassing could reduce the quality of the data. This could be assessed by monitoring the pressure inside the chamber.

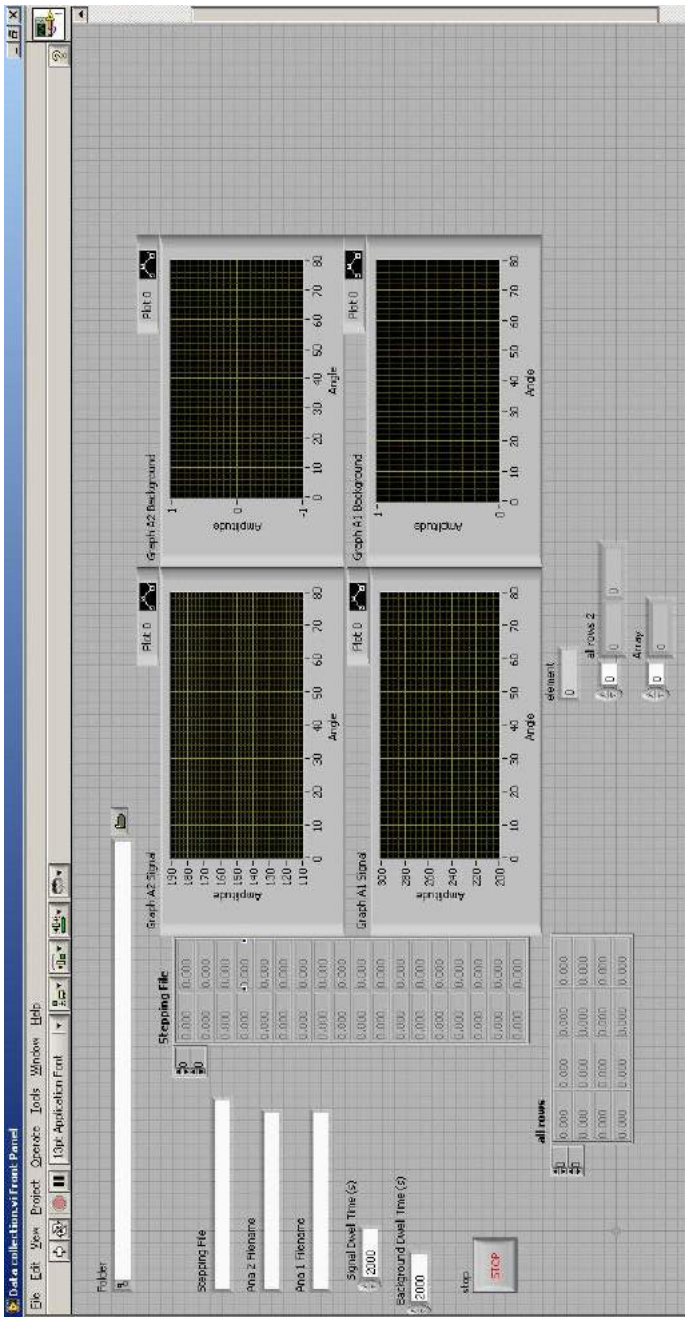

Figure 7.3: *The* `datacollection.vi` *program which displayed graphs of the signal and background counts from the analysers as they were being recorded.*

The `Datacollection.vi` program was particularly useful in determining trends in the data or mistakes that could arise for several reasons, for example, if the laser shutter had been left out after an alignment process, the background count rate would be similar to the raw signal count rate and such a mistake would be obvious on the graphical output of the data collection software.

7.3.2 Data Analysis Software

An online analysis software, `SEDataAnalysis_new.vi` was developed to automatically analyse any set of data and produce a value of the ACP $L_{\perp}$. The program was written in LabVIEW [124]. Although the analysis could be achieved manually, this program was quicker to process the large number of data sets generated by repeated measurements. The software also provided an easy way of calculating as well as displaying the results graphically. It could be run whenever the quality of a data set had to be established in order to determine whether repeated measurements were required.

Using `SEDataAnalysis_new.vi`, the files containing the data sets from the two analysers could be separately loaded. A third file containing a list of the angles of the quarter-wave plate for which measurements were taken, also had to be input by the user. The program then computed the value of P3 at each angle and saved the results as a list in an output file (P3.txt in the example shown in figure 7.4). In addition, the program also displayed graphs of signal against background count rate as a function of the quarter-wave plate angle. This provided a visual aid in determining the quality of the data. This could be carried out while the measurement process was going on.

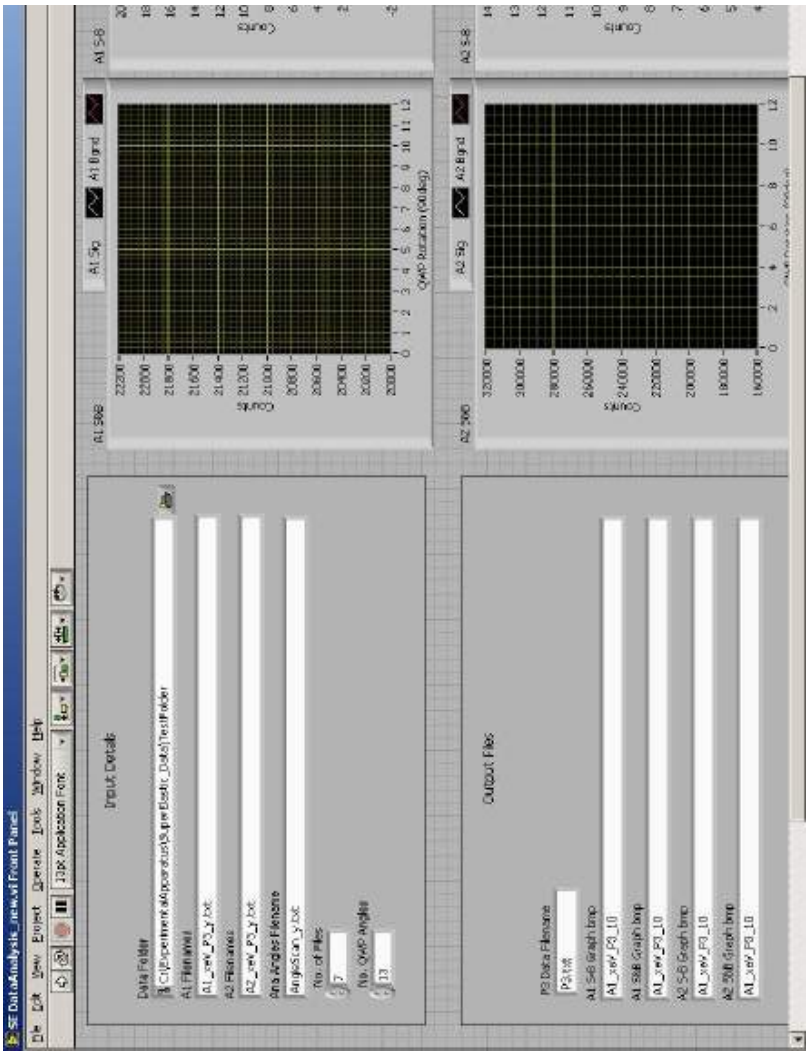

Figure 7.4: *The* `SEDataAnalysis_new.vi` *which was used to analyse the super-elastic scattering data from silver.*

7.4 Experimental results

Figure 7.5 presents the experimental results for $L_\perp$ calculated at six equivalent energies. The equivalent energy is defined as the energy of the incident electron beam in a conventional coincidence experiment. In this case, they corresponded to the energy of the outgoing electron in the super-elastic experiments.

The data shown here are for six outgoing energies between 20 eV and 100 eV. The first data set was taken at 40 eV, where the count rates are high and data acquisition times low. The data was collected over this range of energies to be able to assess the dependence of the ACP on scattering angles as well as on energy. From conservation of angular momentum, $L_\perp$=0 at θ_e=0^o and θ_e=180^o. Additionally, the value of $L_\perp$ is restricted to lie between -1 and +1, according to equation 7.1. These limits and the zero points are also included on the graphs.

From this data, $L_\perp$ is seen to evolve significantly with energy. Starting at higher energies, the changes in the value of $L_\perp$ are sharp and well-defined. As the energy decreases, more features appear, such as the appearance of an additional dip at E_{out}=30 eV. At 100 eV, $L_\perp$ rises quickly from zero at θ_e=0^o to $\sim$ 0.8 at θ_e= 20^o, which is the smallest angle for which super-elastic scattering was measured. $L_\perp$ then decreases sharply to $\sim$-0.1 at θ_e= 40^o which is a minimum point, from which $L_\perp$ rises again to a value of -0.93 at θ_e= 75^o, crossing zero again at $\sim$ 60^o. Above θ_e= 75^o, $L_\perp$ increases again slowly to reach $\sim$-0.6.

Similar features can be observed at 50 eV but thy occur at higher scattering angles. From $L_\perp$=0 at θ_e= 0^o, $L_\perp$ is seen to increase sharply to just under unity at the maximum point at θ_e= 30^o. After a sharp decrease to a dip at θ_e= 60^o where $L_\perp \simeq$-0.25, $L_\perp$ then increases again sharply to $\sim$ 1 at θ_e= 80^o, a peak which can be likened to the one seen at θ_e= 75^o for E_{out}=100 eV. $L_\perp$ then decreases to a second minimum at a value of $\sim$ -0.77 from where it rises only slowly to $\sim$-0.65.

The same trend continues at E_{out}= 40 eV with the obvious deepening of the

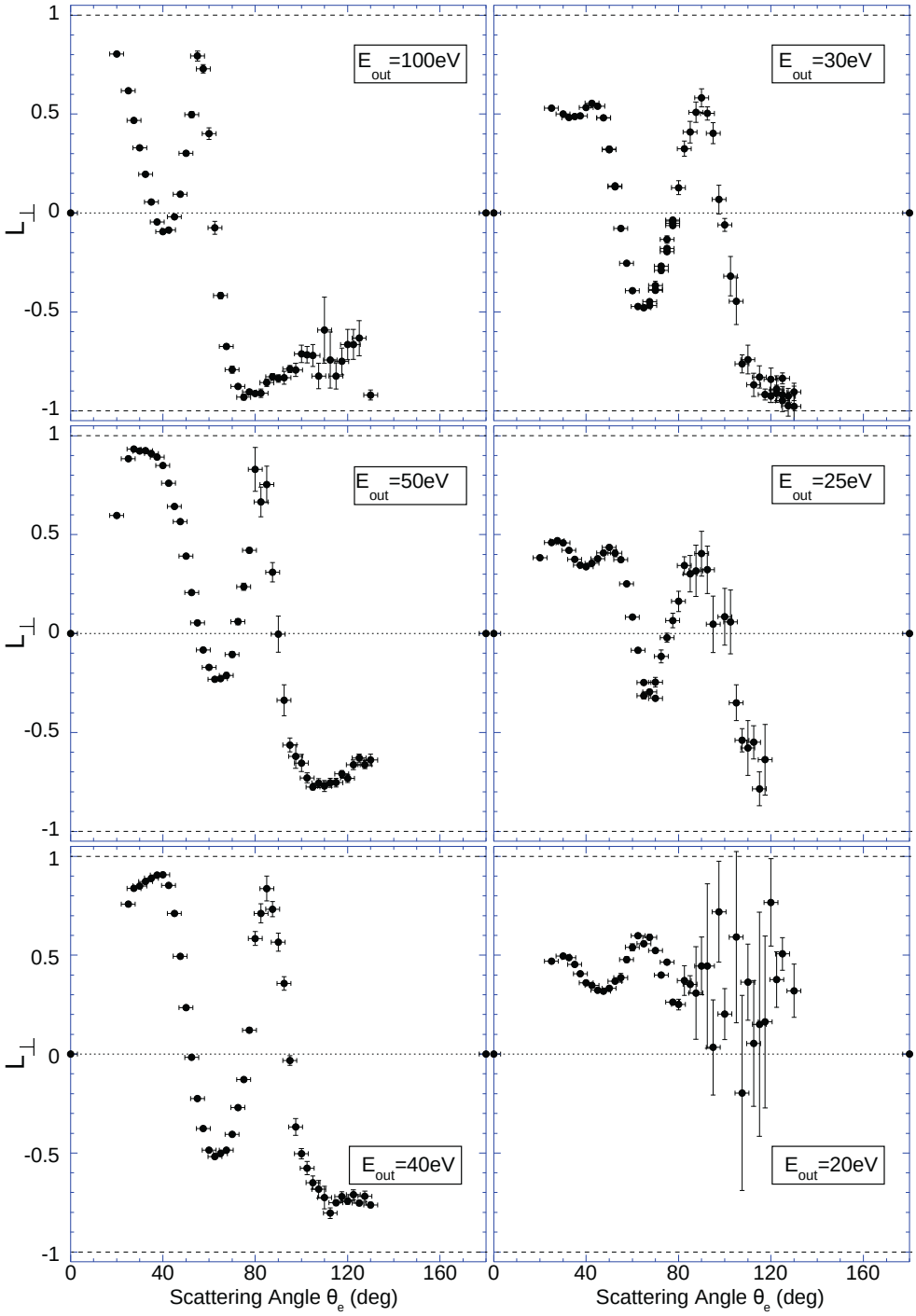

Figure 7.5: *Measurements of the ACP $L_\perp$, calculated from the super-elastic scattering data taken at the energies and scattering angles shown.*

trough between the first and second peaks. Two maxima can again be distinguished at E_{out}= 40 eV. $L_\perp$ rises rapidly from 0 at θ_e= 0°, to a first peak at ∼ 0.9 and then decreases quickly, crossing zero at ∼ 50° to reach a maximum at ∼ 60° where $L_\perp$= -0.52. $L_\perp$ increases again rapidly to just below 0.9 at ∼85° and decreases again to ∼ -0.75. At higher scattering angles, $L_\perp$ remains constant at around -0.75.

At E_{out}=30 eV, the first peak at low scattering angle evolves into two peaks with a shallow trough at θ_e ∼ 32.5°. This peak at forward scattering angle deepens as the energy decreases from 30 eV to 20 eV, whereas the main minimum feature initially observed between the two peaks at low scattering angles decreases in magnitude. This is in contrast to the pattern observed from E_{out}= 100 eV to E_{out}= 40 eV where the minimum grew deeper. Meanwhile, the peak observed at θ_e≈ 55° for E_{out}=100 eV moves to higher scatterings angles with decreasing energy. At 30 eV, the minimum previously observed at higher scattering angles, namely at θ_e∼ 75° at 100 eV, can no longer be distinguished.

This evolution noted in the main peaks and troughs carries on as the energy decreases further. At E_{out}=25 eV, there are now two forward peaks at θ_e ∼30° and θ_e ∼55°. The highest value of $L_\perp$ is now only less than 0.5 and the largest minimum is considerably shallower. There is no distinguishable dip at higher scattering angles as was previously observed at higher energy.

At E_{out}=20 eV, the trend observed at low scattering angles from E_{out}=30 eV to E_{out}= 25 eV is further confirmed, however the poor statistical accuracy beyond θ_e∼ 90° implies no reliable conclusion can be drawn about the data in this region. The data at 20 eV have noticeably less precision at higher scattering angles as a result of the high background count rates at this energy. Due to the poor signal to noise ratio, the data acquisition times were considerably extended but despite several repeated measurements, the statistics at higher angle remained poor. This decrease in signal to noise ratio meant that a larger number of data sets had to be acquired from the spectrometer whilst the stability of the whole apparatus including the laser system and atomic oven, had to be maintained for a longer time than that which was called for in previous

studies. For this reason and since data had already been taken over a wide range of energies, no further data was collected at energies lower than 20 eV.

From the graphs shown, it can be concluded that the orientation of the $4d^{10}5P^2P_{3/2}$ excited state changes rapidly as a function of scattering angles. This is true for all the energies investigated. Furthermore, the evolution of the state with energy has also been noted. At the time of writing, the only available calculations of the ACP $L_\perp$ at these energies were those made using a convergent close coupling method. These were kindly provided by Professor Igor Bray and colleagues from Curtin University in Australia [69].

A comparison of the CCC theory with the experimental results is provided in figure 7.6.

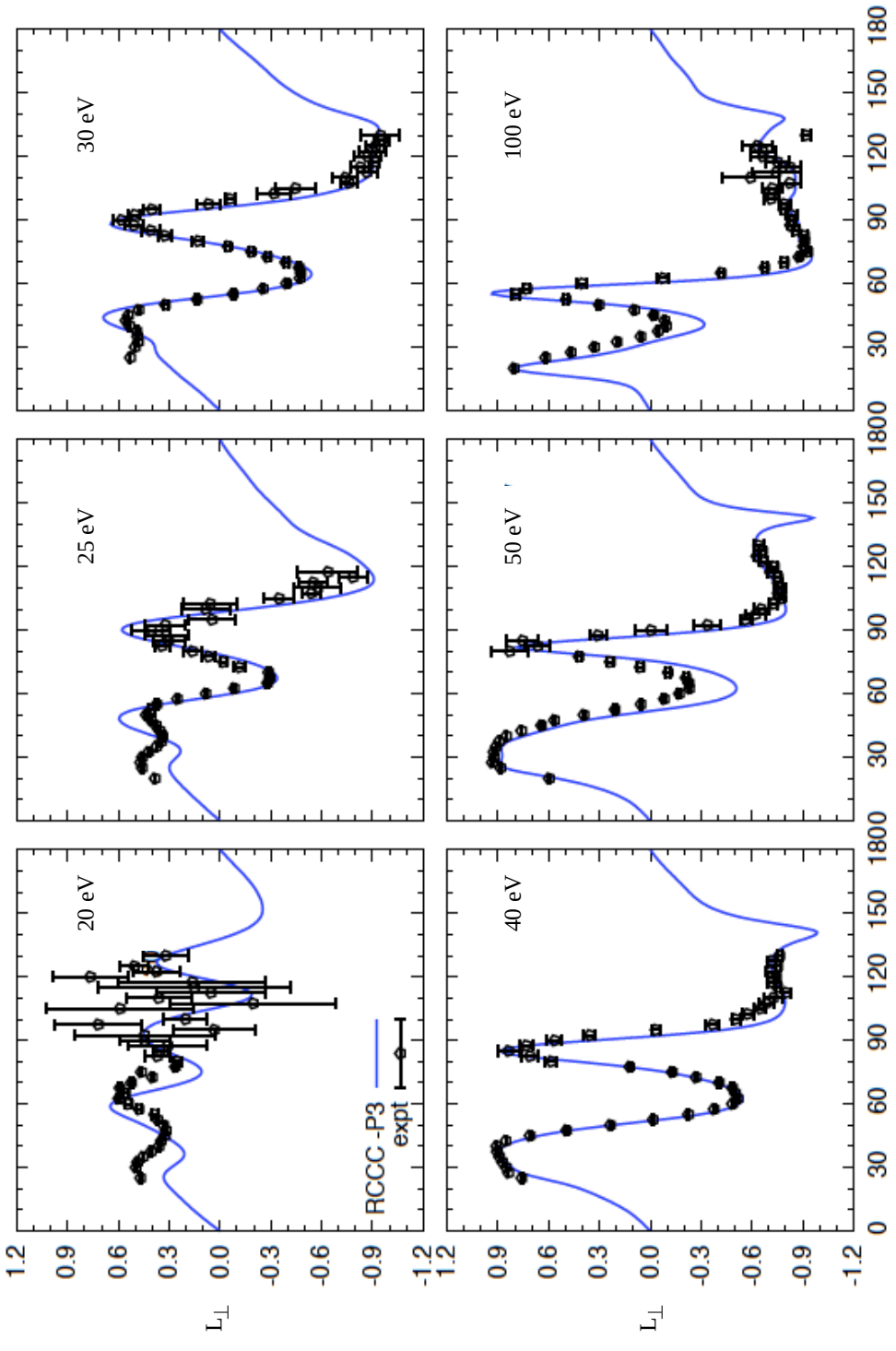

Figure 7.6: *Graphs showing the measurement of the ACP $L_\perp$ at 20, 25, 30, 40 50, and 100 eV compared with CCC calculations at the corresponding energies.*

Overall, good agreement is obtained between the CCC calculations and the experimental results, with the theory predicting most of the features especially at higher energies. The significant evolution of the parameter $L_\perp$ observed as a result of electron energy changes as observed with the experimental data, is well reproduced by the theory.

At 100 eV, the first minimum occurring at $\theta_e \simeq 40^o$, is reproduced by theory however the magnitude of the dip is greater than that obtained experimentally. Excellent agreement is seen from $\theta_e \simeq 50^o$ with theory predicting the correct magnitude and position of the features until $\theta_e \simeq 110^o$. For $110^o < \theta_e < 130^o$, only fair agreement can be observed. In this range, this can be explained by the bigger statistical uncertainties in the experimental data.

All the features observed experimentally are confirmed by theory for E_{out}=50 eV. However, as was the case with data at E_{out}=100 eV, the magnitude of the first minimum at $\theta_e \approx 60^o$ is bigger according to theory. Excellent agreement between calculations and experiment is seen from $\theta_e \approx 80^o$ onwards. In contrast to what was observed at E_{out}=100 eV, data at higher scattering angles are well reproduced by the CCC calculations displaying good agreement up to θ_e=130^o, the highest angle for which data was collected. The slow rise in the value of $L_\perp$ from $\theta_e \approx 100^o$ is well reproduced by theory. At E_{out}= 40 eV, the theoretical predictions exactly match the experimental data for θ_e=20^o to θ_e=90^o, reproducing the exact angular position and magnitudes of the features. Agreement between theory and experiment is less good at higher angles but the third maximum which only appears as a small bump in the experimental data is nonetheless well reproduced by the CCC calculation.

The theoretical calculations at 30 eV also predict well the experimental data, as can be seen from figure 7.6. Best agreement is observed from $\theta_e \approx 50^o$ to $\theta_e \approx 90^o$. For $\theta_e < 50^o$, a sharper peak is predicted by theory at $\theta_e \approx 45^o$, which appears smaller and broader in the experimental data. The angular shift towards higher scattering angles in the sharp peak observed at $\theta_e \approx 55^o$ for E_{out}= 100 eV, is well predicted by theory. The evolution of the one peak into two shallower maxima with a trough, as seen experimentally, is not reproduced

by theory. There is no distinguishable dip at higher scattering angles and this is confirmed by the calculations.

The evolution of the peak at smaller scattering angles into two peaks at E_{out}=25 eV, is also predicted by the CCC theory however the peaks appear less symmetrical according to the theoretical calculations, producing an over-estimate of the magnitude of the first of the two peaks and an underestimate of the second. There is also a slight misalignment of the angular positions of the theory with respect to the experimental results.

The agreement between theory and experimental data at E_{out}=30^o is least satisfactory. From θ_e= 90^o, this may be attributed to the poor quality of the experimental data which resulted from the poor signal to noise ratio at this energy. The theoretical calculations predict two peaks in the region 90^o<θ_e< 130^o which have not been measured experimentally. The feature with two peaks at smaller angles, seen experimentally at $\theta_e\sim$ 30^o and $\theta_e\sim$ 65^o are calculated theoretically to be at $\theta_e\sim$ 25^o and $\theta_e\sim$ 60^o respectively. The magnitude of the second of the two peaks at these small angles, as predicted by the CCC model, matches the experimental value but poor agreement between the magnitudes can be seen in the case of the first peak at $\theta_e\sim$ 30^o.

One of the principal motivations behind this project was the investigation of the influence of the d-electrons in silver on the dynamics of the scattering process. It is yet to be established whether the same models used for calcium will be able to accurately predict the experimental results obtained here even though these models have proven successful in predicting the ACPs for alkali and alkali-earth metals. It is hoped that in the near future, calculations from other theoretical models will be published and a subsequent comparison with the data here obtained may provide insight into the influence of the d-electrons when transition metals are used as targets in collision experiments.

7.5 Conclusion

In this chapter, the data acquisition process for super-elastic experiments scattering with silver has been discussed. The preliminary procedures which are very similar to the ones undertaken with calcium as a target have been briefly mentioned. The initial energy loss spectra measurements, which are necessary to determine whether the spectrometer was ready for super-elastic measurements, have also been outlined. The experimental results for super-elastic scattering from excited silver atoms at equivalent energies of 20, 25, 30, 40, 50 and 100 eV have been presented. The ACP $L_{\perp}$ was extracted from the data and has been shown in graphs at all energies. Theoretical calculations from a CCC model, by Professor Igor Bray [69] were compared to the experimental data and good agreement was observed especially in the intermediate to high energy regimes.

It has been outlined that the poor signal to noise ratio in the low energy regime especially at 20 eV made experimental measurements more challenging and in spite of several repeated data sets, the poor statistical accuracy did not allow reliable conclusions to be drawn about the data obtained at higher scattering angles.

Chapter 8

Conclusion

8.1 Summary

This thesis has presented the research that has been undertaken to investigate super-elastic scattering from laser-excited calcium and silver atoms. The work has been divided into two distinct parts, each relating to one individual target. A description of the various aspects involved towards the achievement of the two separate projects has been provided.

Chapter 1 introduced electron atom collisions in general and provided a review of the work in the field which has stimulated this project. Additionally, it presented the case for the present work. On one hand, the experimental study on calcium adds to a series of super-elastic scattering already conducted at Manchester. Previous experiments had focussed on energies ranging from 17 eV to 65 eV. The work presented here was the first attempt to acquire super-elastic data at lower energies for calcium.

A thorough comparison of earlier studies with contemporary theoretical models had revealed the fact that agreement between experiment and theory is poor at lower energies. It was therefore deemed necessary to conduct experiment in the lower energy regime to acquire accurate data that can provide a stringent test of various models. Similarly, the interest in silver as a scattering target arises from the need for additional comparison between experimental data and theory for a wider range of targets. Silver is a transition metal with

D-shell structure and the study carried out here provides the first super-elastic data for such atoms. It was also the first such study to be carried out using UV CW laser radiation.

Chapter 2 described the theoretical background of electron-atom collisions. The density matrix formalism was introduced to describe the excited atomic system. It was shown that calcium can be regarded as a two-level system which significantly simplifies the theoretical treatment. The elements of the density matrix were related to alignment and orientation parameters for the case of an S-P transition. This approach was possible based on the equivalence of the electron-photon coincidence and the super-elastic scattering processes.

In the second part of the chapter, the QED model of laser-atom interaction model was invoked. The general equations of motion that can be derived using the model, were employed to determine the time evolution of the two-level system in calcium.

In the final part of chapter 2, the implications of optical pumping processes in the interaction of silver atoms with the laser field was briefly discussed. For the purpose of this project, the relevant optical parameter, K' is equal to unity.

Chapter 3 was devoted to a description of the experimental apparatus used in the super-elastic study of calcium. The experiments were carried out inside an evacuated chamber with internal pressure of $3\text{x}10^{-7}$ mbar which housed the main parts of the spectrometer. A resistively heated atomic oven operating at $\sim$800^{o}C provided a well-collimated beam of calcium atoms. A single-mode CW laser beam at 423.3 nm excited the target atoms at the interaction region, which were then collisionally de-excited by electrons of well-defined energy generated by an electron gun. Scattered electrons were detected by an electron analyser able to discriminate electrons with respect to energy and angle. A gas jet inside the chamber provided a means of delivering gaseous targets such as argon in the interaction region. These were used for calibration and diagnostic purposes.

The optical set up that was needed to deliver the laser beam from the laser

system to the interaction region was located outside the chamber. Mirrors were used to steer the light which was directed onto a number of optical elements including a half-wave plate, optional quarter-wave plate and polariser that modified the polarisation of the laser light as required for the super-elastic experiments. The laser frequency was stabilised using a locking system based on the observation of the laser induced fluorescence at the interaction region, by means of a quadrant photodiode.

Chapter 4 describes the processes involved in the preparation of the spectrometer to be ready for data collection. This involved calibration of the gun energy, determining the exact frequency at which the laser beam was resonant with the atomic transition in calcium and taking preliminary energy loss/gain spectra in order to maximise the super-elastic signal.

The data collection process was automated and the programmes used for this purpose are mentioned. A detailed description was provided in past quoted literature. In the final part of this chapter, the results obtained from the super-elastic study of calcium at 10 eV and 12 eV equivalent energies were presented. The ACPs P_{lin}, $L_{\perp}$ and γ were calculated from the obtained data. These have been compared to predictions calculated at these energies using four state of the art theories. The CCC model calculations were in best agreement with the experimental data. It was observed that the data at 12 eV showed improved agreement with theoretical calculations at 10 eV. It was hence postulated that a $\approx$2eV shift in the nominal energy may have been introduced as a result of variation of the contact potential of the gun, which therefore implies that the incident electron energy was not as recorded. This hypothesis was confirmed when the data at 10 eV was in turn compared to CCC calculations at 8 eV. This comparison showed good agreement and indicated the 2 eV offset had been accounted for.

In order to investigate silver using the super-elastic technique, a new high temperature oven was needed that could vaporise the metal and deliver it in a controlled, well-collimated beam. The design and construction of this oven have been discussed in chapter 5. The challenge of building this oven extended

beyond the need for it to operate at high temperatures. Further requirements that were met include the need for the oven to be inert and non-magnetic. These problems and their corresponding solutions were addressed in this chapter.

As a result of the above mentioned criteria, the materials used for construction had to be carefully chosen as well as the method of heating the oven. The oven consisted of a cylindrical crucible containing a sample of the target, 80 mm long made from high density graphite with a 10 mm long nozzle at the front which quasi-collimated the atomic vapour as it exited the crucible. A furnace constructed from boron nitride surrounded the crucible. Six radially equidistant holes in the boron nitride housed six individual heater elements made from 300 mm length of 0.125 mm thick tungsten wire wound around a thin Al_2O_3 ceramic tube. The winding was in a double spiral around the tube in order to reduce the effects of magnetic fields created by the currents which were passed through the wires to heat them up. The heat was conducted to the crucible and this caused the silver sample to melt and vaporise.

Heat losses were minimised by the inclusion of cylindrical heat shields around the furnace as well as custom-designed thin metal discs in front of and behind the furnace. An oxygen-free cylindrical copper jacket surrounded the oven assembly. Copper tubing was wound along grooves in the copper jacket, through which cold water was passed to reduce the heat transmitted to other components of the spectrometer. The temperature of the jacket could be monitored using a thermocouple attached to it. With the oven at full operating temperature of $\sim$1200^{o}C the jacket only reached $\sim$150^{o}C. The oven was tested in a separate evacuated test chamber before being installed in the main spectrometer used for the super-elastic experiments where the final tests of its operation were conducted.

Chapter 6 presented the set up of the apparatus used for the experiments with silver. The experiments were conducted in an existing spectrometer that was modified to allow the super-elastic studies to be conducted. The experimental apparatus is similar to that of calcium. This spectrometer however

housed two analysers instead of one as it was initially designed and assembled for use in (e,2e) experiments. The high temperature atomic beam oven, the electron gun and two analysers were arranged in a crossed-beam configuration in the scattering plane.

Light from a frequency-doubled CW dye laser doubled at 328.16 nm excited the ^{107}Ag isotope atoms from the $5^2S_{1/2}$ ground state to the $5^2P_{3/2}$ excited state. The laser system and optical configuration are described in this chapter. Electrons from an electron gun similar to the one described in chapter 3, were directed to the interaction region. Collision of the electrons with the excited target caused the atoms to relax to the ground state. The super-elastically scattered electrons were detected by the two analysers, as a function of scattering angle and laser polarisation.

The results obtained from the super-elastic study of silver are presented in chapter 7. Before super-elastic data collection could commence, a number of preliminary procedures had to be carried out to ensure all components of the spectrometer were running properly and the super-elastic signal was measurable. The gun energy was calibrated against the known and reproducible 19.366 eV elastic resonance feature of helium, the gas being introduced into the chamber via the gas jet. Energy loss spectra were taken in order to identify the inelastic and elastic peaks in silver confirming that the oven was emitting a collimated beam of atoms. The laser was then switched on and the induced fluorescence was maximised by adjusting the mirror used to steer the laser light onto the interaction region. The laser frequency was maintained at resonance with the atomic transition by continuously monitoring the frequency using a wave-meter, calibrated using a He-Ne laser. It was crucial to maintain the stability of the laser due to the long accumulation times required for data collection especially at lower energies where the signal to noise ratio was degraded.

The steps involved in the super-elastic data acquisition are elaborated in this chapter. Herein are also described the computer programs written and used to control the spectrometer and to automate the data collection process. Data was collected for the first time for the electron-impact excitation of silver

using circularly polarised light. The ACP $L_{\perp}$ was determined from the data over the angular range of 20° to 130° for outgoing electron energies of 20, 25, 30, 40, 50 and 100 eV. At the time of writing, theoretical calculations using a CCC model were obtained from unpublished work by Professor Igor Bray at Curtin University in Western Australia. These were compared to the experimental data and good agreement was found.

It is expected that calculations for the scattering process using other models will be performed in the near future. The experimental data will be able to provide a thorough test for all the models across a relatively extended energy range (20 eV- 100 eV). This will provide an excellent test of the different models to ascertain their accuracy.

8.2 Directions for future work

This project concluded with super-elastic scattering data from silver. The oven designed and constructed was intended for use also with copper and gold. It is proposed that these targets may be investigated with the existing spectrometer. To date, there is no super-elastic scattering data from either copper or gold. One problem encountered whilst operating the oven was that the tungsten heating wires would fail, requiring replacement. This could be the result of either the wires burning out at weak spots or the spot welded end of the wire coming off. In such cases, even though it was possible to maintain the temperature by increasing the current through the remaining heaters, the resulting load on these would be higher in turn increasing the risk of more heaters failing in an avalanche effect.

In order to be able to vaporise copper and gold, a higher working temperature is required as was discussed in chapter 3. One way to be able to achieve high temperature stably would be to increase the number of heater elements. This would require modification of the existing oven or construction of a new oven based on the same design. It is proposed that the number of heaters be increased to eight in total rather than six. This would decrease the load on

each heater and subsequently make them less prone to failure.

An obvious extension to the experiments conducted with silver is to perform super-elastic scattering using linearly polarised radiation at the same outgoing energies. This would allow the determination of the atomic collision parameters P_{lin} and γ thus giving a complete description of the scattering process.

In reality, the experiments are expected to be far more challenging as a result of lower signal to noise ratio. This in turn is due to the lower population of atoms in the excited state when using linearly polarised light under the same conditions. The population of excited atoms decreases because of higher losses due to spontaneous emission when using linearly polarised light. One way to increase the excited state population would be to excite atoms from both hyperfine ground states of silver. This could be achieved by using an electro-optic modulator EOM to produce side bands at the right frequency from the main laser beam. The ground state splitting in silver is 1977 MHz. By using an EOM at the right frequency, side bands could be added on either side of the main frequency so as to excite the hyperfine ground states to the excited states thus producing a higher density of excited atoms at the interaction region.

The experiments with silver have been restricted to the angles from -97° to 145 ° excluding the range -20°$\leq \theta_e \leq$ 20° because of the geometrical constraints of the spectrometer. Another improvement to the experiment would be to collect data over a larger angular range. This can be achieved by using a magnetic angle changing (MAC) device with which all scattering angles can be accessed from 0°$\leq \theta_e \leq$ 180°. The MAC device has previously been used for super-elastic studies with calcium as mentioned in previous references.

To conclude, super-elastic scattering studies conducted with calcium at low energies have provided accurate data in the low energy regime. This has enabled testing of various theoretical models and it was shown that the CCC model predicts the collision process most effectively at these energies. Additionally, super-elastic experiments performed using silver as a target have yielded data for transition metals with d-shell electrons for the first time, across a broad

range of energies. Excellent agreement was observed when the experimental results were compared to the CCC theory at higher energies and good agreement was found at lower energies. It should be possible to extend the super-elastic studies for silver across a larger scattering angular range with a higher population of excited atoms, by using the above mentioned MAC device and an EOM, which will provide more accurate data to further test theoretical models. It is suggested that the oven designed and constructed in this project be adapted for use with copper and eventually with gold, so that the data from these transition elements may be expanded.

Silver is a transition metal and therefore differs from calcium and all other targets previously studied using the super-elastic scattering process. It is expected that the ten d-shell electrons in the outer 4d orbital of silver will affect the dynamics of the scattering process. This would be the case with gold as well if used as a target. It is hoped that progress in experimental studies in the future will be accompanied by improved calculations from theoretical groups that will take into consideration any effect of the d-electrons in the scattering process.

It is hoped that with continuing progress in the experimental field, a wealth of new accurate data will help to assist theoreticians in deriving a unified theory across a broad energy range, that will be able to give a complete description of the scattering process for any target.

References

[1] H. S. N. Massey, E. H. S. Burhop, and H. B. Gibody, *Electronic and Ionic Impact Phenomena*. Clarendon Press Oxford, 1969.

[2] J. Franck and G. Hertz, "Über zusammenstöße zwischen elektronen und molekülen des quecksilberdampfes und die ionisierungsspannung desselben," *Verh. Dtsch. Phys. Ges*, vol. 16, pp. 457–467, 1914.

[3] B. L. Moiseiwitsch and S. J. Smith, "Electron impact excitation of atoms," *Reviews of Modern Physics*, vol. 40, no. 2, 1968.

[4] N. Andersen, J. Gallagher, and I. Hertel, "Collisional alignment and orientation of atomic outer shels I. direct excitation by electron and atom impact," *Physics Reports*, vol. 165, no. 1-2, 1988.

[5] R. E. Imhof and F. H. Read, "A new electron-photon coincidence mothod for the measurement of lifetimes in atoms and molecules," *Journal of Physics B: Atomic, Molecular and Optical Physics*, vol. 4, no. 4, p. 450, 1971.

[6] M. Eminyan, K. B. MacAdam, J. Slevin, and H. Kleinpoppen, "Measurement of complex excitation amplitudes in electron-helium collisions by angular correlations using a coincidence method," *Physical Review Letters*, vol. 31, no. 9, 1973.

[7] M. Eminyan, K. B. MacAdam, J. Slevin, and H. Kleinpoppen, "Electron-photon angular correlations in electron-helium collisions: measurement of complex excitation amplitudes, atomic orientation and alignment," *Journal of Physics B: Atomic, Molecular and Optical Physics*, vol. 7, no. 12, pp. 1519–42, 1974.

[8] M. A. Khakoo, D. Randy, and F. Ruganas, "Electron-impact excitation of the $1^1S \rightarrow 3^1P$ and $1^1S \rightarrow 4^1P$ transition in helium," *Physical Review A*, vol. 54, no. 5, 1996.

[9] E. Weigold, L. Frost, and K. H. Nygaard, "Large-angle electron-photon coincidence experiment in atomic hydrogen," *Physical Review A*, vol. 21, no. 6, 1980.

[10] P. J. O. Teubner, J. E. Hurst, and J. L. Riley, "Electron-photon coincidence studies in sodium," *Australian Journal of Physics*, vol. 35, pp. 501–511, 1982.

[11] A. Wolcke, J. Croeke, G. F. Hanne, J. Kessler, W. Vollner, K. Bartschat, and K. Blum, "Electron-photon coincidence studies in collisions of polarised electron with mercury atoms," *Physical Review Letters*, vol. 52, no. 13, 1984.

[12] A. J. Murray, W. R. MacGillivray, and M. C. Standage, "Effect of laser intensity variation and coherence on the resonant excitation of the 6P-1-(1)-6D-1(2) transition of atomic mercury," *Journal of Modern Optics*, vol. 38, no. 5, pp. 961–969, 1991.

[13] K. E. Martus, S. H. Zheng, and K. Becker, "Electron-photon coincidence study of heavy-noble-gas excitation at small scattering angles," *Physical Review A*, vol. 44, no. 3, 1991.

[14] M. Jacka, J. Kelly, B. Lohmann, and S. J. Buckman, "Superelastic electron scattering from metastable helium," *Journal of Physics B: Atomic, Molecular and Optical Physics*, vol. 28, pp. L361–L366, 1995.

[15] I. D. Williams, B. Srigengan, A. Platzer, J. B. Greenwood, W. R. Newell, and L. O'Hagan, "Superelastic scattering of electron from Ar^{3+}," *Physica Scripta*, vol. T73, pp. 121–122, 1997.

[16] J. Macek and D. H. Jaecks, "Theory of atomic photon-particle coincidence measurements," *Physical Review A*, vol. 4, no. 6, 1971.

[17] U. Fano and J. Macek, "Impact excitation and polarisation of the emitted light," *Reviews of Modern Physics*, vol. 45, no. 4, p. 553), 1973.

[18] H. S. W. Massey and C. B. O. Mohr, "The collision of slow electrons with atoms. II. General theory and inelastic collisions," *Proceedings of Royal Society A*, pp. 187–201, 1933.

[19] J. C. Percival and M. J. Seaton, "The partial wave theory of electron-hydrogen atom collisions," *Mathematical Proceedings of the Cambridge Philosophical Society*, vol. 53, no. 3, pp. 654–662, 1957.

[20] M. Shurgalin, A. Murray, W. MacGillivray, M. Standage, D. Madison, K. Winkler, and I. Bray, "Atomic collision parameters for electron de-excitation of the 4S-3P transition of sodium," *Journal of Physics B: Atomic, Molecular and Optical Physics*, vol. 32, no. 10, pp. 2439–2459, 1999.

[21] I. V. Hertel and W. Stoll, "Principles and theoretical interpretation of the electron scattering by laser excited atoms," *Journal of Physics B: Atomic, Molecular and Optical Physics*, vol. 7, no. 5, 1974.

[22] I. V. Hertel and W. Stoll, "A crossed beam experiment for the inelastic scattering of slow electrons by excited state sodium atoms," *Journal of Physics B: Atomic, Molecular and Optical Physics*, vol. 7, no. 5, 1974.

[23] H. W. Hermann, I. V. Hertel, W. Reiland, A. Stamatovic, and W. Stoll, "Measurement of the collision-induced alignment in the differential scattering by laser-excited atoms: 3P to nS transitions excited by electron scattering on sodium," *Journal of Physics B: Atomic, Molecular and Optical Physics*, vol. 10, no. 2, 1977.

[24] H. W. Hermann, I. V. Hertel, and M. H. Kelly, "Orientation in the 3P-3S transition in sodium induced by electron impact," *Journal of Physics B: Atomic, Molecular and Optical Physics*, vol. 13, pp. 3465–3479, 1980.

[25] J. J. McClelland, M. H. Kelley, and R. J. Celotta, "Spin dependence in superelastic electron scattering from Na(3P)," *Physical Review Letters*, vol. 55, no. 7, 1985.

[26] J. J. McClelland, M. H. Kelley, and R. J. Celotta, "Large-angle superelastic electron scattering from Na(3P)," *Journal of Physics B: Atomic, Molecular and Optical Physics*, vol. 20, pp. L385–L388, 1987.

[27] P. M. Farrell, C. J. Webb, W. R. MacGillivray, and M. C. Standage, "A comment on the controversy over results obtained from coincidence and superelastic experiments on e^--Na collisions at 22.1 - 20.0 eV," *Journal of Physics B: Atomic, Molecular and Optical Physics*, vol. 22, pp. L527–531, 1989.

[28] P. Teubner, R. Scholten, and G. Shen, "Electron scattering from optically pumped sodium atoms," *Journal of Modern Optics*, vol. 37, no. 11, pp. 1761–1769, 1990.

[29] R. E. Scholten, S. R. Lorentz, J. J. McClelland, M. H. Kelley, and R. J. Celotta, "Spin resolved superelastic scattering from sodium at 10 and 40 eV," *Journal of Physics B: Atomic, Molecular and Optical Physics*, vol. 24, pp. L653–659, 1991.

[30] R. E. Scholten, G. F. Shen, and P. J. O. Teubner, "Superelastic electron scattering from sodium: alignment and orientation parameters," *Journal of Physics B: Atomic, Molecular and Optical Physics*, vol. 26, no. 5, p. 987, 1993.

[31] R. T. Sang, P. M. Farrell, D. H. Madison, W. MacGillivray, and M. C. Standage, "The current status of superelastic scattering studies for e^- Na atom collisions," *Journal of Physics B: Atomic, Molecular and Optical Physics*, vol. 27, no. 6, pp. 1187–1208, 1994.

[32] T. Y. Jiang, Z. Shi, C. H. Ying, L. Vuskovic, and B. Bederson, "Superelastic electron scattering by polarized excited sodium," *Physical Review A*, vol. 51, no. 5, pp. 3773–3782, 1995.

[33] A. T. Masters, R. T. Sang, W. R. MacGillivray, and M. C. Standage, "New data from laser interrogation of electron-atom collision experiments," *Australian Journal of Physics*, vol. 49, pp. 499–514, 1996.

[34] V. Karaganov, I. Bray, and P. J. O. Teubner, "Superelastic scattering in lithium," *Physical Review A*, vol. 54, no. 1, 1996.

[35] V. Karaganov, I. Bray, and P. J. O. Teubner, "Superelastic electron-lithium scattering at 7 and 14 eV," *Journal of Physics B: Atomic, Molecular and Optical Physics*, vol. 31, no. 4, pp. L187–191, 1998.

[36] V. Karaganov, I. Bray, and P. J. O. Teubner, "Electron scattering from optically pumped lithium atoms," *Physical Review A*, vol. 59, pp. 4407–4417, 1999.

[37] I. Bray and A. T. Stelbovics, "Convergent close-coupling calculations of electrom-hydrogen scattering," *Physical Review A*, vol. 46, no. 1, pp. 6995–7011, 1992.

[38] I. Bray, "Convergent close-coupling method for the calculation of electrom scattering of hydrogenlike targets," *Physical Review A*, vol. 49, no. 2, pp. 1066–82, 1994.

[39] I. Bray, "Electrons and photons colliding with atoms: development and application of the convergent close-coupling method," *Journal of Physics B: Atomic, Molecular and Optical Physics*, vol. 35, pp. R117–R146, 2002.

[40] K. A. Stockman, V. Karaganov, I. Bray, and P. J. O. Teubner, "Superelastic electron scattering from potassium," *Journal of Physics B: Atomic, Molecular and Optical Physics*, vol. 31, pp. L867–872, 1998.

[41] D. F. Register, S. Trajmar, S. W. Jensen, and R. T. Poe, "Electron scattering by laser-excited barium atoms," *Physical Review Letters*, vol. 41, no. 11, 1978.

[42] Y. Li and P. W. Zetner, "Transferred orbital angular momentum in the excitation of ^{138}Ba (...6s6p 6^1P_1) by electron impact," *Physical Review A*, vol. 49, no. 2, 1994.

[43] P. V. Johnson, B. Eves, P. W. Zetner, D. Fursa, and I. Bray, "Electron-impact excitation of the $(...6s5d^1d_2)$ to $(...6s6p^1p_1)$ transition in barium," *Physical Review A*, vol. 59, no. 1, pp. 439–454, 1999.

[44] P. V. Johnson and P. W. Zetner, "Electron impact coherence parameters for superelastic transition terminating on the $(...6s6p^1P_1)$ level of the barium atom," *Journal of Physics B: Atomic, Molecular and Optical Physics*, vol. 38, pp. 2793–2810, 2005.

[45] B. V. Hall, Y. Shen, A. J. Murray, M. C. Stansage, W. R. MacGillivray, and I. Bray, "Superlastic electron scattering from laser excited rubidium

at 20 eV incident energy," *Journal of Physics B: Atomic, Molecular and Optical Physics*, vol. 37, pp. 1113–1124, 2004.

[46] K. Ross and B. Sonntag, "High temperature metal atom beam sources," *Rev. Sci. Instrum.*, vol. 66, no. 9, pp. 4409–4430, 1995.

[47] P. M. Farrell, W. R. MacGillivray, and M. C. Standage, "Calculation of the optical parameters for electron super-elastic scattering experiments for the sodium $3^2P_{3/2}$ level," *Physical Review A*, vol. 44, no. 3, p. 1828–1835, 1991.

[48] X. Meng, W. R. MacGillivray, and M. C. Standage, "Line polarisation of laser excited Na d_2-transition resoance fluorescence," *Physical Review A*, vol. 45, no. 3, 1992.

[49] P. V. Johnson, Y. Li, P. W. Zetner, G. Csanak, R. E. H. Clark, and J. Abdallah Jr, "Electron impact excitation of the $(...6s6p^1p_1)$ level in ytterbium," *Journal of Physics B: Atomic, Molecular and Optical Physics*, vol. 31, no. 13, pp. 3027–3041, 1998.

[50] P. W. Zetner, P. V. Johnson, Y. Li, G. Csanak, R. E. H. Clark, and J. Abdallah Jr, "Electron impact excitation of the $(...6s6p^3P_J)$ levels in ytterbium," *Journal of Physics B: Atomic, Molecular and Optical Physics*, vol. 34, pp. 1619–1639, 2001.

[51] D. S. Slaughter, V. Karaganov, M. J. Brunger, P. J. O. Teubner, I. Bray, and K. Bartschat, "Superelastic electron scattering from laser-excited cesium atoms," *Physical Review A*, vol. 75, p. 062717, 2007.

[52] M. Law and P. Teubner, "Orientation of the 4^1P state in calcium by electron impact," *Journal of Physics B: Atomic, Molecular and Optical Physics*, vol. 28, no. 11, p. 2257, 1995.

[53] R. Srivastava, T. Zuo, R. McEachran, and A. Stauffer, "Excitation of the $^{1,3}P_1$ states of calcium, strontium and barium in the relativistic distorted wave approximation," *Journal of Physics B: Atomic, Molecular and Optical Physics*, vol. 25, no. 7, pp. 3709–20, 1992.

[54] R. E. H. Clark, J. Abdallah, G. Csanak, and S. P. Kramer, "Electron impact cross sections and coherence parameters for the $6s^2\ ^1pP$ transition in neutral barium," *Physical Review A*, vol. 40, pp. 2935–2949, 1989.

[55] P. J. O. Teubner, P. M. Farrell, V. Karaganov, M. R. Law, and V. Suvorov, "Laser assisted collision of electrons with metal vapours," *Australian Journal of Physics*, vol. 49, p. 481, 1996.

[56] A. J. Murray and D. Cvejanovic, "Low energy superelastic scattering from the $4\ ^1P_1$ state of calcium," *Journal of Physics B: Atomic, Molecular and Optical Physics*, vol. 36, pp. 4889–4910, 2003.

[57] S. Kawazoe, T. Kai, R. K. Chauhan, R. Srivastava, and S. Nakazaki, "Excitation of the 4^1P state of calcium by electron impact," *Journal of Physics B: Atomic, Molecular and Optical Physics*, vol. 39, no. 3, p. 493, 2006.

[58] O. Zatsarinny, K. Bartschat, L. Bandurina, and S. Gedeon, "Electron impact excitation of calcium," *Journal of Physics B: Atomic, Molecular and Optical Physics*, vol. 40, no. 20, pp. 4023–4031, 2007.

[59] R. J. Chauhan, R. Srivastava, and A. D. Stauffer, "Electron impact excitation of the 4^1P_1 state of calcium," *38*, vol. 38, no. 14, pp. 2385–2394, 2005.

[60] D. V. Fursa and I. Bray, "Calculation of electron-impact 4^1P excitation of calcium," *Journal of Physics B: Atomic, Molecular and Optical Physics*, vol. 41, no. 14, p. 145206, 2008.

[61] M. J. Hussey, A. J. Murray, W. MacGillivray, and G. C. King, "Superelastic electron scattering within a magnetic angle changer: determination of the angular momentum transferred during electron excitation over all scattering angles," *Physical Review Letters*, vol. 99, no. 13, p. 133202, 2007.

[62] D. Cubric, R. Ward, G. C. King, and F. H. Read, "Iron-cored coil system for the measurement of angular distributions of charged particles," *Review of Scientific Instruments*, vol. 71, no. 9, pp. 3323–3325, 2000.

[63] M. J. Hussey, A. J. Murray, W. MacGillivray, and G. King, "Low energy superelastic scattering studies of calcium over the complete angular range using a MAC device," *Journal of Physics B: Atomic, Molecular and Optical Physics*, vol. 41, no. 5, p. 055202, 2008.

[64] W. MacGillivray, A. J. Murray, M. Hussey, G. King, A. Knight-Percival, and S. Satti, "Super-elastic electron scattering from calcium over all angles," *Journal of Physics Conference Series*, vol. 185, no. 1, p. 012025, 2009.

[65] A. J. Murray and P. Hammond, "A novel spectrometer combining laser and electron excitation and deflection of atoms and molecules," *Review of scientific instruments*, vol. 70, no. 4, 1999.

[66] A. Knight-Percival, S. Jhumka, M. Hussey, and A. J. Murray, "Super-elastic electron scattering from the laser-excited 4^1P_1 state of calcium at low incident energy," *Journal of Physics B: Atomic, Molecular and Optical Physics*, vol. 44, p. 105203, 2011.

[67] S. Jhumka, K. L. Nixon, M. Hussey, and A. J. Murray, "Super-elastic electron collision studies from silver-measuring the angular momentum transferred to the target atoms during the collision," *Physical Review A*, vol. 87, p. 052714, 2013.

[68] J. K. Bŏhle, J. R. Laeter, P. de Bievre, H. Hidaka, H. S. Peiser, K. J. R. Rossman, and P. D. P. Taylor, "Isotopic compositions of the elements," *Journal of Physical and Chemical Reference Data*, vol. 34, no. 57, 2005.

[69] I. Bray, "CCC calculations for silver at 20, 25, 30, 40, 50 and 100 eV." Private communication, 2013.

[70] B. V. Hall, R. T. Sang, M. Shurgalin, P. M. Farrell, W. R. MacGillivray, and M. C. Standage, "Electron superelastic scattering states of atomic sodium and rubidium," *Canadian Journal of Physics*, vol. 74, no. 11, pp. 977–983, 1996.

[71] M. Shurgalin, *Electron Scattering from the Optically Prepared 3P State of Sodium*. PhD thesis, Griffith University, Queensland, Australia, 1998.

[72] B. Hall, *Superelastic Electron Scattering from the Laser Excited $5^2P_{3/2}$ State of Rubidium.* PhD thesis, Griffith University, Queensland, Australia, 1998.

[73] K. Blum, *Density Matrix Theory and Applications.* Springer-Verlag New York, 2012.

[74] K. Blum and H. Kleinpoppen, "Electron-photon angular correlation in atomic physics," *Physics Reports*, vol. 52, no. 4, pp. 203–261, 1979.

[75] W. A. Shurcliff, *Polarized light, Production and Use.* Harvard University Press, 1966.

[76] P. M. Farrell, W. R. MacGillivray, and M. C. Standage, "Quantum-electrodynamical calculation of the hyperfine state populations in atomic sodium," *Physical Review A*, vol. 37, no. 11, pp. 4240–51, 1988.

[77] R. Loudon, *The Quantum Theory of Light.* Oxford University Press, 1983.

[78] J. Ackerhalt and J. Eberly, "Quantum electrodynamics and radiation reaction: Nonrelativistic atomic frequency shifts and lifetimes," *Physical Review D*, vol. 10, no. 10, pp. 3350–75, 1974.

[79] C. Cohen-Tannoudji, B. Diu, and F. Laloe, *Quantum Mechanics*, vol. 1. Wiley, 1977.

[80] M. Harvey, *Low Energy Electron Scattering from a Pulsed AC-MOT.* PhD thesis, School of Physics and Astronomy, University of Manchester, United Kingdom, 2009.

[81] N. Strohmaier, "Mphil thesis," Master's thesis, Physics and Astronomy, University of Manchester, United Kingdom, 2005.

[82] P. M. Farrell, *Superelastic elecron scattering from the laser-excited $3^2P_{3/2}$ level of Na.* PhD thesis, Griffith University, Queensland, Australia, 1992.

[83] A. J. Murray, "Theoretical modelling of resonant laser excitation of atoms in a magnetic field," *Physical Review A*, vol. 77, p. 013409, 2008.

[84] A. S. Knight-Percival, *Low Energy Super-Elastic Scattering from Laser Excited Calcium*. PhD thesis, School of Physics and Astronomy, University of Manchester, United Kingdom, 2012.

[85] A. Corney, *Atomic and Laser Spectroscopy*. Oxford University Press, 1977.

[86] W. MacGillivray and M. Standage, "Stepwise electron and laser excitation of atoms," *Physics Reports*, vol. 168, no. 1, pp. 1–54, 1988.

[87] Y. U. Ralchenko, A. E. Kramida, and J. Reader, "NIST atomic spectra database," 2012.

[88] M. Shurgalin, A. J. Murray, W. R. MacGillivray, M. C. Standage, D. H. Madison, K. D. Winkler, and I. Bray, "Comparison of electron-atom collision parameters for s to p transitions under reversal of energy transfer," *Physical Review Letters*, vol. 81, no. 21, pp. 4604–4607, 1998.

[89] M. Shurgalin, A. J. Murray, W. R. MacGillivray, M. C. Standage, D. Madison, K. D. Winkler, and I. Bray, "Angular momentum transferred in inelastically scattered P to S state electron-atom collisions," *American Institute of Physics Conference Proceedings*, vol. 500, no. 436, 2000.

[90] BOC Edwards, *Instruction Manual EM18 and E2M18 rotary vacuum pumps*.

[91] Leybold Vacuum GmBH, *Leybold Vakuum Ionivac ITR 90 instruction sheet*.

[92] Leybold Vakuum, *Leybold Vakuum Ionivac ITR90 Instruction Sheet*.

[93] Thermocoax. thermocoax.com, 2013.

[94] A. Murray, M. Hussey, and M. Needham, "Design and characterization of an atomic beam source with narrow angular divergence for alkali-earth targets," *Meas. Sci. Technol. (UK)*, vol. 17, no. 11, pp. 3094 – 101, 2006.

[95] M. J. Hussey, *Electron impact ionisation studies of molecular nitrogen and carbon dioxide.* PhD thesis, Physics and Astronomy, University of Manchester, United Kingdom, 2003.

[96] A. J. Murray, "Construction of a gravity-fed circulating liquid nitrogen dewar for experiments in high vacuum," *Meas. Sci. Technol.*, vol. 13, pp. N12–N15, 2002.

[97] A. J. Murray, "An automatic controller for filling and maintaining liquid nitrogen levels in dewars," *Measurement Science and Technology*, vol. 15, pp. N31–N34, 2004.

[98] Sirah Laser und Plasmatechnik GmbH, *Matisse user's guide*, 2007.

[99] R. Drever, J. Hall, F. Kowalski, J. Hough, G. Ford, A. Munley, and H. Ward, "Laser phase and frequency stabilization using an optical resonator," *Appl. Phys. B, Photophys. Laser Chem.*, vol. B31, no. 2, pp. 97–105, 1983.

[100] E. D. Black, "An introduction to Pound-Drever-Hall laser frequency stabilisation," *American Association of Physics Teachers*, vol. 69, no. 1, pp. 79–87, 2001.

[101] M. Nickerson, "A review of Pound Drever Hall laser frequency locking," JILA, University of Colorado and Nist.

[102] Spectra-Physics, *Wavetrain external frequency doubler for cw lasers user's manual*, 2004.

[103] A. Murray, M. Green, and D. Cvejanovic, "Frequency locking a doubled ti:sapphire laser using doppler fluorescence." Unpublished, 2001.

[104] J. Brunt, G. King, and F. Read, "Resonance structure in elastic scattering from He,Ne and Ar," *J. Phys. B. At. Mol. Phys.*, vol. 10, no. 7, pp. 1289–1301, 1977.

[105] R. K. Chauhan, R. Srivastava, and A. Stauffer, "Electron impact excitation of the 4^1P_1 state in calcium," *Journal of Physics B: Atomic, Molecular and Optical Physics*, vol. 38, no. 14, pp. 2385–2394, 2005.

[106] S. Kawazoe, T. Kai, R. K. Chauhan, R. Srivastava, and S. Nakazaki, "Excitation of the 4^1P_1 state of calcium by electron impact," *Journal of Physics B: Atomic, Molecular and Optical Physics*, vol. 39, no. 3, p. 493, 2006.

[107] O. Zatsarinny, K. Bartschat, L. Bandurina, and S. Gedeon, "Electron impact excitation of calcium," *Journal of Physics B: Atomic, Molecular and Optical Physics*, vol. 40, no. 20, pp. 4023–4031, 2007.

[108] D. V. Fursa and I. Bray, "Calculation of electron impact 4^1P_1 excitation of calcium," *Journal of Physics B: Atomic, Molecular and Optical Physics*, vol. 41, no. 14, p. 145206, 2008.

[109] I. Bray, "CCC calculations at 8 eV." Private communication, 2011.

[110] M. N. Green, *Fabrication of chromium nanostructures using atom optics*. PhD thesis, School of Physics and Astronomy, University of Manchester, Manchester, United Kingdom, 2006.

[111] E. Schmidt, H. Schroder, B. Sonntag, H. Voss, and H. E. Wetzel, "$M_{2,3}$-shell Auger and autoionisation spectra of free Cr, Mn, Fe, Co, Ni and Cu atoms," *J. Phys. B: Atomic, Molecular and Optical Physics*, pp. 707–718, 1984.

[112] Claris Corporation, "Claris cad," 1989.

[113] Frialit-Degussit ceramics. www.degussit.co.uk.

[114] Omega Industries. www.omega.co.uk.

[115] Behringer, "EP400 2X200W amplifier." www.behringer.com, 2012.

[116] C. D. Kaiser, *Electron impact excitation of atoms and molecules*. PhD thesis, School of Physics and Astronomy, University of Manchester, United Kingdom, 2009.

[117] C. Kaiser, D. Spieker, J. Gao, M. J. Hussey, A. J. Murray, and D. H. Madison, "Coplanar symmetric and asymmetric electron impact ionisation studies from the $1b_1$ state of H_2o at low to intermediate impact

energies," *Journal of Physics B: Atomic, Molecular and Optical Physics*, vol. 40, p.) 2563–2576, 2007.

[118] Leybold Vacuum GmBH, *Turbovac 340M 340MC 340 MCT 341 MCT User Manual*.

[119] M. B. J. Woolf, *e-2e measurements in the perpendicular plane*. PhD thesis, Physics and Astronomy, University of Manchester, United Kingdom, 1989.

[120] A. J. Murray, "Low-cost high-speed pulsed amplifiers for electron, ion and photon detectors," *Measurement Science and Technology*, vol. 23, 2012.

[121] Thorlabs, "GLB10-UV BBO Glan-Laser polariser." www.thorlabs.co.uk.

[122] CVI Melles Griot, "QWPO-325-08-4-R10 zero-order." www.cvimellesgriot.co.uk.

[123] N. Andersen and K. Bartschat, "Complete experiments in atomic collisions," *Advances in atomic, molecular and optical physics*, vol. 36, no. 1, 1996.

[124] National Instruments corporation, "labview." ni.com/labview.